NUMERICAL SIMULATION OF COALESCENCE OF MICRON-SUBMICRON SIZED DROPLETS AND THIN FILMS

A THESIS SUBMITTED TO
THE GRADUATE SCHOOL OF NATURAL AND APPLIED SCIENCES
OF
MIDDLE EAST TECHNICAL UNIVERSITY

BY

YILMAZ BARIŞ ERKAN

IN PARTIAL FULFILLMENT OF THE REQUIREMENTS
FOR
THE DEGREE OF MASTER OF SCIENCE
IN
MECHANICAL ENGINEERING

SEPTEMBER 2021

Approval of the thesis:

NUMERICAL SIMULATION OF COALESCENCE OF MICRON-SUBMICRON SIZED DROPLETS AND THIN FILMS

submitted by **YILMAZ BARIŞ ERKAN** in partial fulfillment of the requirements for the degree of **Master of Science in Mechanical Engineering Department, Middle East Technical University** by,

Prof. Dr. Halil Kalıpçılar
Dean, Graduate School of **Natural and Applied Sciences** ______________

Prof. Dr. M. A. Sahir Arıkan
Head of Department, **Mechanical Engineering** ______________

Prof. Dr. Zafer Dursunkaya
Supervisor, **Mechanical Engineering, METU** ______________

Examining Committee Members:

Assoc. Prof. Dr. Merve Erdal Erdoğmuş
Mechanical Engineering, METU ______________

Prof. Dr. Zafer Dursunkaya
Mechanical Engineering, METU ______________

Assist. Prof. Dr. Altuğ Özçelikkale
Mechanical Engineering, METU ______________

Assist. Prof. Dr. Ali Karakuş
Mechanical Engineering, METU ______________

Assoc. Prof. Dr. Barbaros Çetin
Mechanical Engineering, Bilkent University ______________

Date: 07.09.2021

I hereby declare that all information in this document has been obtained and presented in accordance with academic rules and ethical conduct. I also declare that, as required by these rules and conduct, I have fully cited and referenced all material and results that are not original to this work.

Name, Surname: Yılmaz Barış Erkan

Signature :

ABSTRACT

NUMERICAL SIMULATION OF COALESCENCE OF MICRON-SUBMICRON SIZED DROPLETS AND THIN FILMS

Erkan, Yılmaz Barış
M.S., Department of Mechanical Engineering
Supervisor: Prof. Dr. Zafer Dursunkaya

September 2021, 106 pages

Dynamics of droplet merging emerges with an utmost significance in many scientific areas and its effects ranges vastly from agriculture to engineering. Understanding the underlying physics of coalescence of droplets is, therefore, crucial to have control over its effects in complex systems which they are included. In this study, time dependent coalescence dynamics of fully wetting cylindrical droplets is investigated extensively. Droplets are created utilizing the Young-Laplace equation, and the dynamics of the temporal development and the merger of two liquid droplets is studied through the solution of the governing unsteady Reynolds equation, obtained with lubrication assumption. The governing Reynolds equation is a 4^{th} order non-linear partial differential equation for film thickness and it is solved using a time step marching algorithm in conjunction with an implicit formulation of the spatial domain solved iteratively to account for the non-linear terms.

Keywords: Thin films, droplet coalescence, numerical simulation, micron-submicron sized droplets

ÖZ

MİKRON-MİKRON ALTI BOYUTLU DAMLACIKLARIN VE İNCE FİLMLERİN BİRLEŞİMİNİN SAYISAL SİMÜLASYONU

Erkan, Yılmaz Barış
Yüksek Lisans, Makina Mühendisliği Bölümü
Tez Yöneticisi: Prof. Dr. Zafer Dursunkaya

Eylül 2021 , 106 sayfa

Damlacıkların birleşme dinamiği, birçok bilimsel alanda ortaya çıkmakta ve etkileri tarımdan mühendisliğe kadar çok geniş bir yelpazeyi kapsamaktadır. Bu nedenle damlacıkların birleşmesinin altında yatan fiziği anlamak bulundukları karmaşık sistemler üzerindeki etkilerini kontrol etmek için çok önemlidir. Bu çalışmada, tamamen ıslatan silindirik damlacıklar Young-Laplace denklemi ile oluşturulup birleşme sırasında sıvı kalınlıklarının zamana bağlı gelişiminin dinamiği, yağlama varsayımı ile elde edilen kararsız Reynolds denklemi çözülerek incelenmiştir. Bu problemde Reynolds denklemi, film kalınlığı için 4. dereceden doğrusal olmayan bir kısmi diferansiyel denklemdir ve doğrusal olmayan terimlerin etkisini hesaba katmak için yüzey koordinatı yönünde yinelemeli olarak çözülen örtük bir formülasyon ile zaman içinde adımlı ilerleme algoritması kullanan bir benzetimleme uygulanmıştır.

Anahtar Kelimeler: İnce filmler, damlacık birleşmesi, sayısal simulasyon, mikron-mikron altı boyutlu damlacıklar

To my family and loved ones,

ACKNOWLEDGMENTS

First and above all, I would like to express my sincerest gratitude to my supervisor, Dr. Zafer Dursunkaya for his everlasting support and guidance. This journey could never be completed without his faith in me. I not only benefited from his immense knowledge, but also his world-view opened a whole new chapter in my life.

I am thankful to the examining committee members Dr. Merve Erdal Erdoğmuş, Dr. Altuğ Özçelikkale, Dr. Ali Karakuş, and Dr. Barbaros Çetin for their valuable suggestions and comments.

I would like to convey my special thanks to my superior Dr. Tahsin Çağrı Şişman as well as to my colleagues and friends; İbrahim, Tolga and Arif for their support during my study. I especially enjoyed our long-lasting discussions.

Finally, I owe my deepest appreciations to my father Serhat Erkan, my mother Ender Erkan, my brother Doğu Erkan and my other family members for their never-ending support, inspiration and faith. They always lifted my morale whenever I falter.

TABLE OF CONTENTS

CHAPTERS

APPENDICES

LIST OF TABLES

TABLES

LIST OF FIGURES

FIGURES

LIST OF ABBREVIATIONS

$2D$	Two dimensional
$3D$	Three dimensional
A	Cross sectional area of thin film, m^2
Bo	Bond number, *
g	Gravity, $\mathrm{m\ s^{-2}}$
L	Horizontal length of the droplet, m
L_o	Initial length of the droplet, m
$\dot{m}'_x$	Mass flow rate per unit depth in x-direction, $\mathrm{kg\ m^{-1}\ s^{-1}}$
P_c	Capillary pressure, Pa
P_g	Pressure caused by gravity, Pa
P_l	Liquid pressure, Pa
P_v	Vapour pressure, Pa
$\dot{q}'_x$	Volume flow rate per unit depth in x-direction, $\mathrm{m^2\ s^{-1}}$
u	Fluid velocity in x-direction, $\mathrm{m\ s^{-1}}$
	Greek Symbols
α	Contact angle, °
δ	Film thickness, m
ϕ	Right hand side angle of the meniscus, °
λ_1	First coefficient used in dynamic modelling
λ_2	Second coefficient used in dynamic modelling
λ_3	Third coefficient used in dynamic modelling
μ	Dynamic viscosity, Pa s
ν	Kinematic viscosity, $\mathrm{m^2\ s^{-1}}$
ρ	Density, $\mathrm{kg\ m^{-3}}$

σ	Surface tension, N m^{-1}
ζ	A function used in Eq. (3.26)
	Superscripts
$'$	First derivative with respect to x
$''$	Second derivative with respect to x
$'''$	Third derivative with respect to x
*	Dimensionless

CHAPTER 1

INTRODUCTION

General considerations regarding the formation and coalescence of droplets or thin films have been in the focal point of many research areas for more than a century; relevant research even dates back to Osborne Reynolds' phenomenal study about the drops floating on the surface of water [1]. Understanding the underlying physics of coalescence of droplets is crucial for a wide range of applications in microfluidic systems such as industrial coatings, ink jet applications, spraying pesticides and in phase change heat exchangers in which dropwise condensation occur [2, 3]. Heat transfer performance of heat pipes is also affected by the droplet or thin film coalescence on top of the fins; and therefore, one cannot simply disregard this natural process. In the first part of this chapter, a general introduction regarding droplets and various other related phenomena will be addressed. After that, a detailed literature review will be included.

1.1 Droplets

A droplet is typically a small ellipsoid shape containing liquid inside. Depending on the various environmental and physical parameters, raindrops are practically expected to be smaller than $1 - 3$ mm in diameters [4]. It is observed that bigger droplets are bound to break up eventually short after reaching these limits [5]. Drops may be completely surrounded with free surfaces such as in the case of freely falling raindrops, or they can rest on a solid surface if certain requirements are satisfied. They can either be created via an equipment with a small nozzle such as a Pasteur pipette or by condensation of liquid vapor. There are various physical parameters that affect droplet formation or coalescence such as surfactants, surface tension, capillarity, viscosity, gravity and so on. In the absence of external effects, a droplet would take the shape of a sphere as it has the tendency to have minimal surface area. This is assured by the surface tension to compensate the excess energy accumulated on the surface. Gravitational effects on a statically stable drop may be neglected if the radius of the drop is much less than the capillary length scale. More on surface tension and capillarity will be discussed in Chapter 2. Another parameter that plays an important role on the droplet formation is the contact angle formed with the solid surface. Initial geometrical shape of the drop and the coalescence procedure heavily relies on the contact angle. There are two types of contact angle: dynamic and static contact angles. According to Mittal [6], dynamic contact angle can be assumed as constant for coalescence velocities less than a few millimeters per second. Therefore, the contact angle is accepted as constant in all the coalescence simulations throughout this thesis study, as Mittal's assumption is satisfied.

Wettability is another important characteristics of liquid-solid interactions. Droplet laying on a surface behaves distinctly depending on the liquid and the surface material. For example, on a hydrophobic substrate water drop will have a higher contact angle than on a hydrophilic substrate, as shown in Fig. 1.1:

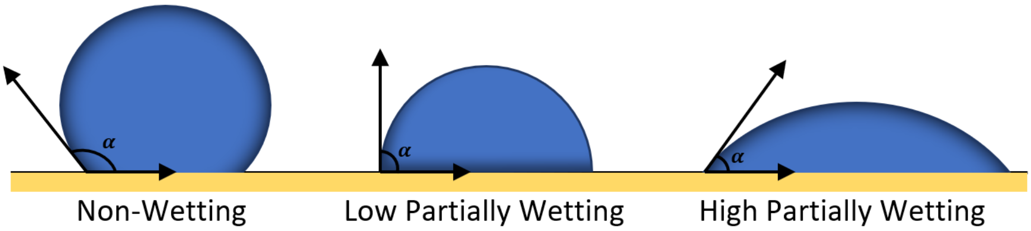

Figure 1.1: Different wettability characteristics are shown. Contact angle α for non-wetting case is $\alpha \geq 180°$, for low partially wetting case is $90° \leq \alpha < 180°$ and for high partially wetting setup is $0° < \alpha < 90°$.

Although there are various wettability options for the droplets, only low and high partially wetting droplets are investigated in this thesis. Therefore, the contact angle that individual droplets have is limited within an interval $0° < \alpha < 90°$. There are several wetting models achieved by altering the surface texture either physically or chemically grafting the surface. Changing the surface texture enables one to control the contact angle of the drop. Surfaces in these models are also known as non-ideal surfaces, however, these are not in the scope of this study. Instead, droplets will be merged upon ideal surfaces in this study, which will be briefly mentioned in the upcoming section.

1.2 Ideal and Non-Ideal Surfaces

Even though non-ideal surfaces are not studied, a brief information regarding both ideal and non-ideal surfaces is given in this section. Non-ideal surfaces can either be homogeneous or heterogeneous. Surfaces that are considered in the latter category are actually composites, i.e. it consists of two or more materials with different properties [7] while non-ideal homogeneous surfaces are rough surfaces made from only one material. These different non-ideal surface types are modelled by Cassie-Baxter and Wenzel's model, respectively, and they are illustrated in Fig. 1.2:

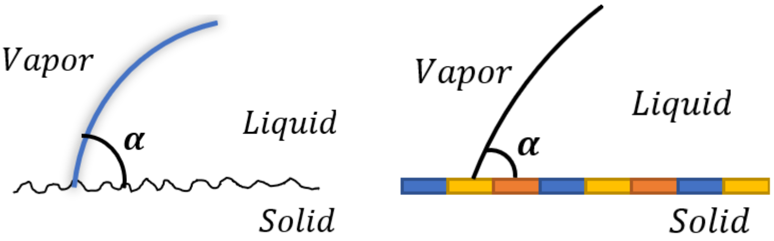

(a) (b)

Figure 1.2: (a) Rough homogeneous surface Wenzel's model and (b) heterogeneous surface as an example to (b) Cassie-Baxter model.

On the other hand, ideal surfaces are considered to be flat, smooth and homogeneous where stabilized contact angle can be achieved under idealized circumstances, i.e. not having external disturbances and being physically, chemically and thermodynamically stable [8]. Furthermore, there is no contact angle hysteresis with ideal surfaces, implying that there are no more than one contact angle. However with certain perturbations, a drop may have more than one unique contact angle as shown in Fig. 1.3. Difference between these angles is termed as contact angle hysteresis.

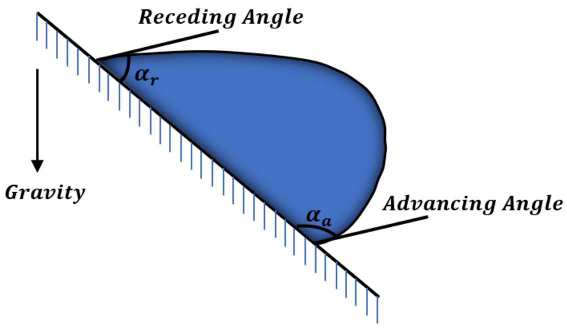

Figure 1.3: Droplet motion on an inclined surface

1.3 Literature Review

Droplet and thin film coalescence have been modelled and experimented in numerous studies in the literature. Although these studies intensified over the last couple decades, fundamental research dates back even 1960's. Study presented by Orchard [9] in 1963 is one of the pioneering studies in the literature. Orchard discussed surface levelling in viscous liquids and had a detailed linear and nonlinear analysis for thin film flows. Driving forces in the surface levelling are mainly the surface tension and the gravity, which are opposed by the viscous forces. Navier-Stokes equations are utilized together with the conservation of mass and simplified with the fact that viscous forces dominate the inertial forces. These flows in which Reynolds number is very small are termed as *creeping flow* or *Stoke's flow*. Orchard then further reduced the problem with the two dimensional restriction of the flow. Different boundary conditions are also applied to the problem, namely free and fixed boundary conditions. After this comprehensive analysis, author defined the motion of the liquid film in terms of the viscosity μ and the surface tension σ. Orchard also argued time scales for very thin and very thick layers of liquids as well as the effect of gravity to the liquid motion [9]. He claimed that for the scales less than about 1 cm, the effect of gravity is so small that it can be safely neglected. For nonlinear thin film levelling, a nonlinear 4^{th}- order partial differential equation is presented, which can also be derived from basic principles. Orchard's results show that error due to linear flow assumption is not important if the initial amplitude of the thin film does not exceed the 80% of the mean film thickness [9].

In 1976, Atherton and Homsy [10] conducted their study regarding the fluid-fluid interfaces that exhibit wavelike motions. They presented mathematical derivation for the evolution of wavelike motion. These nonlinear partial differential equations are defined and studied on both planar and cylindrical coordinates. Atherton and Homsy made similar reasonings with Orchard's study, yet they mostly disregarded the effect of surface tension which could be substantially significant when it comes to engineering applications. Mathematical analysis of hydrodynamics results with moving boundary-value problems; however, Atherton and Homsy proposed an asymptotic method which solves the problem as a function of the surface location [10].

There has been various studies in the literature conducted by Hopper [11–14] regarding the coalescence phenomena. Among these studies, he first investigated and analysed incompressible creeping flow under viscous effects in a finite region bounded by a closed curve which is solely driven by the surface tension. Hopper used rather a different method for the shape evolution of the curve; he described the evolution with a time dependent mapping function [11]. He noted that the problem is highly nonlinear as the geometrical curve evolves through time constantly and large changes occur in the shape. Hopper gave solutions for regions bounded by a regular epitrochoid, a half-plane bounded by a trochoid, and the two-lobbed rosettes. Latter shape gives the exact solution of the coalescence of equal 2D cylinders as shown in Fig. 1.4:.

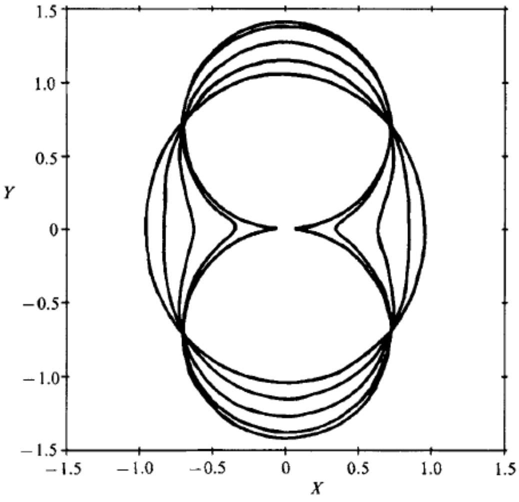

Figure 1.4: Coalescence of two cylinders at different times [11]

Even though Hopper gave an exact analytical relation for the coalescence of two 2D cylinders on a simple plane, he accepted inviscid surroundings when coalescing these 2D cylinders. Therefore, the motion is solely driven by surface tension in [11]. Presented methods provide the exact solution for the problem defined by Hopper; however, he also pointed out that his problem involves a considerable amount of approximations. In an article published in 1992, Hopper obtained an exact solution of the time evolution of the coalescence of a circular cylinder with half-space [12]. In this work, he was able to derive interrelated parametric relations for the height of the coalesced circular cylinder with a half-space in Cartesian coordinates. He also addressed the expected exponential time decay for long times of coalescence problem he described in [12]. Hopper then published an article series that described the coalescence of two circular cylinders driven by surface tension. In the first part [13] he delved into the theoretical background of the coalescence, and in the second part [14] he mostly addresses the shape evolution. He disregarded inertial and gravitational effects in building his theory. Hopper also acknowledged that at very long times gravitational effects may dominate the flow once capillary effects start wearing off. In the close proximity of two liquid surfaces, molecular attractions become relatively important as the free energy residing on surfaces depends on the surface tension [13]. Therefore, it is stated by the author that the neck profile may not satisfy the model at the very early states of the coalescence. Hopper also suggested extending his theory to include time-depending parameters such as density of liquid density ρ, dynamic viscosity μ, and surface tension σ, while keeping these parameters independent of their position. Their time dependency is mostly governed by the temperature of the medium. He ignores further complicated dependencies [13]. In part II of his article series, Hopper continued his theory by giving normalized shape evolution results for initial diameter ratios $1, 2, 5, 20, \infty$ and their respective evolution graphs.

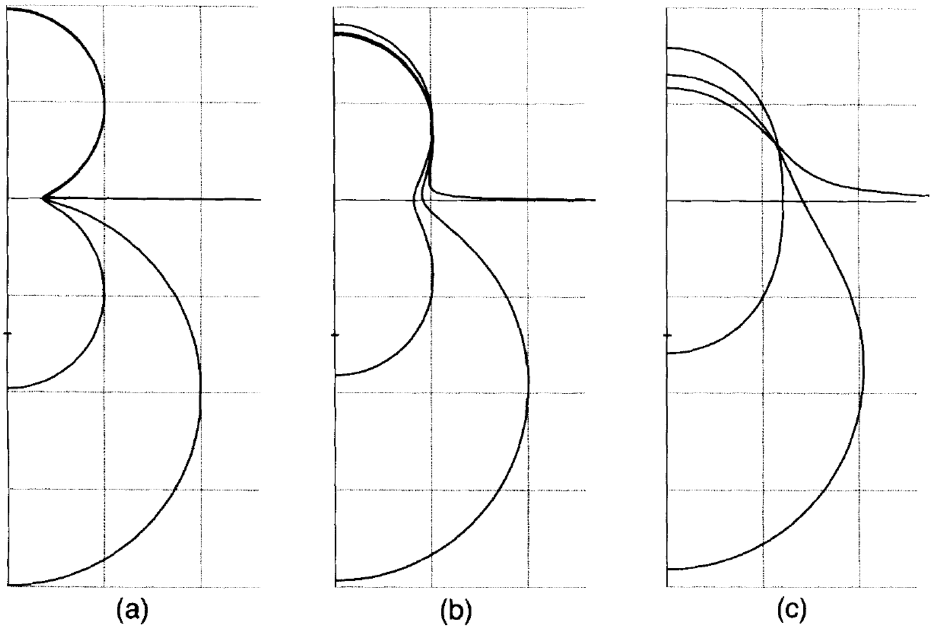

Figure 1.5: Time evolution for different initial diameter ratios $(D = 1, 2, \infty)$ is given consecutively. t is dimensionless time and it is 0.15, 0.5 and 1.2 respectively. [14]

Hopper defined rendered versions of width, length and perimeter and suggested that normalization by smaller diameter is much more efficient than the normalization with larger diameter. He stated that since width of the coalesced matter behaves asymptotically, a power law could be obtained within a good range of convergence. Yet he also pointed out that there is no power law that satisfies the mentioned approximation at the early times of coalescence except from Frenkel's [15] finding. He also critiqued Frenkel's power law claiming that it is physically incorrect and it does not bear the nature of the coalescence. Hopper claimed Frenkel's finding to be completely misleading since he assumed that the dissipation is uniform throughout the merging process [14]. Except for the movement in the neck region, Hopper's results have shown that at early times of coalescence 2D cylinders only make a translational motion towards each other. Yet this argument does not mean a rigid motion occurs between cylinders. Shear is mostly accumulated in the neck region in the early phases of merging [14]. Although Hopper's contribution to the coalescence phenomena is invaluable, his language in his work may be considered as dated by today's researchers.

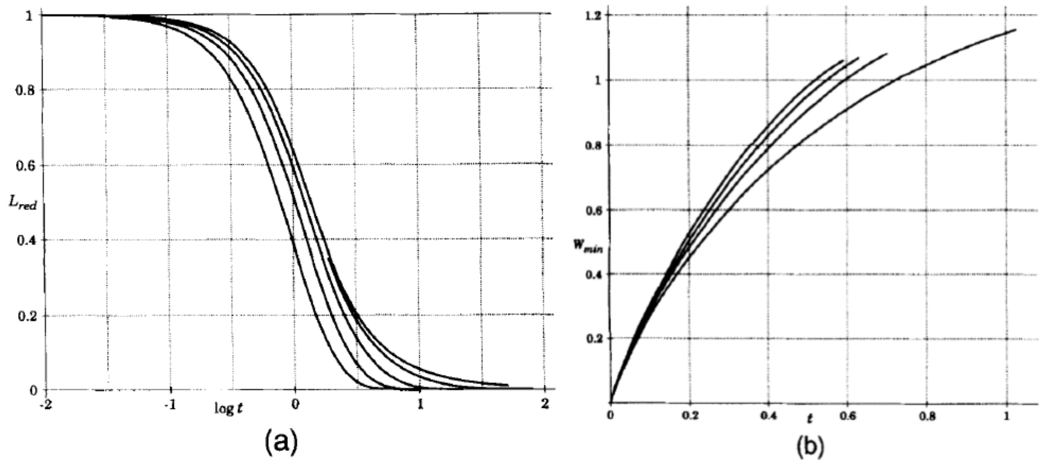

Figure 1.6: Hopper's results. In (a) Reduced length versus logarithmic time for initial diameter ratios $1, 2, 5, 20, \infty$. In (b) Minimum width versus time for initial diameter ratios $1, 2, 5, 20, \infty$. [14]

In their study published in 1999, Eggers et al. [16] broadened the scope of Hopper in [12–14] by making detailed numerical and analytical analysis. They considered different setups in which the exterior of the droplet is inviscid or viscous medium. They assumed a tiny bridge between droplets prior to coalescence, to ease the calculations and avoid the singularity. Their prediction for the evolution of bridge radius were $r_m \sim t\sigma/\mu$, however, after their analysis for switching from three dimensions to two dimensions, it is observed that latter scaling requires a logarithmic adjusting such as $r_m \sim [(1-\xi)/2\pi]t \ln t$. Here, ξ is a parameter originating from viscosity ratio of the interior and exterior media. For viscosity ratios 1 and ∞, given scale is convenient for a dimensionless bridge radii smaller than 0.03. Analysis of Eggers et al. [16] for inviscid and viscous exteriors results with different velocity scales which are investigated further. They pointed out that at the early stages of coalescence, creeping flow assumption can be implemented up until the point where the Reynolds number becomes of order 1. They claim that after this point, it is convenient to work with Euler equations which results in a coupling between velocity and pressure fields. Following their study, Andrieu et al. [17] experimentally and theoretically studied the dynamics of coalescence of partially wetting drops. In their experimental work, nitrogen drops saturated with water are first condensed on a substrate before coalescence event. Their main focus is to observe the relaxation process after the coalescence of droplets having intermediate contact angles. Experimental results of Andrieu et al. indicate surprisingly long relaxation times. However, contact angle dependencies are not investigated in detail. In their theoretical discussion, they gave three different time scales; first one is the inviscid inertial scale, second one is the viscous inertial scale and the last one is viscous relaxation scale. Another similar study is conducted by Aarts [18] in 2005 considering different Reynolds number values. They were able to observe the coalescence in complete viscous regime and it was noted by the author that bridge growth between drops linearly depended on time t. This linear dependency can be achieved by either increasing the viscosity or decreasing the surface tension of the liquid by 5 orders of magnitude [18]. It was emphasized that the coalescence mechanics were driven by the relationship between viscous and inertial effects. Author roughly claims that for settings Re< 1 flow can be assumed as viscous, and for Re> 1 it can be assumed inertial. That being said, Aarts et al. emphasized that the coalescence of water droplets would always be in the inertial regime [18].

The study of Gaskell et al. [2] in 2004 is another important study in terms of droplet motion even though they mainly focused on the spreading of a droplet on an inclined surface. They have developed an efficient and time adaptive multi-grid simulation method for droplet spreading, primarily using the arguments presented in [9]. Even though Gaskell et al. [2] studied droplet spreading, the motion of the droplet was again modelled with a coupled non-linear *long wave* or *lubrication equations* along with a fully implicit time-adaptive numerical scheme. The effect of disjoining pressure was also considered at the point of contact, i.e. wetting lines. Multigrid method that was implemented introduced a simple iterative technique to the problem to reduce the error in approximations. This method was then integrated with Heun's 2^{nd}- order predictor-corrector method to achieve an efficient time-adaptive scheme. Since the dynamic problem at hand was very sensitive to both initial parameters and the time step, Δt, Gaskell et al. tried to control the time step [2]. For the droplet spreading, it was stated that the lubrication assumption was only valid when the active surface was rather smooth. Authors also noted that the accuracy of the aforementioned assumption could waver by the steep slopes, which they considered in this study. However, Gaskell et al. stated that recent studies and experiments show that lubrication theory is extremely sturdy with the steep topographies, providing that Reynolds and Capillary numbers are not too large. This inference creates the basis of droplet spreading with elevated topographies [2].

Ristenpart and his colleagues [19] studied the coalescence of spreading droplets both theoretically and experimentally. Acknowledging that the prior work of others focuses on the slow settling of the merged droplet [17, 20], Ristenpart et al. [19] stated that it is critical to investigate the early-time dynamics of the coalescence. They showed that width of the meniscus bridge between the droplets is correlated with scaling law, $d_m \sim (\sigma h_o^3 t/\mu R_o^2)^{1/2}$. Here d_m is the time-dependent width of the bridge, h_o and R_o are the initial height and radii of the droplet respectively. As a result of careful examination of dimensionless parameters, Ristenpart et al. concluded that the initial geometry of the droplets had substantial impact on the coalescence dynamics, therefore, it is suggested that these initial states has to be determined carefully. This outcome was also provided by other authors [2, 13]. According to results of Ristenpart et al., thin droplets on substrates coalesce much more slowly since they are strongly governed by a power-law depending on their geometry [19]. Ristenpart also suggested a comparison between their scaling for thin films and the work of Eggers et al. [16] who shared a similar argument but worked with freely suspended liquid droplets. He mentioned that in Eggers' study, meniscus bridge between merging droplets grew linearly with time.

In their work published in 2012, Yarin et al. [21] conducted experiments regarding coalescence of droplets with various contact angles on partially wetting surfaces. They analysed coalescence both in top and side views. Later on, their experimental results were compared with various scaling laws and numerical results of the two-dimensional settings. Yarin et al. [21] argued that the coalescence of two freely suspended drops dramatically differed from two droplets merging on a substrate. Main focus of their study was the early-time evolution of the bridge height, $R_y(t)$. They examined the coalescence of diethylene glycol droplets with diameters ranging from 100 μm to 240 μm. Because of the similarities between the droplet coalescence and thin film flow, they utilized the lubrication approximation in their theoretical modelling part. Their theoretical modelling resembles the setting that is used in the current thesis study except authors used a different solution approach with Kutta-Merson method. Moreover, they found it practical to create the initial droplet shape with two tangent parabolas which consisted of a bridge at the symmetry axis. Linearization and non dimensionalization of the main equation was followed by a special stretching method in spatial coordinate [21]. Eventually they were able to find a characteristic time scale for the early-time coalescence, $\tau_{char} = (3\mu R_o/4\sigma)(1/\tan^4(\alpha_o))$, where R_o is initial radius of the droplet and α_o is the initial contact angle. Finally, they presented a power law, $R_y/R_o = c(t/\tau_{char})^d$, which roughly represented the evolution of the bridge height. Here c and d are constants that they provided. Moreover, they noted that only at $10°$ obtained results overlapped with the latter power law; other settings conducted at angles $24°$, $27°$, $56°$ resulted with deviation from this power law at prolonged times. Last but not least, their theoretical results under the lubrication approximation showed that the complete coalescence process followed a similar trend for the bridge height with the experimental results.

Modelling of coalescence of sessile droplets were studied by Sellier and Trelluyer [22] in 2009. They considered a simple coalescence scenario in which the bridge between droplets depending on a power-law growth. The growth of the bridge between droplets relied heavily on the size of droplets and wetting parameters [20]. Their study also included the effect of disjoining pressure in coalescence process as Gaskell et al. did in [2]. They formulated the problem with lubrication approximation and solved it using the commercial finite element software COMSOL since it has been proved quite efficient on modelling thin film applications [23]. To validate their solution, Sellier and Trelluer first analytically solved a set of equations which were similar to the governing dynamic equation and disjoining pressure relation. It should be noted that the validation case they followed was is not physical, yet it bears a self similar analytical solution [24]. Analytical and numerical results for maximum film thickness coincided throughout the study. In Fig. 1.7, the numerical solution of coalescence of droplets in top view is given [22].

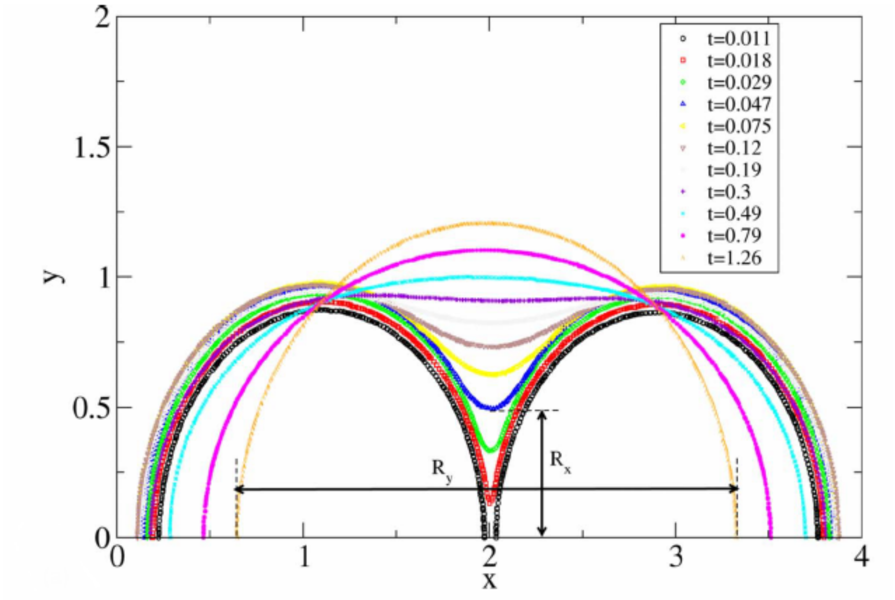

Figure 1.7: Top view of the droplet merging results at various times [22]

Coalescence of two identical droplets was again studied by Sprittles [25] in terms of two different mathematical procedures where their results were compared with the experimental findings in the literature. The first method was the work of [16] and it was addressed as “conventional” by Sprittles [25]. The second method, however, is proposed by Sprittles and it is termed as the interface formation/disappearance method. Sprittles pointed out that the first method used in [16] assumed that a single body of droplet was already formed, in other words, a tiny bridge between droplets was already created. On the contrary, the interface formation/disappearance method also considered the process prior to the bridge formation between droplets. In this method, the free surface between droplets was trapped and it gradually vanished. Consequently, a single body achieved after which the conventional method of [16] started to take over. By using the interface formation/disappearance method, Sprittles [25] argued that singularities were avoided and more accurate results could be obtained since all the necessary physics were accounted prior to the bridge formation. It should also be noted that they rendered 3D droplets into 2D droplets with the utilization of symmetry axis. They also used a zero Bond number in their simulations.

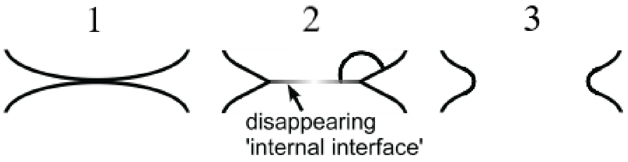

Figure 1.8: Schematic of interface formation/disappearance method [25]

Diverging from previous methods, Zhang et al. [26] investigated the dynamics of a 3D droplet impacting on a solid surface with phase-field method. Phase-field modelling were considered as an efficient way for solving interfacial problems and Zhang et al. [26] were able to simulate the nucleation and dispersion of new droplets by using this method. They utilized a phase-field model consisting of Cahn-Hillard and Navier-Stokes equations. Zhang et al. also studied the effect of dimensionless parameters such as Reynolds number, Weber number, density ratio and viscosity ratio by conducting a detailed non-dimensional analysis [26]. In the end, they observed various impact dynamics by changing aforementioned dimensionless parameters, and compared these results with the experimental findings. In all their simulations, they also included energy dissipation due to impacting.

Another recent study on the coalescence behavior of sessile drops in a thin smectic-A film was conducted by Klopp [27]. They revealed that the scaling laws showed different characteristics in fluids compared to the scaling laws of droplets merging on a solid substrate. Additionally, Klopp [27] studied the 3D droplet coalescence case by utilizing the lubrication approximation. However, they rendered the problem from three dimensions to two dimensions by taking an average of the flow profile across the film thickness and neglecting inertial terms. Moreover, the pressure term used in the equations consisted of the approximated Laplace pressure and the disjoining pressure.

Finally, scaling laws of 3D droplet coalescence was studied thoroughly by Khodabocus et al. [28]. They divided their study into two parts as theoretical and numerical. In the prior, they observed and discussed different scaling laws describing the bridge growth with ordinary differential equations, while in the latter, they validated their findings using the commercial software COMSOL Multiphysics. Khodabocus et al. [28] investigated three distinct regimes, namely, viscous, visco-inertia and inertial coalescence regimes as these were introduced in [29]. Khodabocus et al. also illustrated 3D coalescence results of the numerical study which was in good agreement with their theoretical findings.

To summarize these arguments, theoretical and experimental studies on droplet and thin film coalescence have been ongoing since early 1960's. Two dimensional studies are first led by some theoretical and analytical discussions of Orchard [9] and Hopper [11–14]. Their findings are followed by many other researcher up to this day. However, these studies mostly investigated the coalescence cases where the flow across the film thickness is accepted as average and three dimensional settings are rendered into two dimensional settings.

1.4 Motivation and Objectives of the Thesis

As it can be deduced from the literature review that there has been ongoing research regarding the coalescence of 2D cylindrical and 3D spherical shapes. Comprehension of underlying physics of droplet or thin film coalescence is crucial in order to make certain configurations towards number of applications where droplet merging plays a significant role, therefore, it is our main motivation.

The main objective of this thesis study is to numerically model and simulate the dynamic coalescence of droplets (or thin films), where the droplets are in the micron to sub-micron scales. In order to initiate the simulation, the profile of the droplet at hand is required, thus as the first step, droplets are modelled using the capillary and gravitational effects.

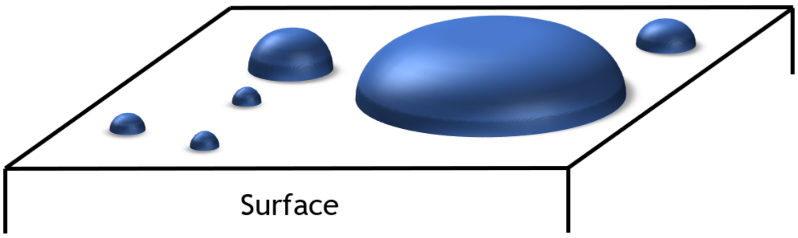

Figure 1.9: Droplets with various sizes residing on a surface

After gaining the ability to create a droplet, coalescence two drops with same dimensions and properties are studied. In this step, utilization of the symmetry axis renders the problem into observing the coalescence dynamics of a single droplet. By eliminating the symmetry axis, however, coalescence of both identical droplets can be numerically simulated and observed for the entire process. Similar to the prior coalescence simulations, coalescence of different sized droplets are also studied. Consequently, both dynamics during the coalescence, and the shape of the coalesced liquid is compared with others work in the literature.

Coalescence analyses that are conducted in this work included the whole spectrum of contact angles between the close proximity of $0°$ and $90°$, while in the literature, only a certain number of contact angles are often studied. It is also observed that many authors did not include the effects of gravity in their simulations. Even though it might seem trivial to include the effect of gravity, it plays an important role on larger droplets. Additionally, the denominator term included in the pressure relation was mostly disregarded in the literature, however, for relatively higher contact angle values its effect cannot be overruled. Therefore, it is included in this study. Moreover, to the best knowledge of the author, the coalescence of different sized droplets are not studied in the literature and it will be addressed in this current thesis study.

CHAPTER 2

PHYSICAL CONCEPTS AND PROBLEM DEFINITION

2.1 Surface Tension

Surface tension is a thermophysical phenomenon that is present at the interface of any two or more immiscible fluids or between fluid-solid interfaces. Molecules of the liquid substance residing at the surface have one missing molecular bond and this in return adds extra energy to the molecules at the surface, as shown in Fig. 2.1. As result, the interface is retracted by inner molecules and a net pressure is generated within. In order to balance the excess pressure inside, the liquid tends to have minimum surface area. Due to this reason smaller liquid-gas systems contain more pressure within. In the Table 2.1 surface tension values of some liquid-air systems at 20°C is given:

Table 2.1: Typical working fluids in contact with air and their surface tension values at 20°C

Liquid	**Surface Tension, N/m**
Water	0.0728
Ammonia	0.0210
Methanol	0.0220
Sodium	0.1910

In Section 1.1 droplets with different contact angles were presented. In liquid-solid interfaces, surface tension dictates the balance between adhesive and cohesive forces that effectively determines the wettability of the liquid on solid surface. Capillary action is also responsible for the liquid movement in the tiny wicks, and it is created *via* the surface tension.

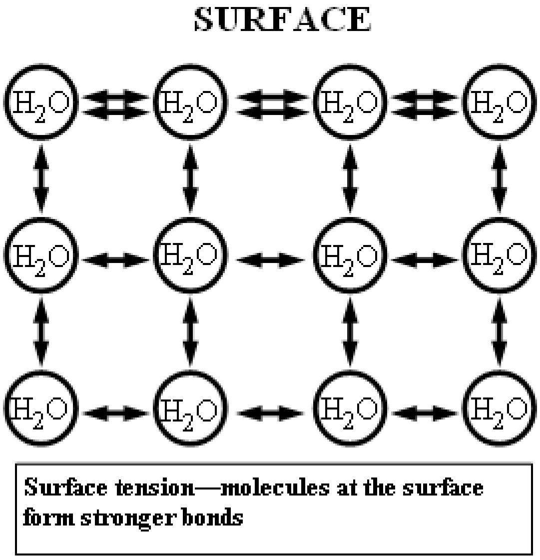

Figure 2.1: Surface tension representation [30]

2.2 Capillary Pressure

Surface tension creates a curvature at the liquid-vapour interface, and this results with a pressure difference. This pressure difference is called the capillary pressure. In three-dimensional settings there are two curvature radii created by the surface tension. Capillary pressure is represented by the Young-Laplace equation:

$$P_c = \sigma \left(\frac{1}{R_1} + \frac{1}{R_2} \right) \tag{2.1}$$

One simplification can be made by considering the gravitational forces and the surface forces. Bond number (or Eötvös number) is a dimensionless number which determines the ratio of the gravitational forces to the surface tension forces. If Bond number is relatively small —which is often the case in micro scales— then one of the radii in Eq. (2.1) can be eliminated. As a result, the simplified version of the capillary pressure becomes:

$$P_c = \frac{\sigma}{R} \tag{2.2}$$

where, R is defined as the radius of curvature.

2.3 Problem Definition

Dynamic coalescence of fully wetting droplets and evolution of thin films are studied in this thesis. All simulations are conducted for cylindrical shapes, i.e. for 2D droplets. In addition, droplet profile is analyzed in the front view instead of top view at all times.

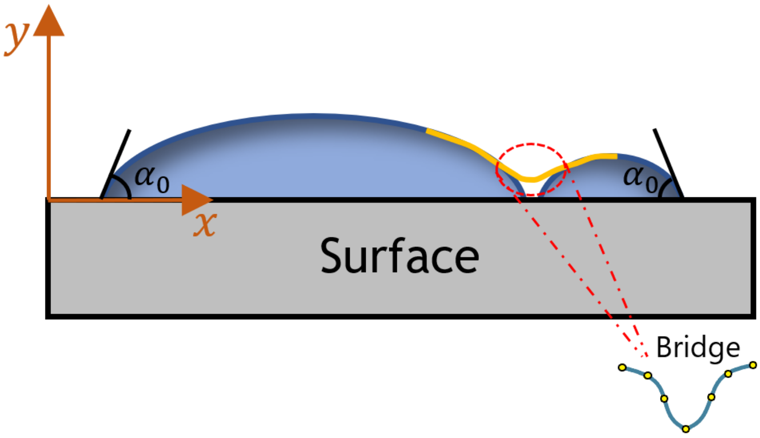

Figure 2.2: Schematic of the expected scenario

Prior to any coalescence simulations, droplets has to be created and readied for the merging by touching each other. In the first simulation, symmetry axis property is invoked, thus, merging process for only one of the droplets is observed. Following this simulation, two exactly same droplets are coalesced by switching to proper boundary conditions. After accomplishing this setting, different sized droplets are merged. Once droplets are close enough to each other, molecular interactions start and a singularly fast movement occurs for a very short amount of time. To avoid the complications brought by this singular movement, it is intrinsically assumed that droplets barely touch each other so that a tiny bridge is just formed between them. This bridge is presented in the Fig. 2.2 and it will usually be one order of magnitude smaller than the maximum thickness of the initial droplet. All the arguments presented in this section will be elaborated in Chapter 3 along with the proper methodology and solution procedure.

CHAPTER 3

MODELLING AND SOLUTION METHODOLOGY

3.1 Driving Forces: Capillarity and Gravity

Capillarity and gravity are the two phenomena together with the surface tension that effect the morphology of the droplets or thin films. Capillary pressure is defined as the pressure difference between two non-miscible liquids and it is caused by the surface tension. Capillary pressure can be expressed with the renowned Young-Laplace equation by substituting the radius of curvature term into Eq. (2.2):

$$\Delta P = \frac{\sigma \delta''}{[1 + (\delta')^2]^{\frac{3}{2}}} \tag{3.1}$$

where the pressure jump at the interface is defined as,

$$\Delta P = (P_v - P_l) \tag{3.2}$$

where P_v is the vapor pressure and P_l is the liquid pressure. Even though it was stated in Section 1.3 that gravity can be neglected for droplets with size less than ~ 2.7 mm, addition of gravity does not increase the complexity of the equation drastically. Thus, it is decided to add gravity term when modelling the droplet so that both capillary and gravitational effects contribute to the pressure inside the droplet. It contributes this pressure jump with,

$$P_g = \rho g \delta \tag{3.3}$$

which will be combined with Eq. (3.1). Moreover, for the generic droplets, the sign of the second derivative is negative, thus, a negative sign is also added in front of the surface tension term in Eq. (3.1). Therefore, the pressure jump between the innards and the exterior of the droplet becomes,

$$\Delta P = \frac{-\sigma\delta''}{[1+(\delta')^2]^{\frac{3}{2}}} + \rho g \delta \tag{3.4}$$

In many studies, Eq. (3.4) is further simplified by neglecting the effect of the denominator term. In this thesis, the effect of this denominator term will be included whether it may be small or substantial.

3.2 Derivation of the Reynolds Equation with Lubrication Assumption

As Orchard also mentions in his study, thin film evolution or droplet dynamics can be derived from basic principles [9]. In this section, the detailed derivation of this resulting dynamic partial differential equation will be presented. In the settings where thin films or micro regions are included, viscosity effects become effectively important in the calculations. In such flows, Reynolds number becomes so small that we can employ creeping flow or lubrication assumptions. For lubrication assumption to be applicable, the ratio of the diffusion time scale to convection time scale as a function the local film thickness, δ_{local}, extend of flow, L_{flow}, kinematic viscosity ν and the local average velocity u_{local} needs to be defined [31]:

$$\frac{t_{diff}}{t_{conv}} \sim \mathcal{O}\left(\frac{\delta_{local}^2/\nu}{L_{flow}/u_{local}}\right) \sim \mathcal{O}\left(\frac{\delta_{local}}{L_{flow}} Re_{local}\right) \ll 1 \tag{3.5}$$

Therefore, either local Reynolds number or the amplitude of the thin film/droplet needs to be small enough to apply the lubrication assumption. In the light of these assumptions, our x-momentum equation is greatly rendered into:

$$\frac{\partial^2 u}{\partial y^2} = \frac{1}{\mu}\frac{\partial P}{\partial x} \tag{3.6}$$

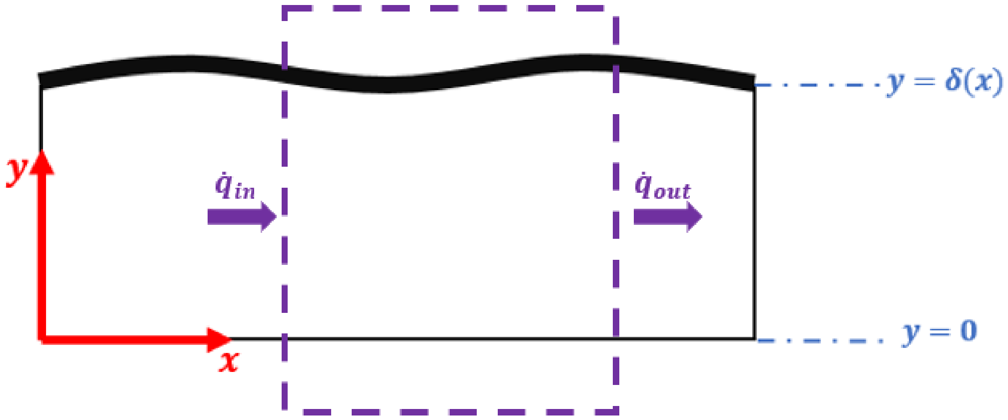

Figure 3.1: Coordinate system for the dynamic equation

There is no-slip condition at the surface droplet lies, and at the free surface of the droplet there is zero tangential stress. Therefore, considering the coordinate system shown in Fig. 3.1, boundary conditions for this problem are:

$$\begin{aligned} y = 0; &\quad u = 0 \\ y = \delta; &\quad \frac{\partial u}{\partial y} = 0 \end{aligned} \tag{3.7}$$

Integration of Eq. (3.6) twice with above boundary conditions, velocity profile is found to be,

$$u(y) = \frac{1}{2\mu}\frac{\partial P}{\partial x}(y^2 - 2\delta y) \tag{3.8}$$

Additionally, volume flow rate per unit depth in the x-direction is:

$$\dot{q}'_x = \int_0^{\delta} u dy \tag{3.9}$$

Inserting previously found velocity profile in Eq. (3.9) and integrating it, volume flow rate per unit depth in x-direction is found to be:

$$\dot{q}'_x = \frac{-\delta^3}{3\mu}\frac{\partial P}{\partial x} \tag{3.10}$$

Furthermore, the conservation of mass also needs to be satisfied. To do so, an infinitesimal control volume (CV) over the flow has to be designated as in Fig. 3.2. It can be seen from the figure that not only there is incoming and outgoing mass flow rates, but also a substantial amount of liquid mass transverses through the top boundary of CV. Therefore, mass balance is written as:

$$\dot{m}'_{out} - \dot{m}'_{in} + \dot{m}'_{top} = 0 \tag{3.11}$$

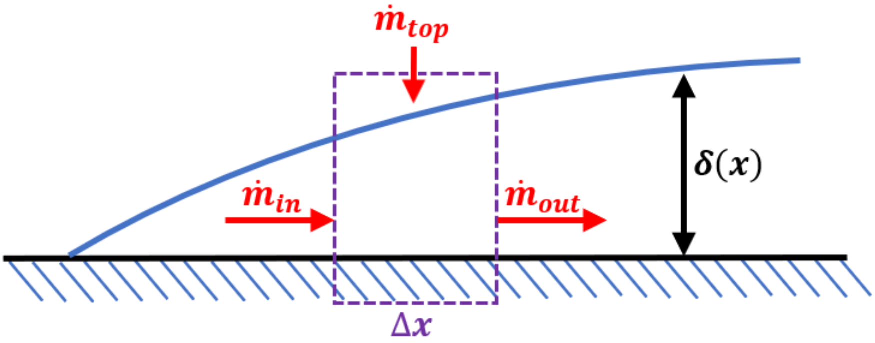

Figure 3.2: Mass balance of an evolving droplet

Notice also that the single quotation mark again represents per unit depth. While $\dot{m}'_{top}$ is equal to the rate of change of droplet thickness in x-direction, the difference between incoming and outgoing mass rates are easily calculated from Taylor Series expansion. Then, mass balance per unit depth over the infinitesimal length Δx becomes:

$$\overbrace{\dot{m}'_{in} + \frac{d\dot{m}'_{in}}{dx}\Delta x}^{\dot{m}'_{out}} - \dot{m}'_{in} + \overbrace{\rho\frac{\partial \delta}{\partial t}}^{\dot{m}'_{top}}\Delta x = 0 \tag{3.12}$$

where incoming mass flow rate is,

$$\dot{m}'_{in} = \rho \int_0^{\delta} u dy \tag{3.13}$$

Notice that integral term in Eq. (3.13) is nothing but the volume flow rate per unit depth in Eq. (3.10). Using these two relations with Eq. (3.12) we finally have:

$$\rho \frac{\partial \delta}{\partial t} + \frac{\partial}{\partial x}\left(\rho \frac{-\delta^3}{3\mu}\frac{\partial P}{\partial x}\right) = 0 \tag{3.14}$$

or rather,

$$\frac{\partial \delta}{\partial t} = \frac{1}{3\mu}\frac{\partial}{\partial x}\left(\delta^3 \frac{\partial P}{\partial x}\right) \tag{3.15}$$

Eq. (3.15) is a 4^{th}- order nonlinear partial differential equation that represents the time evolution of the droplet thickness during the coalescence. Eq. (3.15) can also be reached via taking integral of conservation of mass equation over the domain and implementing Leibniz integral rule to each term, however, it is somewhat cumbersome and the wedge effect appearing due to lubrication assumption has to be dealt with. Partial derivative term on the left hand side of Eq. (3.15) assumes constant film thickness along the x-direction. Therefore, one must also needs to consider these spatial effects. Rewriting partial derivative $\partial\delta/\partial t$ as total derivative:

$$\frac{\partial \delta}{\partial t} = \frac{d\delta}{dt} - \frac{\partial \delta}{\partial x}\frac{dx}{dt} \tag{3.16}$$

and our finalized equation becomes,

$$\boxed{\frac{d\delta}{dt} - \frac{\partial \delta}{\partial x}\frac{dx}{dt} = \frac{1}{3\mu}\frac{\partial}{\partial x}\left(\delta^3 \frac{\partial P}{\partial x}\right)} \tag{3.17}$$

3.3 Droplet Modelling

In Section 3.1, a pressure relation consisting of capillary term and gravitational term is reached. Rearranging this relation, we have:

$$\delta'' = -\frac{\Delta P}{\sigma}\left[1 + (\delta')^2\right]^{\frac{3}{2}} + \frac{\rho g}{\sigma}\left[1 + (\delta')^2\right]^{\frac{3}{2}}\delta \tag{3.18}$$

Above relation is an nonlinear second order ordinary differential equation (ODE) and it can be solved with reduction of order. Letting $\delta' = v$ and $\delta'' = v'$ we have the set:

$$\begin{gathered} \delta' = v \equiv g(x, \delta, v) \\ v' = -\frac{\Delta P}{\sigma}\left[1 + v^2\right]^{\frac{3}{2}} + \frac{\rho g}{\sigma}\left[1 + v^2\right]^{\frac{3}{2}}\delta \equiv f(x, \delta, v) \end{gathered} \tag{3.19}$$

Problem is now converted to two first-order coupled ordinary differential equations. This system can be solved with various numerical methods, however, solution with Runge-Kutta 4 (RK4) method is preferred since with $\mathcal{O}(h^4)$ admits enough accuracy up to a relative error value of 10^{-12} in the film thickness at the right boundary. RK4 method for both relations are given as:

$$\begin{aligned} \delta_{i+1} &= \delta_i + \frac{dx}{6}(K_1 + 2K_2 + 2K_3 + K_4) \\ v_{i+1} &= v_i + \frac{dx}{6}(L_1 + 2L_2 + 2L_3 + L_4) \end{aligned} \tag{3.20}$$

where the coefficients K_1, K_2, K_3, K_4 and L_1, L_2, L_3, L_4 are respectively:

$$\begin{aligned} &K_1 \equiv g\left(x_i, \delta_i, v_i\right) = v_i \\ &K_2 \equiv g\left(x_i + \frac{dx}{2}, \delta_i + \frac{dx}{2}K_1, v_i + \frac{dx}{2}L_1\right) = v_i + \frac{dx}{2}L_1 \\ &K_3 \equiv g\left(x_i + \frac{dx}{2}, \delta_i + \frac{dx}{2}K_2, v_i + \frac{dx}{2}L_2\right) = v_i + \frac{dx}{2}L_2 \\ &K_4 \equiv g\left(x_i + dx, \delta_i + dxK_3, v_i + dxL_3\right) = v_i + dxL_3 \end{aligned} \tag{3.21}$$

and,

$$
\begin{aligned}
&L_1 \equiv f(x_i, \delta_i, v_i) = -\frac{\Delta P}{\sigma}\left[1+v^2\right]^{\frac{3}{2}} + \frac{\rho g}{\sigma}\left[1+v^2\right]^{\frac{3}{2}}\delta_i \\
&L_2 \equiv f\left(x_i + \frac{dx}{2}, \delta_i + \frac{dx}{2}K_1, v_i + \frac{dx}{2}L_1\right) = \\
&\quad -\frac{\Delta P}{\sigma}\left[1+\left(v_i + \frac{dx}{2}L_1\right)^2\right]^{\frac{3}{2}} + \frac{\rho g}{\sigma}\left[1+\left(v_i + \frac{dx}{2}L_1\right)^2\right]^{\frac{3}{2}}\left(\delta_i + \frac{dx}{2}K_1\right) \\
&L_3 \equiv f\left(x_i + \frac{dx}{2}, \delta_i + \frac{dx}{2}K_2, v_i + \frac{dx}{2}L_2\right) = \\
&\quad -\frac{\Delta P}{\sigma}\left[1+\left(v_i + \frac{dx}{2}L_2\right)^2\right]^{\frac{3}{2}} + \frac{\rho g}{\sigma}\left[1+\left(v_i + \frac{dx}{2}L_2\right)^2\right]^{\frac{3}{2}}\left(\delta_i + \frac{dx}{2}K_2\right) \\
&L_4 \equiv f(x_i + dx, \delta_i + dxK_3, v_i + dxL_2) = \\
&\quad -\frac{\Delta P}{\sigma}\left[1+(v_i + dxL_3)^2\right]^{\frac{3}{2}} + \frac{\rho g}{\sigma}\left[1+(v_i + dxL_3)^2\right]^{\frac{3}{2}}(\delta_i + dxK_3)
\end{aligned}
\tag{3.22}
$$

Finally, boundary conditions for a basic droplet model on a flat surface are $\delta(0) = 0$ and $\partial\delta(0)/\partial x = \tan(\alpha)$, where the former one simply states that the film thickness starts from zero, and the latter boundary condition points out the contact angle. In terms of changed variables, boundary conditions for the problem become:

$$
\begin{aligned}
\delta(0) &= 0 \\
v(0) &= \tan(\alpha)
\end{aligned}
\tag{3.23}
$$

Providing the desired cross sectional area (A) or the horizontal length (L) of the droplet, Eqs. (3.20) to (3.22) are solved together with boundary conditions at (3.23). RK4 method will continue to solve our set of equations until we meet a specific criteria. For droplet modelling, the computation stops as soon as the film thickness is equal to or below zero. Additionally, pressure term in the relations is unknown and must be guessed initially. After the first guess and first iteration of the solution, A or L must be checked for convergence with the desired value. If they do not converge, another guess with a fresh solution must be introduced. Consequently, using these two different ΔP values and the different A's or L's with Newton's Linear Interpolation method, a better ΔP value is achieved. Interpolation method used is given in Eq. (3.24) together with Table 3.1:

Table 3.1: Example for Newton's Linear Interpolation

$\boldsymbol{L}$	$\boldsymbol{\Delta P}$
L_1	ΔP_1
L_2	ΔP_2
$L_{desired}$	ΔP_{next}

$$\Delta P_{next} = \frac{(L_{desired} - L_1)(\Delta P_2 - \Delta P_1)}{L_2 - L_1} + \Delta P_1 \tag{3.24}$$

Our droplet is modelled once the cross sectional area or the horizontal length for the droplet with predetermined contact angle is converged. Depending on the adequateness of the initial guess for ΔP, converging to desired horizontal length may require more than one iteration. As horizontal length criterion is reached, the total number of nodes that we determined in the first place must also be met, such as 100, 200, 400 or 1000 etc. nodes. For computational time concerns, it is always better working with smaller total number of nodes, however, for the contact angles at close proximity to $90°$, droplet may only be modelled with a finer mesh and with a good initial pressure guess.

3.4 Dynamic Modelling of Coalescence of Droplets

Droplet coalescence (or thin film evolution) is governed by 4^{th}- order nonlinear partial differential equation found in Section 3.2. Pressure term inside Eq. (3.17) is substituted with relation 3.4:

$$\frac{d\delta}{dt} - \frac{\partial \delta}{\partial x}\frac{dx}{dt} = \frac{1}{3\mu}\frac{\partial}{\partial x}\left[\delta^3 \frac{\partial}{\partial x}\left(\frac{-\sigma\delta''}{[1+(\delta')^2]^{\frac{3}{2}}} + \rho g \delta\right)\right] \tag{3.25}$$

At this point, it is beneficial to define a function ζ to improve the readability of equations:

$$\zeta = \frac{1}{[1+(\delta')^2]^{3/2}} \tag{3.26}$$

Rewriting Eq. (3.25),

$$\frac{d\delta}{dt} - \frac{\partial \delta}{\partial x}\frac{dx}{dt} = \frac{-\sigma}{3\mu}\frac{\partial}{\partial x}\left\{\delta^3 \frac{\partial}{\partial x}\left[\left(\zeta\frac{\partial^2 \delta}{\partial x^2}\right) + \rho g \delta\right]\right\} \tag{3.27}$$

Further manipulating above relation,

$$\begin{aligned}\frac{d\delta}{dt} - \frac{\partial \delta}{\partial x}\frac{dx}{dt} = \frac{-\sigma}{3\mu}\left[3\delta^2\left(\frac{\partial \delta}{\partial x}\right)\frac{\partial}{\partial x}\left(\zeta\frac{\partial^2 \delta}{\partial x^2}\right) + \delta^3\frac{\partial^2}{\partial x^2}\left(\zeta\frac{\partial^2 \delta}{\partial x^2}\right)\right] \\ + \frac{\rho g}{3\mu}\left[3\delta^2\left(\frac{\partial \delta}{\partial x}\right)^2 + \delta^3\frac{\partial^2 \delta}{\partial x^2}\right]\end{aligned} \tag{3.28}$$

Finite difference methods are employed throughout this thesis. In Eq. (3.28) backward difference scheme of order $\mathcal{O}(h)$ is applied for the time derivative, and central difference schemes of order $\mathcal{O}(h^2)$ is used for space derivatives:

$$
\frac{\delta_i^k-\delta_i^{k-1}}{\Delta t}-\left(\frac{\delta_{i+1}^k-\delta_{i-1}^k}{2\Delta x}\right)\left(\frac{x_i^k-x_i^{k-1}}{\Delta t}\right)=\frac{-\sigma}{3\mu}\Bigg\{\underbrace{3\delta_i^{k^2}}_{\text{nonlinear}}\left(\frac{\delta_{i+1}^k-\delta_{i-1}^k}{2\Delta x}\right)
$$

$$
\underbrace{\left(\frac{\zeta_{i+1}^k\delta_{i+1}^{k''}-\zeta_{i-1}^k\delta_{i-1}^{k''}}{2\Delta x}\right)}_{\text{nonlinear}}+\underbrace{\delta_i^{k^3}}_{\text{nonlinear}}\left(\frac{\overbrace{\zeta_{i+1}^k}^{\text{nonlinear}}\,\delta_{i+1}^{k''}-\overbrace{2\zeta_i^k}^{\text{nonlinear}}\,\delta_i^{k''}+\overbrace{\zeta_{i-1}^k}^{\text{nonlinear}}\,\delta_{i-1}^{k''}}{\Delta x^2}\right)\Bigg\}+
$$

$$
\frac{\rho g}{3\mu}\Bigg\{\underbrace{3\delta_i^{k^2}}_{\text{nonlinear}}\underbrace{\left(\frac{\delta_{i+1}^k-\delta_{i-1}^k}{2\Delta x}\right)}_{\text{nonlinear}}\left(\frac{\delta_{i+1}^k-\delta_{i-1}^k}{2\Delta x}\right)+\underbrace{\delta_i^{k^3}}_{\text{nonlinear}}\left(\frac{\delta_{i+1}^{k''}-\delta_i^{k''}+\delta_{i-1}^{k''}}{\Delta x^2}\right)\Bigg\}
\tag{3.29}
$$

In above relation subscript i represents space and superscript k represents time. There are multiple nonlinear terms present in Eq. (3.29). To be able to proceed with finite difference methods, these nonlinearities has to be dealt with a proper linearization method, which adds an iterative technique to the problem at hand. Therefore, we proceed with linearization of Eq. (3.29):

$$
{}_{l+1}\delta_i^k-\delta_i^{k-1}-\lambda_3\left({}_{l+1}\delta_{i+1}^k-{}_{l+1}\delta_{i-1}^k\right)=\overset{\lambda_1}{\boxed{\frac{-\sigma\Delta t}{3\mu\Delta x^4}}}\Bigg\{\frac{3}{4}\left({}_{l}\delta_i^k\right)^2\Big[{}_{l}\zeta_{i+1}^k
$$

$$
\left({}_{l}\delta_{i+2}^k-{}_{l}2\delta_{i+1}^k+{}_{l}\delta_i^k\right)-{}_{l}\zeta_{i-1}^k\left({}_{l}\delta_i^k-2\,{}_{l}\delta_{i-1}^k+{}_{l}\delta_{i-2}^k\right)\Big]\left({}_{l+1}\delta_{i+1}^k-{}_{l+1}\delta_{i-1}^k\right)+
$$

$$
\left({}_{l}\delta_i^k\right)^3{}_{l}\zeta_{i+1}^k\left({}_{l+1}\delta_{i+2}^k-{}_{l+1}2\delta_{i+1}^k+{}_{l+1}\delta_i^k\right)-2\left({}_{l}\delta_i^k\right)^3{}_{l}\zeta_i^k\left({}_{l+1}\delta_{i+1}^k-{}_{l+1}2\delta_i^k+{}_{l+1}\delta_{i-1}^k\right)
$$

$$
+\left({}_{l}\delta_i^k\right)^3{}_{l}\zeta_{i-1}^k\left({}_{l+1}\delta_i^k-{}_{l+1}2\delta_{i-1}^k+{}_{l+1}\delta_{i-2}^k\right)\Bigg\}+
$$

$$
\underset{\lambda_2}{\boxed{\frac{\rho g\Delta t}{3\mu\Delta x^2}}}\Bigg\{\frac{3}{4}\left({}_{l}\delta_i^k\right)^2\left({}_{l}\delta_{i+1}^k-{}_{l}\delta_{i-1}^k\right)\left({}_{l+1}\delta_{i+1}^k-{}_{l+1}\delta_{i-1}^k\right)+\left({}_{l}\delta_i^k\right)^3
$$

$$
\left({}_{l+1}\delta_{i+1}^k-2\,{}_{l+1}\delta_i^k+{}_{l+1}\delta_{i-1}^k\right)\Bigg\}
\tag{3.30}
$$

Due to linearization process, third subscript now appears in Eq. (3.30) as l. Linearization reasonings and solution procedure will be presented after reaching the general finite difference relation. Again for the sake of simplicity, λ_1, λ_2 and λ_3 values are defined as following:

$$\lambda_1 = \frac{-\sigma\Delta t}{3\mu\Delta x^4} \quad , \quad \lambda_2 = \frac{\rho g\Delta t}{3\mu\Delta x^2} \quad \mathit{and} \quad \lambda_3 = \frac{x_i^k - x_i^{k-1}}{2\Delta x}$$

Finally, collecting the similar terms, we reach our general expression as:

$$\begin{aligned}
&\left\{ -\lambda_1 \left({}_l\delta_i^k\right)^3 {}_l\zeta_{i-1}^k \right\} {}_{\boldsymbol{l+1}}\boldsymbol{\delta}_{\boldsymbol{i-2}}^{\boldsymbol{k}} + \\
&\left\{ \frac{3\lambda_1}{4} \left({}_l\delta_i^k\right)^2 \left[{}_l\zeta_{i+1}^k \left({}_l\delta_{i+2}^k - 2\,{}_l\delta_{i+1}^k + {}_l\delta_i^k\right) - {}_l\zeta_{i-1}^k \left({}_l\delta_i^k - 2\,{}_l\delta_{i-1}^k + {}_l\delta_{i-2}^k\right) \right] + \right. \\
&\left. 2\lambda_1 \left({}_l\delta_i^k\right)^3 {}_l\zeta_i^k + 2\lambda_1 \left({}_l\delta_i^k\right)^3 {}_l\zeta_{i-1}^k - \lambda_2 \left({}_l\delta_i^k\right)^3 + \frac{3\lambda_2}{4} \left({}_l\delta_i^k\right)^2 \left({}_l\delta_{i+1}^k - {}_l\delta_{i-1}^k\right) + \lambda_3 \right\} {}_{\boldsymbol{l+1}}\boldsymbol{\delta}_{\boldsymbol{i-1}}^{\boldsymbol{k}} + \\
&\left\{ 1 - \lambda_1 \left({}_l\delta_i^k\right)^3 {}_l\zeta_{i+1}^k - 4\lambda_1 \left({}_l\delta_i^k\right)^3 {}_l\zeta_i^k - \lambda_1 \left({}_l\delta_i^k\right)^3 {}_l\zeta_{i-1}^k + 2\lambda_2 \left({}_l\delta_i^k\right)^3 \right\} {}_{\boldsymbol{l+1}}\boldsymbol{\delta}_{\boldsymbol{i}}^{\boldsymbol{k}} + \\
&\left\{ \frac{-3\lambda_1}{4} \left({}_l\delta_i^k\right)^2 \left[{}_l\zeta_{i+1}^k \left({}_l\delta_{i+2}^k - 2\,{}_l\delta_{i+1}^k + {}_l\delta_i^k\right) - {}_l\zeta_{i-1}^k \left({}_l\delta_i^k - 2\,{}_l\delta_{i-1}^k + {}_l\delta_{i-2}^k\right) \right] + \right. \\
&\left. 2\lambda_1 \left({}_l\delta_i^k\right)^3 {}_l\zeta_{i+1}^k + 2\lambda_1 \left({}_l\delta_i^k\right)^3 {}_l\zeta_i^k - \lambda_2 \left({}_l\delta_i^k\right)^3 - \frac{3\lambda_2}{4} \left({}_l\delta_i^k\right)^2 \left({}_l\delta_{i+1}^k - {}_l\delta_{i-1}^k\right) - \lambda_3 \right\} {}_{\boldsymbol{l+1}}\boldsymbol{\delta}_{\boldsymbol{i+1}}^{\boldsymbol{k}} + \\
&\qquad\qquad \left\{ -\lambda_1 \left({}_l\delta_i^k\right)^3 {}_l\zeta_{i+1}^k \right\} {}_{\boldsymbol{l+1}}\boldsymbol{\delta}_{\boldsymbol{i+2}}^{\boldsymbol{k}} = \boldsymbol{\delta}_{\boldsymbol{i}}^{\boldsymbol{k-1}}
\end{aligned} \tag{3.31}$$

where the black terms in the relation represent known values of droplet thickness from previous iteration, the red terms are unknown values of droplet thickness from current iteration and lastly, the blue term at the end of the equation is known values of droplet thickness from previous time step, as shown in the Fig. 3.3:

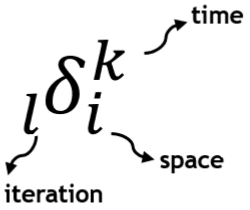

Figure 3.3: Representation of sub and superscripts.

After applying proper finite differences, Eq. (3.31) becomes the resulting implicit finite difference relation for the 4^{th}- order partial differential equation. As mentioned before, an iterative process between consecutive time steps is initiated with linearization of Eq. (3.25). At all time steps, droplet profile has to be guessed in order to start the iteration procedure. The most suitable guess for these black terms in Eq. (3.31) is the exact profile of the droplet from the previous time step. However, for the iteration of the first time step, there is no previous time, therefore, initial profile of the droplet is simply selected as the very first guess. At any time step, result of the current iteration and the previous iteration is compared with a relative convergence check, which will be named as "nonlinearity check" from now on. If the difference between them is sufficiently small, then current iteration is accepted as result. Rewriting Eq. (3.31) in a more compact way:

$$A_{l+1}\delta_{i-2}^{k} + B_{l+1}\delta_{i-1}^{k} + C_{l+1}\delta_{i}^{k} + D_{l+1}\delta_{i+1}^{k} + E_{l+1}\delta_{i+2}^{k} = \delta_{i}^{k-1} \tag{3.32}$$

Notice that in Eq. (3.31), there are 5 unknown nodes and one node is known from previous time step. These coefficients of five unknown nodes are denoted as A, B, C, D, E and they constitute the pentadiagonal matrix in our linear system:

$$\underbrace{\begin{bmatrix} C & D & E & 0 & \cdots & \cdots & \cdots & \cdots & 0 \\ B & C & D & E & \ddots & & & & \vdots \\ A & B & C & D & E & \ddots & & & \vdots \\ 0 & A & B & C & D & E & \ddots & & \vdots \\ \vdots & \ddots & \ddots & \ddots & \ddots & \ddots & \ddots & \ddots & \vdots \\ \vdots & & \ddots & A & B & C & D & E & 0 \\ \vdots & & & \ddots & A & B & C & D & E \\ \vdots & & & & \ddots & A & B & C & D \\ 0 & \cdots & \cdots & \cdots & \cdots & 0 & A & B & C \end{bmatrix}}_{\substack{\text{Coefficient matrix consisting of known} \\ \text{film thickness values} \\ \text{from previous time step}}} \underbrace{\begin{bmatrix} {}_{l+1}\delta_{0}^{k} \\ {}_{l+1}\delta_{1}^{k} \\ {}_{l+1}\delta_{2}^{k} \\ \vdots \\ \vdots \\ \vdots \\ {}_{l+1}\delta_{end-2}^{k} \\ {}_{l+1}\delta_{end-1}^{k} \\ {}_{l+1}\delta_{end}^{k} \end{bmatrix}}_{\substack{\text{Unknown linear terms} \\ \text{from current iteration}}} = \underbrace{\begin{bmatrix} \delta_{0}^{k} \\ \delta_{1}^{k} \\ \delta_{2}^{k} \\ \vdots \\ \vdots \\ \vdots \\ \delta_{end-2}^{k} \\ \delta_{end-1}^{k} \\ \delta_{end}^{k} \end{bmatrix}}_{\substack{\text{Known terms from} \\ \text{previous time step}}} \tag{3.33}$$

Introduced linear system is the result of our implicit finite difference scheme cast on to Eq. (3.15). Therefore, given system in Eq. (3.33) completely solves our 4^{th} order nonlinear partial differential equation for the droplet profile at each time step. Noticing that our coefficient matrix is also a sparse matrix consisting of zero terms except from main diagonals, it has to be treated with a special algorithm for effective computational time. Thomas algorithm can only be used with tridiagonal systems, however, it can be modified and its purpose can be extended for pentadiagonal systems as well.

The solution of Eq. (3.33) will give us the droplet profile result of the current iteration. This result is then compared with the result of the previous iteration with a nonlinearity check. If this check cannot be satisfied, iterative process continues. As soon as the nonlinearity check is satisfied, the droplet profile reached by the current iteration is accepted and admitted to upcoming convergence check. Total mass, i.e. cross sectional area for 2D droplets, must be preserved throughout each time step. Therefore, after passing the nonlinearity check, the area under the profile is calculated and compared against the area that must be conserved. If this relative area check is satisfied, then the droplet profile is finally found for that time step. However, if the area is not converged as expected, then a similar procedure is followed as in Section 3.3. Again Newton's Linear Interpolation method is utilized here for the step size in space. Δx, consequently the horizontal length of the droplet is slightly perturbed. Thus, conservation of area (i.e. mass) is satisfied, by shrinking or stretching the droplet length in horizontal axis. Although the solution procedure is narrated in brief, the implemented algorithm is presented with flowchart in Fig. B.2, and reader's review is strictly recommended. Moreover, different settings for droplet coalescence is covered in the following subsections.

3.4.1 Modelling the Coalescence of a Single Droplet with Symmetry Axis

Dynamic coalescence of droplets can be modelled in multiple ways. In this thesis study, we first decided to model the coalescence of a single droplet since it is relatively easier to work with. In this part, symmetry axis at $x = 0$ is used as an advantage in simulating droplet merging. It should also be reminded that a precursor film thickness is present at the symmetry axis, which is accepted to be equal to the thickness of the point next to it. Initial setting and the symmetry axis property is show in Fig. 3.4:

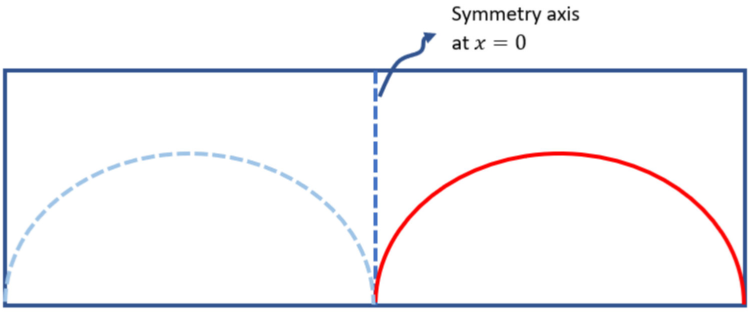

Figure 3.4: Representation of symmetry axis with initial droplet profile.

Initial condition is simply acquired from the droplet modelling part, Section 3.3:

$$t \quad = 0 \quad ; \qquad \delta(x) = \delta_o(x) \tag{3.34}$$

Boundary conditions are also somewhat straight forward for this setting:

$$\begin{aligned} &1) \quad x = 0 && ; \quad \frac{\partial \delta}{\partial x} = 0 \\ &2) \quad x = 0 && ; \quad \frac{\partial \delta^3}{\partial x^3} = 0 \\ &3) \quad x = L(t) && ; \quad \delta = 0 \\ &4) \quad x = L(t) && ; \quad \frac{\partial \delta}{\partial x} = \tan \alpha \end{aligned} \tag{3.35}$$

Where $L(t)$ is time dependent horizontal length of the droplet. Since MATLAB is used as the programming language throughout this thesis and it does not accept zero or negative index, our domain is started from node 1 and ended at node N, where N is the total number of nodes in our computational domain. Also, first and second boundary conditions are symmetry boundary conditions, therefore, central finite difference of order $\mathcal{O}(h^2)$ is applied. For the fourth boundary condition, however, backward finite difference of order $\mathcal{O}(h^2)$ is used. Then, rewriting boundary conditions in Eq. (3.35):

$$
\begin{array}{llll}
1)\;\; i=1 & ; \;\; \dfrac{\partial \delta}{\partial x}=0 & \rightarrow & \boxed{\delta_0=\delta_2} \\
2)\;\; i=1 & ; \;\; \dfrac{\partial \delta^3}{\partial x^3}=0 & \rightarrow & \boxed{\delta_{-1}=\delta_3} \\
3)\;\; i=N & ; \;\; \delta=0 & \rightarrow & \boxed{\delta_N=0} \\
4)\;\; i=N & ; \;\; \dfrac{\partial \delta}{\partial x}=\tan(\pi-\alpha) & \rightarrow & \boxed{\delta_{N-1}=\dfrac{\delta_{N-2}}{4}-\dfrac{\Delta x\tan(\pi-\alpha)}{2}}
\end{array}
\tag{3.36}
$$

Notice that while the first boundary condition in Eq. (3.36) represents the symmetry between two merging droplets, the second boundary condition follows from the mass conservation during the coalescence process. Third and fourth boundary conditions represent the film thickness at end of the domain and the static contact angle, respectively. Additionally, last two boundary conditions imply that we have the information of last two nodes, $N-1$ and N at all times. Our general relation Eq. (3.31) is utilized together with the boundary conditions given above to determine the coefficients of first and last two rows of our coefficient matrix. In order not to disturb the flow of the text, these relations will be presented in detail in the Appendix A.1.

In Appendix A.1, the black terms given with A.1 and A.2 create first two rows of our coefficient matrix. Although the coefficients of first and last two rows of pentadiagonal matrix is different, there will not be any alteration regarding the inner rows; they are still represented by Eq. (3.31).

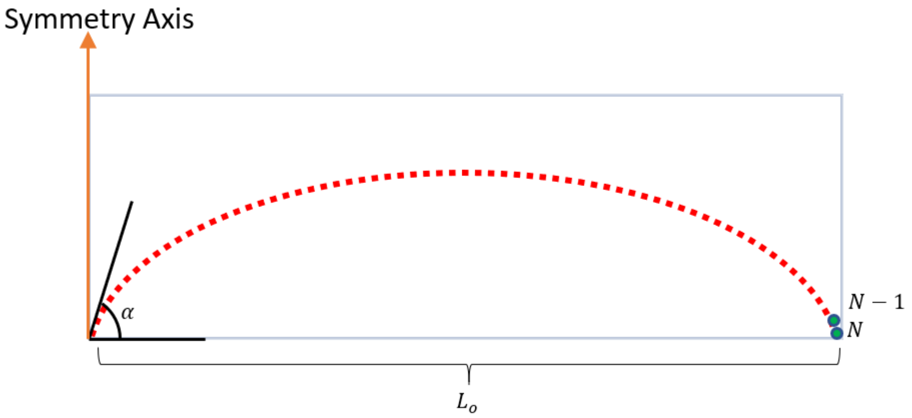

Figure 3.5: Nodes $N-1$ and N are known from boundary conditions at all times.

For the equations presented in Appendix A.1, ${}_l\zeta_0^k$, ${}_l\zeta_1^k$, ${}_l\zeta_{N-2}^k$ and ${}_l\zeta_{N-1}^k$ differ from the usual relation ${}_l\zeta_i^k$, such as:

$$ {}_l\zeta_i^k = \frac{1}{\left[1 + \left(\dfrac{{}_l\delta_{i+1}^k - {}_l\delta_{i-1}^k}{2\Delta x}\right)^2\right]^{3/2}} \tag{3.37} $$

$$ {}_l\zeta_0^k = \frac{1}{\left[1 + \left(\dfrac{{}_l\delta_1^k - {}_l\delta_{-1}^k}{2\Delta x}\right)^2\right]^{3/2}} = \frac{1}{\left[1 + \left(\dfrac{{}_l\delta_1^k - {}_l\delta_3^k}{2\Delta x}\right)^2\right]^{3/2}} \tag{3.38} $$

$$ {}_l\zeta_1^k = \frac{1}{\left[1 + \left(\dfrac{{}_l\delta_2^k - {}_l\delta_0^k}{2\Delta x}\right)^2\right]^{3/2}} = 1 \tag{3.39} $$

$$ {}_l\zeta_{N-2}^k = \frac{1}{\left[1 + \left(\dfrac{{}_l\delta_{N-1}^k - {}_l\delta_{N-3}^k}{2\Delta x}\right)^2\right]^{3/2}} \tag{3.40} $$

$$ {}_l\zeta_{N-1}^k = \frac{1}{\left[1 + \left(\dfrac{{}_l\delta_N^k - {}_l\delta_{N-2}^k}{2\Delta x}\right)^2\right]^{3/2}} = \frac{1}{\left[1 + \left(\dfrac{-{}_l\delta_{N-2}^k}{2\Delta x}\right)^2\right]^{3/2}} \tag{3.41} $$

Eqs. (3.36) to (3.41) and (A.1) to (A.4) fully define the coefficient matrix needed to solve the dynamic equation of coalescence simulation of a single droplet with symmetry axis. A similar procedure will be presented in the next section. Corresponding results will be presented in the next chapter.

3.4.2 Modelling the Coalescence of Two Identical Droplets

In this subsection, two identical droplets are first created by following the procedure argued in Section 3.3, and then they merged into one bigger drop. Schematic of the setting is given in Fig. 3.6:

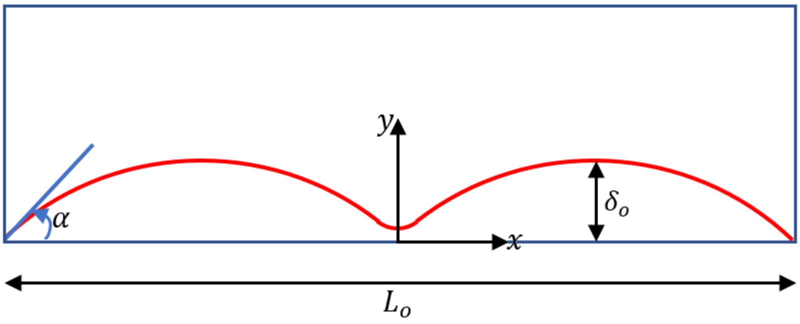

Figure 3.6: Schematic of the initial profile of two exact droplets, ready for coalescence.

Both droplets have same initial length of $L_o/2$, same contact angle of α and same initial maximum height of δ_o. Recall also that droplets are already and barely in contact with each other (exaggerated in the Fig. 3.6) to avoid the singular movement occurring at the center line between drops. The initial bridge height is equal to the film thickness values of prior and subsequent nodes, which corresponds to one order of magnitude smaller value than the maximum thickness of the droplet. Due to the nature of the implemented finite difference method, different set of boundary conditions are applied, while the initial condition is same as before:

$$t = 0 \qquad ; \quad \delta(x) = \delta_o(x) \tag{3.42}$$

and,

$$\begin{aligned}
&1) \quad x = -L(t) \qquad &&; \quad \delta = 0 \\
&2) \quad x = -L(t) \qquad &&; \quad \frac{\partial \delta}{\partial x} = \tan \alpha \\
&3) \quad x = L(t) \qquad &&; \quad \delta = 0 \\
&4) \quad x = L(t) \qquad &&; \quad \frac{\partial \delta}{\partial x} = \tan(\pi - \alpha)
\end{aligned} \tag{3.43}$$

where $L(t)$ is the time dependent droplet length. Right at the middle slight necking is already started. Since nodes 1 and 2 as well as nodes $N-1$ and N are known at each time step, they are not included in the solution matrix, therefore, solution domain only includes nodes from 3 to $N-2$. At this point, another complication is faced, the coefficient matrix simply cannot start from the third node in MATLAB. Following relations will cover the domain starting from node 3 to node $N-2$, however, in order to overcome aforementioned problem, the whole solution domain is shifted towards left in MATLAB programming. This means that in MATLAB codes, domain is forcibly started from node 1 and ended at node $N-4$, which in physical equations these nodes correspond to node 3 and $N-2$ respectively.

Also, for the first boundary condition forward finite difference scheme of order $\mathcal{O}(h^2)$ and for the fourth boundary condition backward finite difference of order $\mathcal{O}(h^2)$ is used. Then, rewriting boundary conditions in Eq. (3.35):

$$\begin{aligned}
&1)\quad i=1 \quad ; \quad \delta=0 && \rightarrow \quad \boxed{\delta_1=0} \\
&2)\quad i=1 \quad ; \quad \frac{\partial\delta}{\partial x}=\tan(\alpha) && \rightarrow \quad \boxed{\delta_2=\frac{\delta_3}{4}+\frac{\Delta x\tan(\alpha)}{2}} \\
&3)\quad i=N \quad ; \quad \delta=0 && \rightarrow \quad \boxed{\delta_N=0} \\
&4)\quad i=N \quad ; \quad \frac{\partial\delta}{\partial x}=\tan(\pi-\alpha) && \rightarrow \quad \boxed{\delta_{N-1}=\frac{\delta_{N-2}}{4}-\frac{\Delta x\tan(\pi-\alpha)}{2}}
\end{aligned} \tag{3.44}$$

In this setting, first and second boundary conditions are changed since the boundary is moved from the symmetry axis to the left side of the first droplet. Thus, first and second boundary conditions represent the film thickness at the end of the domain and the contact angle respectively just like third and fourth boundary conditions. First two and last two boundary conditions again also imply that we have the information of these nodes, 1, 2, $N-1$ and N at all times. Considering the small neck created between drops prior to coalescence, if we have 1001 total nodes, 4 of them are always known, therefore, our linear system is solved for 997 unknowns in each loop. Our general relation Eq. (3.31) is once again utilized together with the boundary conditions given above, and the coefficients of first and last two rows of our coefficient matrix is determined. In order not to disturb the flow of the text, these relations will be presented in detail in the Appendix A.2.

The black terms in relations A.5 and A.6 create first two rows of our coefficient matrix. Although the coefficients of first and last two rows of pentadiagonal matrix is different, there will not be any alteration regarding the inner rows; they are still represented by Eq. (3.31).

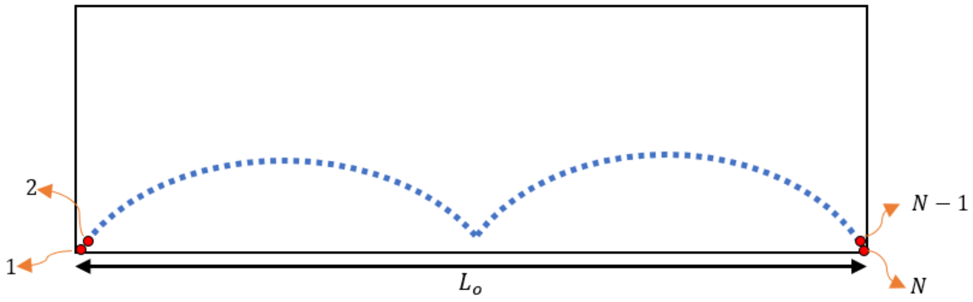

Figure 3.7: Nodes 1, 2, $N-1$ and N are known from boundary conditions at all times.

In above equations, ${}_l\zeta_2^k$, ${}_l\zeta_3^k$, ${}_l\zeta_{N-2}^k$ and ${}_l\zeta_{N-1}^k$ will differ from the usual relation ${}_l\zeta_i^k$, such as:

$${}_l\zeta_i^k = \frac{1}{\left[1+\left(\frac{{}_l\delta_{i+1}^k - {}_l\delta_{i-1}^k}{2\Delta x}\right)^2\right]^{3/2}} \tag{3.45}$$

$${}_l\zeta_2^k = \frac{1}{\left[1+\left(\frac{{}_l\delta_{3}^k - {}_l\delta_{1}^k}{2\Delta x}\right)^2\right]^{3/2}} = \frac{1}{\left[1+\left(\frac{{}_l\delta_{3}^k}{2\Delta x}\right)^2\right]^{3/2}} \tag{3.46}$$

$${}_l\zeta_3^k = \frac{1}{\left[1+\left(\frac{{}_l\delta_{4}^k - {}_l\delta_{2}^k}{2\Delta x}\right)^2\right]^{3/2}} \tag{3.47}$$

$${}_l\zeta_{N-2}^k = \frac{1}{\left[1+\left(\frac{{}_l\delta_{N-1}^k - {}_l\delta_{N-3}^k}{2\Delta x}\right)^2\right]^{3/2}} \tag{3.48}$$

$${}_l\zeta_{N-1}^k = \frac{1}{\left[1+\left(\frac{{}_l\delta_{N}^k - {}_l\delta_{N-2}^k}{2\Delta x}\right)^2\right]^{3/2}} = \frac{1}{\left[1+\left(\frac{-{}_l\delta_{N-2}^k}{2\Delta x}\right)^2\right]^{3/2}} \tag{3.49}$$

Eqs. (3.44) to (3.49) and (A.5) to (A.8) completely define the coefficient matrix needed to solve the dynamic equation of coalescence simulation of two identical droplets. At the end of each iteration, first and last two nodes are added to the found profile, in order to calculate the corresponding cross sectional area. Whether the following area check is passed or failed, these four nodes are again eliminated from the profile. Results and thorough discussion will be made in the following chapter.

3.4.3 Modelling the Coalescence of Two Different Radii Droplets

Arguments that are going to be presented in this section will not be much different than to those presented in Section 3.4.2. Instead of two same droplets, different radii droplets were first created, then coalesced within the viscous regime. Full equations for first two, intermediate and last two rows of our coefficient matrix will not be presented here as they were covered in previous subsections, because these will be identical to what was presented in Section 3.4.2. Thus once again, Eqs. (3.44) to (3.49) and (A.5) to (A.8) define the coefficient matrix for the coalescence simulation of two different radii droplets. Only difference between the coalescence of same droplets and coalescence of different radii droplets is the creation of the initial droplet profiles. In Section 3.3, it is mentioned that the initial droplet profile is either created via converging to a predetermined area or to a predetermined horizontal length. When dealing with different radii droplets, one must work with the same spatial resolution, Δx, through out the domain of interest. Predetermined area or the predetermined horizontal length of the second droplet is determined proportionately with the first droplet. Selecting area as convergence criterion is not practical, since the total number of nodes of second droplet cannot be controlled. Instead, selecting horizontal length as convergence criterion is somewhat flexible, e.g. if we have $1:3$ proportion for the horizontal length of two different droplets, then this proportion also reflected upon the total node number of each droplet.

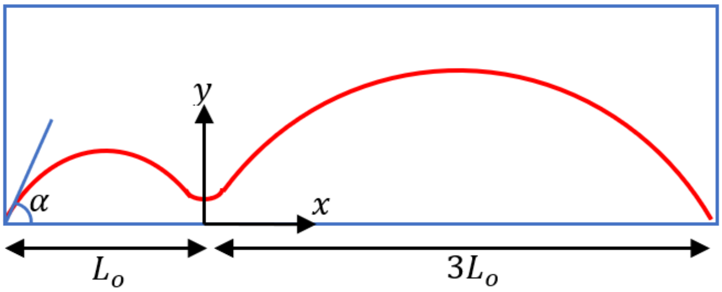

Figure 3.8: Sample schematic of the initial profile of two different (with proportion of $1:3$ horizontal length) droplets, ready to coalesce.

3.4.4 Non-dimensionalization of Governing Equations

In sections 3.2 to 3.4, all the terms in relations for the droplet modelling and the dynamic coalescence are presented in accordance with dimensional parameters. However, in order make proper physical interpretations and to observe dependencies of simulations, performing a non-dimensional analysis is crucial. There are different options to non-dimensionalize the governing equations, yet certain scales and respective non-dimensional groups are selected. Consider the following non-dimensional parameters:

$$x^* = \frac{x}{L_o} \tag{3.50}$$

and,

$$\delta^* = \frac{\delta}{\delta_o} \tag{3.51}$$

where L_o is the characteristic length scale of our droplet or thin film, and δ_o is the characteristic droplet height. Since we are utilizing the lubrication assumption (or thin film assumption), droplet thickness scale is sufficiently smaller than the length scale presented in above relations, thus, one may state their ratio as:

$$\epsilon = \frac{\delta_o}{L_o} \ll 1 \tag{3.52}$$

3.4.4.1 Non-dimensionalization of Young-Laplace Equation

Modelling of the droplet is achieved by solving the differential equation regarding the pressure difference given in Eq. (3.18). Pressure term can be non-dimensionalized by

$$P^* = \frac{P}{P_o} \tag{3.53}$$

Considering that the first derivative of the film thickness, δ', is already dimensionless, and using non-dimensional parameters introduced in Eqs. (3.50), (3.51) and (3.53) together with the Eq. (3.18)

$$\frac{\delta_o}{L_o^2}\frac{\partial^2 \delta^*}{\partial x^{*2}} = \frac{P_o \Delta P^*}{\sigma}\left[1+\frac{\partial \delta^*}{\partial x^*}\right]^{3/2} + \frac{\rho g \delta_o}{\sigma}\left[1+\frac{\partial \delta^*}{\partial x^*}\right]^{3/2}\delta^* \tag{3.54}$$

then further manipulation leads to

$$\frac{\partial^2 \delta^*}{\partial x^{*2}} = \frac{P_o L_o^2 \Delta P^*}{\sigma \delta_o}\left[1+\frac{\partial \delta^*}{\partial x^*}\right]^{3/2} + \frac{\rho g L_o^2}{\sigma}\left[1+\frac{\partial \delta^*}{\partial x^*}\right]^{3/2}\delta^* \tag{3.55}$$

where from the first non-dimensional group on the right hand side, the pressure scale is found as

$$P_o = \frac{\sigma \delta_o}{L_o^2} \tag{3.56}$$

consequently, non-dimensional modelling of a droplet can be reached with

$$\frac{\partial^2 \delta^*}{\partial x^{*2}} = \Delta P^*\left[1+\frac{\partial \delta^*}{\partial x^*}\right]^{3/2} + Bo\left[1+\frac{\partial \delta^*}{\partial x^*}\right]^{3/2}\delta^* \tag{3.57}$$

In Eq. (3.57), Bond number (Bo) represents a dimensionless number which is the indicator of the importance of the ratio of gravitational forces to the surface tension forces.

This finding is rather important, because this is the first parameter that dynamic coalescence simulations depend on. In Chapter 4, droplet models with different Bond numbers will take place, and its effects will be discussed extensively.

3.4.4.2 Non-dimensionalization of Reynolds Equation

Although parametric equations regarding the coalescence represent real life cases, simulating non-dimensional settings offers more intuitive approach towards dependencies. Since coalescence of droplets is an unsteady process, time also needs to be non-dimensionalized, yet the time scale t_o is unknown *a priori*,

$$t^* = \frac{t}{t_o} \tag{3.58}$$

where t_o will be found through the non-dimensionalization process. Consider again the same non-dimensional parameters given in Eqs. (3.50), (3.51) and (3.53) together with the Reynolds Eqn. (3.27). Non-dimensional representation becomes:

$$\frac{\delta_o}{t_o}\frac{d\delta^*}{dt^*} - \frac{\delta_o}{t_o}\frac{\partial\delta^*}{\partial x^*}\frac{dx^*}{dt^*} = \frac{\sigma}{3\mu L_o}\frac{\partial}{\partial x^*}\left\{\frac{\delta_o^3}{L_o}\delta^{*3}\frac{\partial}{\partial x^*}\left[\frac{\delta_o}{L_o^2}\zeta\frac{\partial^2\delta^*}{\partial x^{*2}} + \rho g\delta_o\delta^*\right]\right\} \tag{3.59}$$

where the term f only includes the first derivative of the film thickness, and it was readily stated that it is non-dimensional. Moreover, minus sign in front of the surface tension, σ, bears no significance in non-dimensional analysis, therefore, it is ignored. Further rearranging the above relation and equating the first non-dimensional group on the right hand side to unity, the following non-dimensional scale for the time is reached:

$$\frac{\sigma\delta_o^4 t_o}{3\mu L_o^4\delta_o} = 1 \longrightarrow t_o = \frac{3\mu L_o^4}{\sigma\delta_o^3} \tag{3.60}$$

and the non-dimensional unsteady Reynolds equation becomes,

$$\frac{d\delta^*}{dt^*} - \frac{\partial \delta^*}{\partial x^*}\frac{dx^*}{dt^*} = \frac{\partial}{\partial x^*}\left\{\delta^{*3}\frac{\partial}{\partial x^*}\left[\zeta\frac{\partial^2 \delta^*}{\partial x^{*2}} + Bo\delta^*\right]\right\} \tag{3.61}$$

Eq. (3.61) is the main non-dimensional equation that governs the coalescence of droplets and it is used extensively in this thesis study. Bond number once again appears in the equations, therefore, coalescence simulations also depend on this value. Notice also that unlike most of the studies in the literature gravity is not disregarded; this is the reason Bond number appears in our non-dimensional equations.

Boundary conditions also needs to be non-dimensional. Examining all the boundary conditions in Sections 3.4.1 to 3.4.3, only dependency is for the contact angle of the droplet, α. Hence, it is concluded that droplet coalescence should only be a function of the Bond number, Bo, and the contact angle, α. In the following chapter, these dependencies will be investigated further.

CHAPTER 4

NUMERICAL RESULTS FOR MERGING SIMULATIONS AND DISCUSSIONS

Two dimensional droplet modelling and various droplet coalescence scenarios were numerically analysed in Chapter 3. Both dimensional and non-dimensional results of these analyses will be presented and investigated in detail within this chapter. Since this thesis study focuses only on fully wetting 2D cylindrical droplets, contact angle that the droplet makes with the surface has to be in the interval $0 < \alpha < \pi/2$.

4.1 Coalescence Simulations and Validation within the Literature

Various dimensional merging simulations are conducted to meet real life instances, and the results are presented under this section. Although the possibilities of fluid-substrate pairs are countless, only a number of them are investigated in this section. In accordance with these information, coalescence of water, R-134a and methanol on different materials are analyzed. Properties of the investigated fluids with the corresponding substrate are given in the below table:

Table 4.1: Fluid – Substrate pairs used in dimensional simulations.

Fluid – Substrate	T (°C)	ρ (kg/m^3)	μ (Pa·s)	σ (N/m)	α (°)
Water – Copper	25	1000	8.89e-4	0.07275	72
R-134a – Aluminium	20	1225.5	2.12e-4	0.00892	8.1

where density, dynamic viscosity and surface tension are properties of the fluid and the contact angle is the angle formed at the triple line on gas, fluid, and solid substrate. Note that while air is the gas medium for water–copper setting, R-134a liquid surrounded by R-134a vapor on an aluminum substrate. The contact angle value at first row of fluid-substrate pairs is taken from [32] and the data on second row is obtained from [33]. It is experimentally practiced in [32–36] that the apparent contact angle of fluids given in Table 4.1 highly depend on number of parameters. While increasing the temperature or including surfactants reduce the contact angle of the fluid, polishing the surface tends to increase the contact angle. Therefore, contact angle values given with Table 4.1 are nothing but experimental estimations, and they are subject to change with the minute differences in the experimental setting. Furthermore, since the simulations are covered thoroughly under the Section 4.2, analysing the pairs given in Table 4.1 would suffice in terms of demonstration. For two different initial length values, fluid-substrate pairs in Table 4.1 are simulated, and results are shared below.

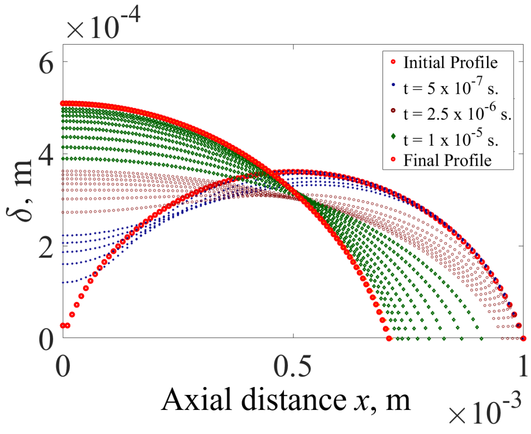

(a)

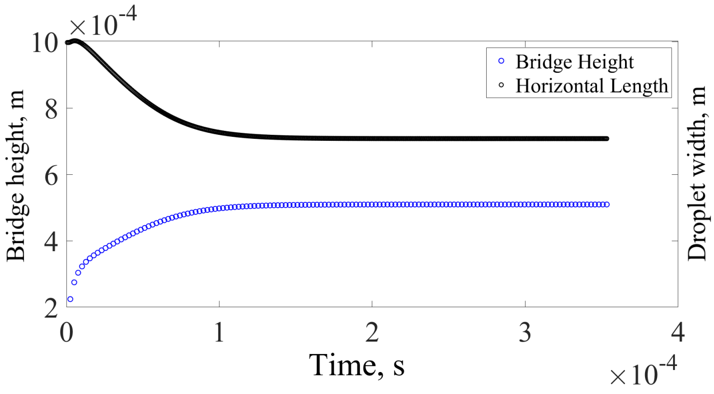

(b)

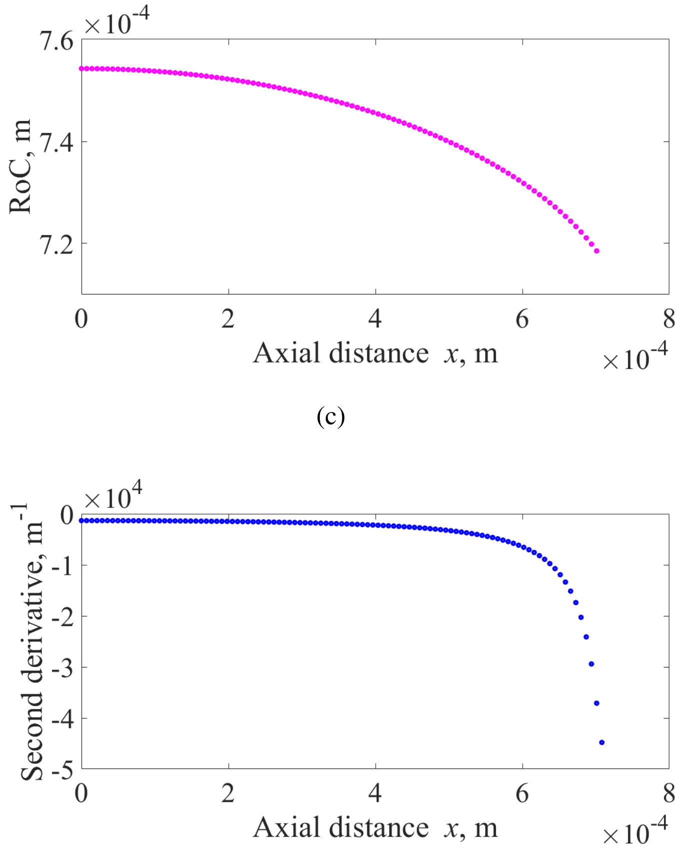

(c)

(d)

Figure 4.1: Coalescence results for water-copper pair. Initial drop has $L_o = 10^{-3}$ m. Plots for (a) time evolution of the droplet, (b) bridge height and merged droplet size variation in time, (c) radius of curvature and (d) second derivative at the steady state.

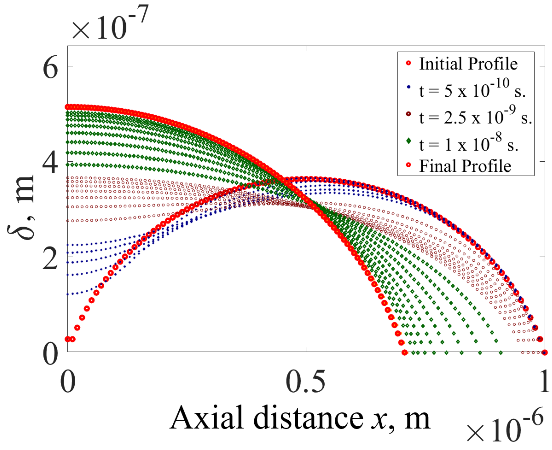

(a)

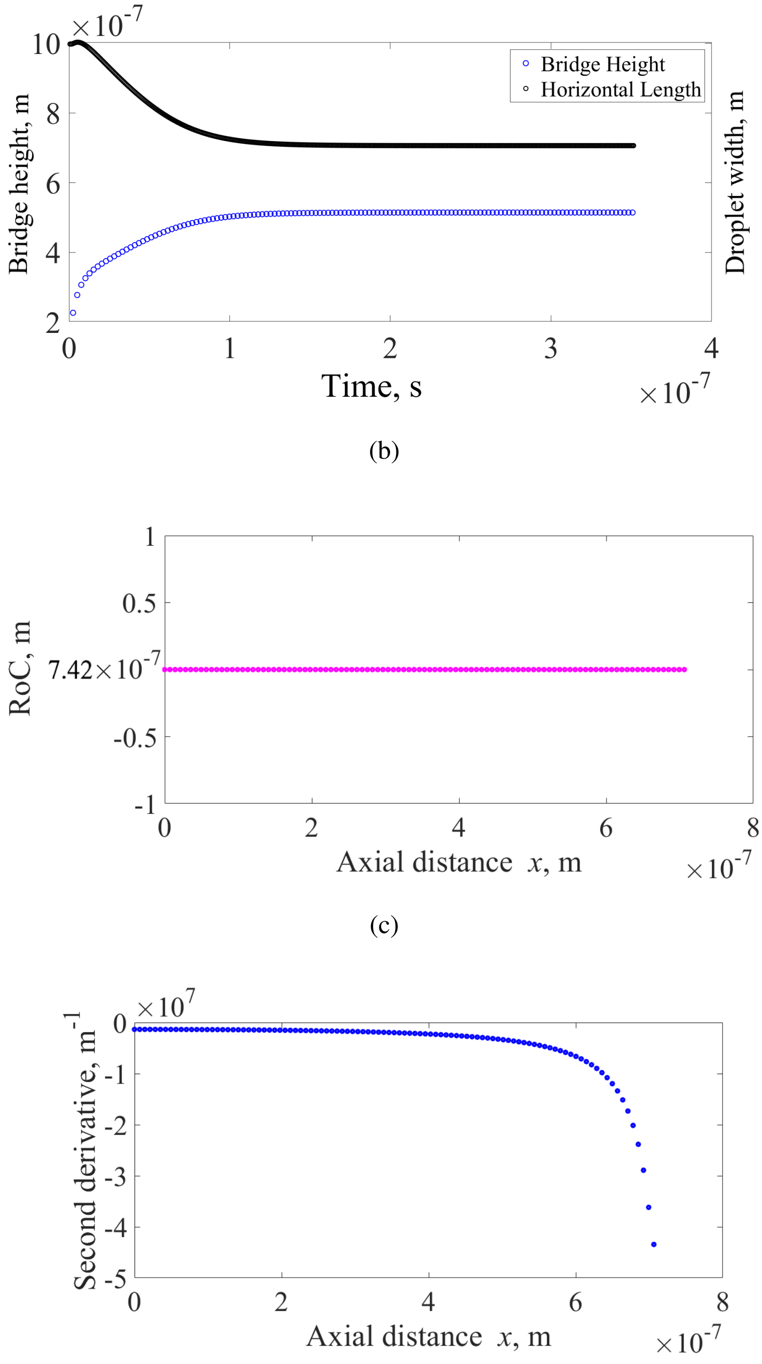

(b)

(c)

(d)

Figure 4.2: Coalescence results for water-copper pair. Initial drop has $L_o = 10^{-6}$ m. Plots for (a) time evolution of the droplet, (b) bridge height and merged droplet size variation in time, (c) radius of curvature and (d) second derivative at the steady state.

By examining the figures presented above, it is easily observed that there is a scale between the initial horizontal length of the droplet and the time to reach steady state. As the initial length is reduced, time to reach the steady state is also decreased. Another immediate observation in Fig. 4.2 is that the radius of curvature values at each spatial location at the steady state barely changes throughout the droplet profile, thus, it is depicted as a constant line. In Fig. 4.2-(c), the difference between each node are at the order of 10^{-16}. On the other hand, radius of curvature values considerably vary in Fig. 4.1-(c). This comparison indicates that the effect of gravity is decreased on smaller droplets. Same results are achieved with the coalescence simulations of two identical droplets.

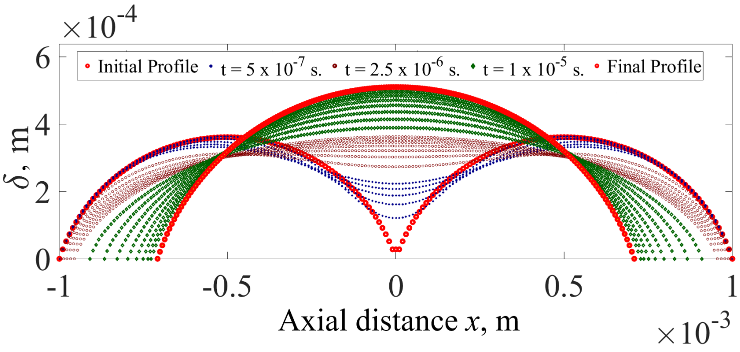

(a)

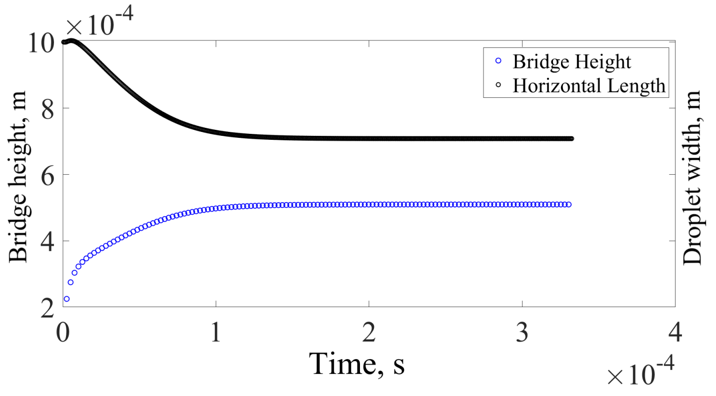

(b)

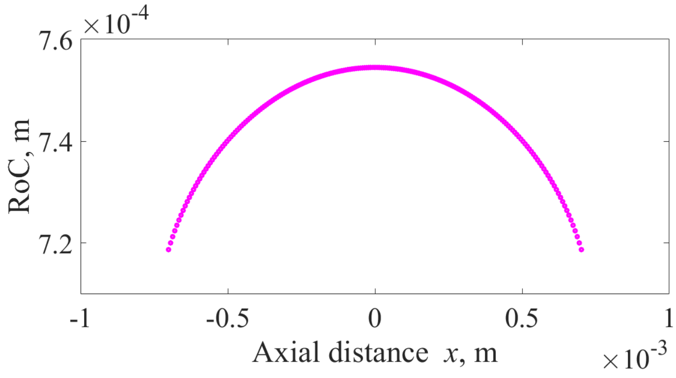

(c)

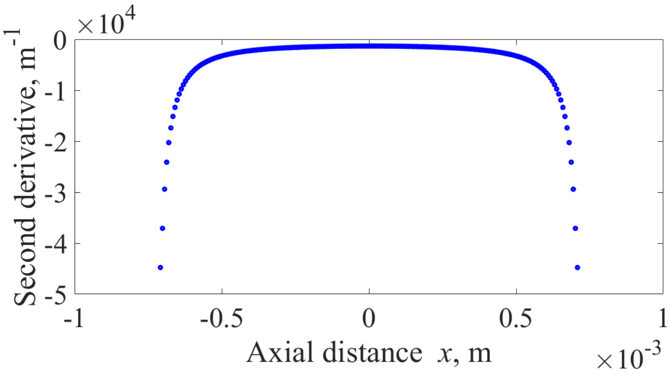

(d)

Figure 4.3: Coalescence results for water-copper pair. Each drop has $L_o = 10^{-3}$ m. Plots for (a) time evolution of the droplet, (b) bridge height and merged droplet size variation in time, (c) radius of curvature and (d) second derivative at the steady state.

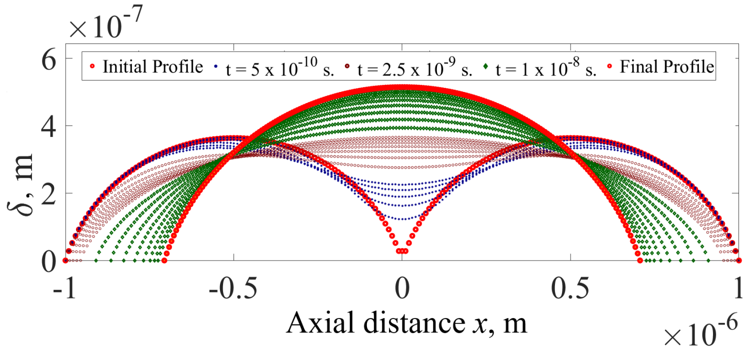

(a)

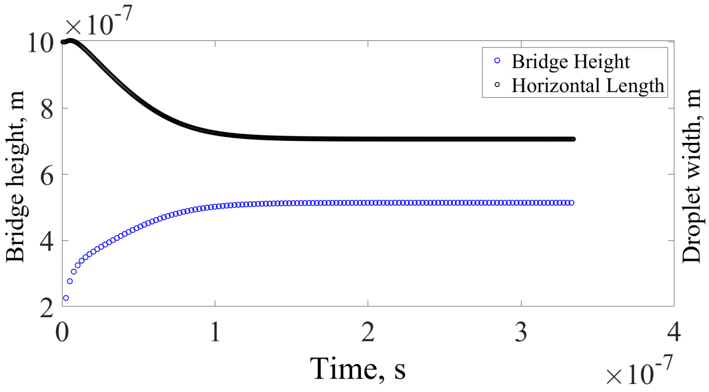

(b)

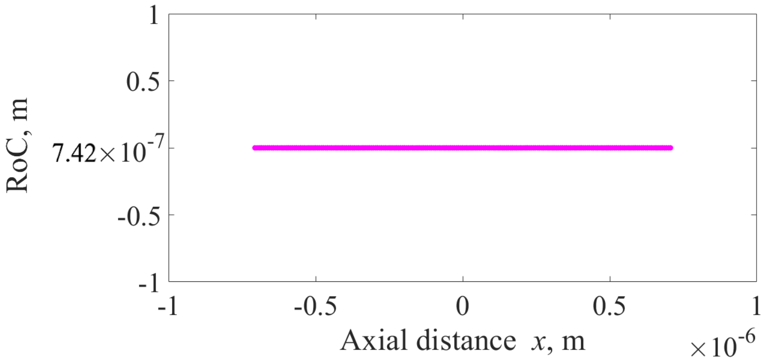

(c)

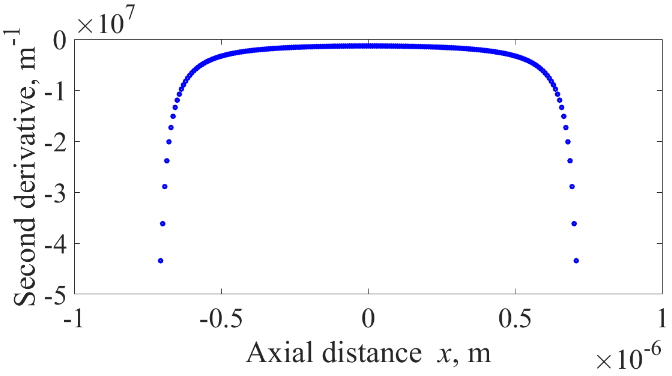

(d)

Figure 4.4: Coalescence results for water-copper pair. Each drop has $L_o = 10^{-6}$ m. Plots for (a) time evolution of the droplet, (b) bridge height and merged droplet size variation in time, (c) radius of curvature and (d) second derivative at the steady state.

In all the simulations, the bridge height and the length of the merged droplet reaches steady state at the same time as expected. It should also be pointed out that the droplet evolution happens rather quickly at the early stages of coalescence comparing to the later stages. Following water–copper results, R-134a droplets on aluminum surface are examined below. Since the contact angle between the R-134a droplet and the aluminum surface is very small, coalescence results given with Figs. 4.5 to 4.8 could not be presented with the same scale on both axes, as it would make it impossible to read the figures.

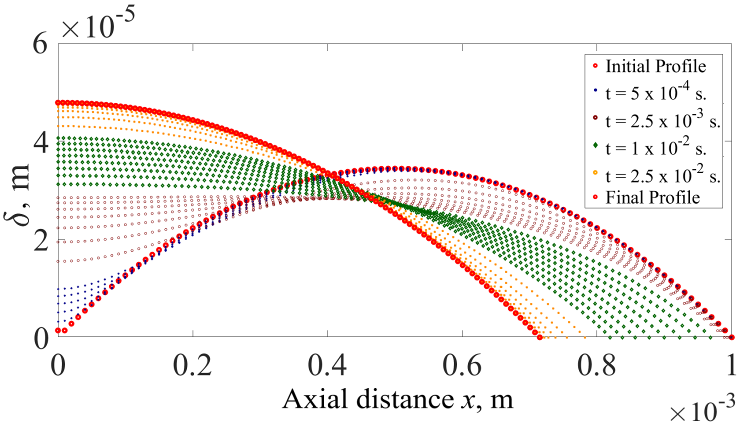

(a)

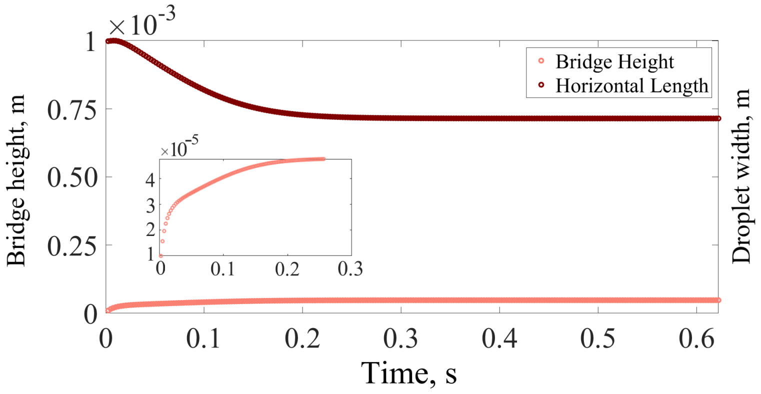

(b)

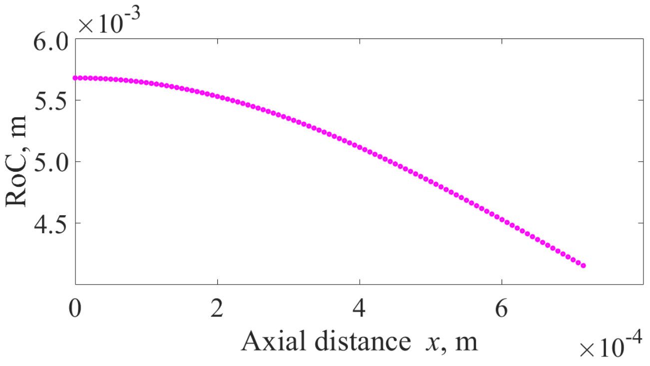

(c)

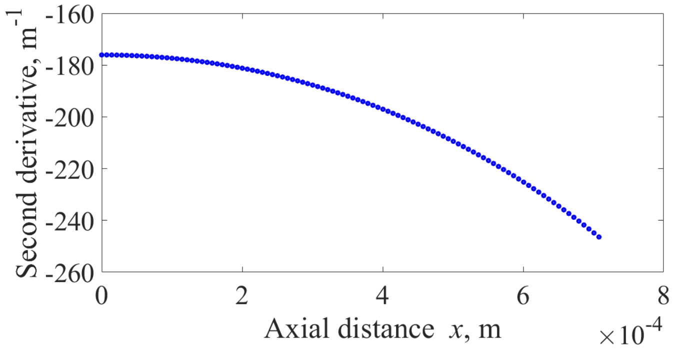

(d)

Figure 4.5: Coalescence results for R-134a–aluminium pair. Initial drop has $L_o = 10^{-3}$ m. Plots for (a) time evolution of the droplet, (b) bridge height and merged droplet size variation in time, (c) radius of curvature and (d) second derivative at the steady state.

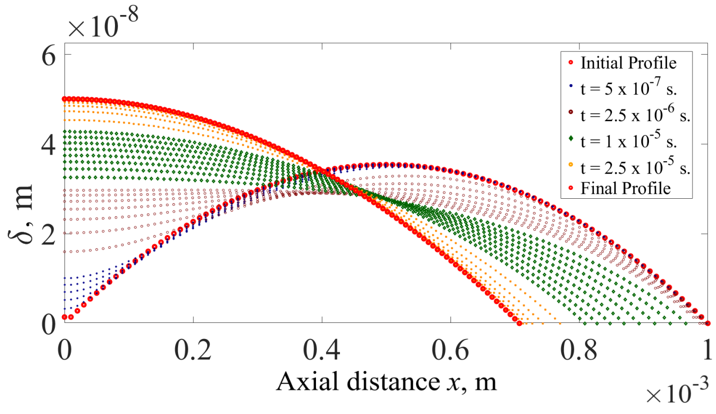

(a)

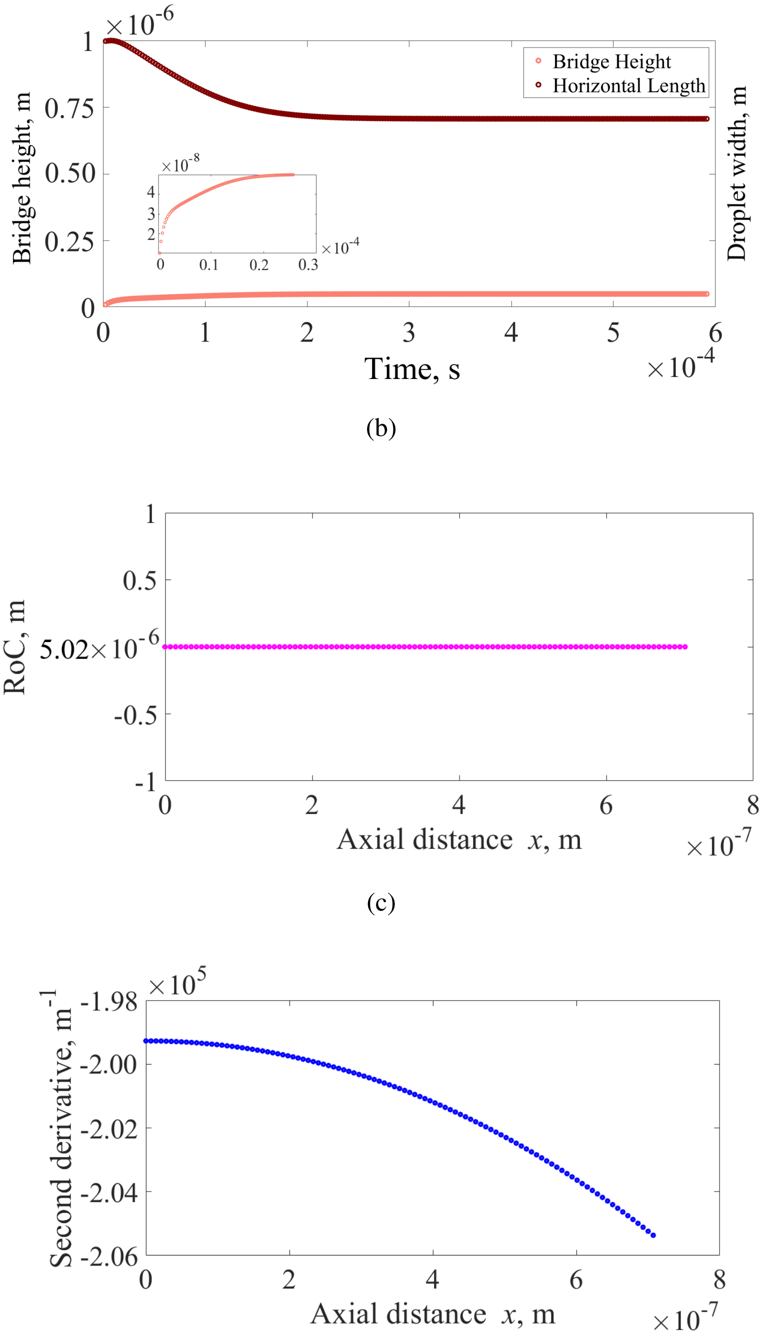

(b)

(c)

(d)

Figure 4.6: Coalescence results for R-134a–aluminium pair. Initial drop has $L_o = 10^{-6}$ m. Plots for (a) time evolution of the droplet, (b) bridge height and merged droplet size variation in time, (c) radius of curvature and (d) second derivative at the steady state.

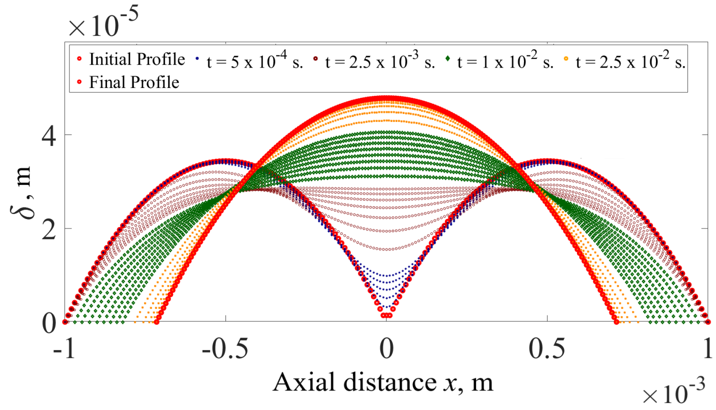
×10^-5
Initial Profile
t = 5 x 10^-4 s.
t = 2.5 x 10^-3 s.
t = 1 x 10^-2 s.
t = 2.5 x 10^-2 s.
Final Profile
δ, m
4
2
0
-1
-0.5
0
0.5
1
Axial distance x, m
×10^-3

(a)

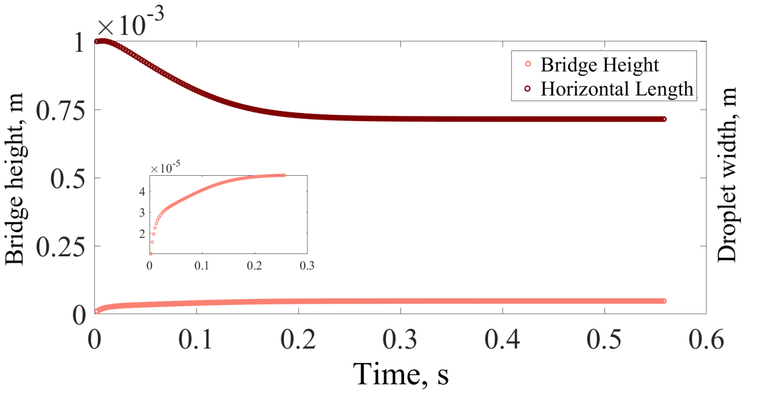
×10^-3
1
0.75
0.5
0.25
0
Bridge height, m
Bridge Height
Horizontal Length
Droplet width, m
×10^-5
4
3
2
0
0.1
0.2
0.3
0
0.1
0.2
0.3
0.4
0.5
0.6
Time, s

(b)

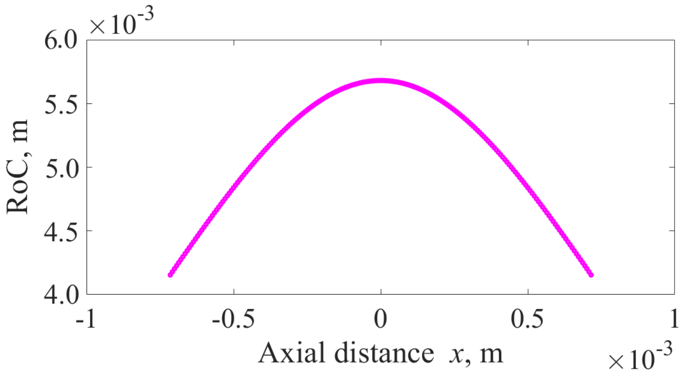
×10^-3
6.0
5.5
5.0
4.5
4.0
RoC, m
-1
-0.5
0
0.5
1
Axial distance x, m
×10^-3

(c)

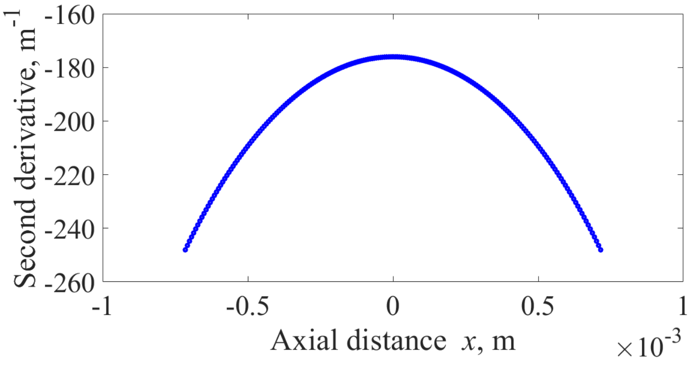

(d)

Figure 4.7: Coalescence results for R-134a–aluminium pair. Each drop has $L_o = 10^{-3}$ m. Plots for (a) time evolution of the droplet, (b) bridge height and merged droplet size variation in time, (c) radius of curvature and (d) second derivative at the steady state.

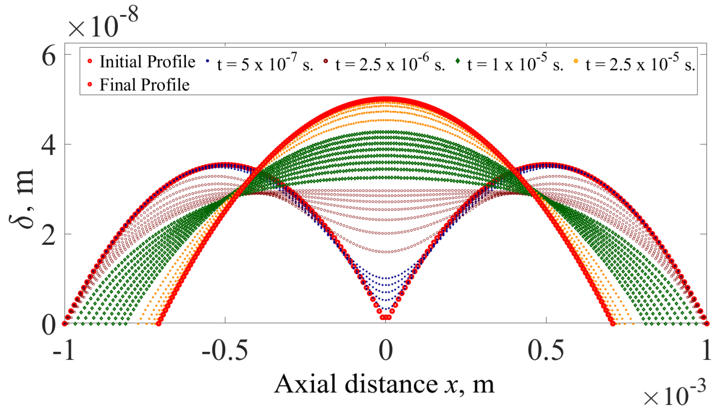

(a)

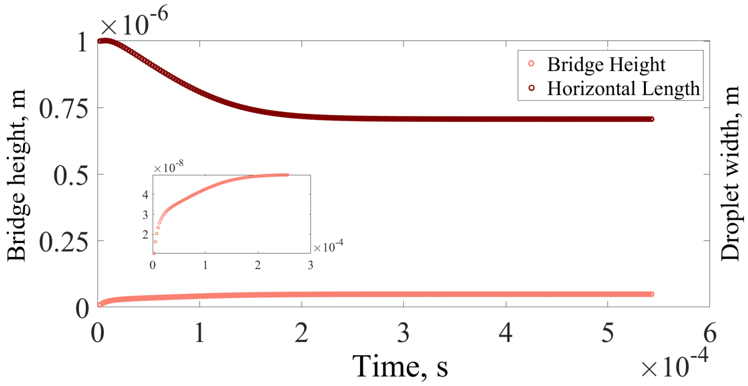

(b)

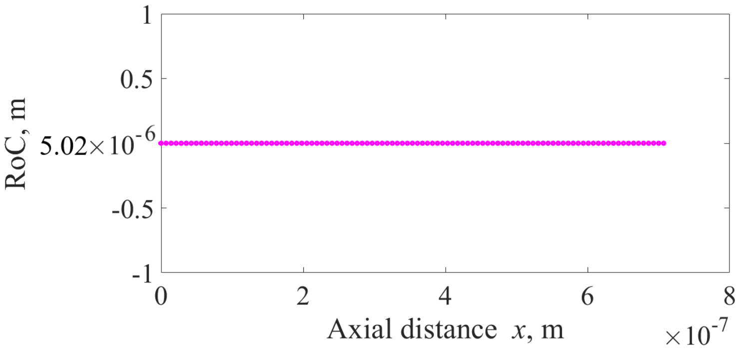

(c)

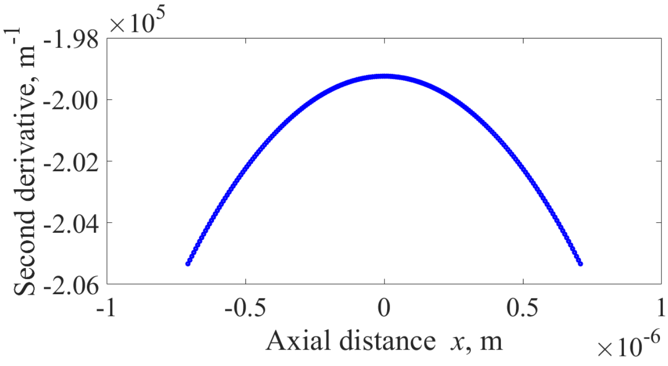

(d)

Figure 4.8: Coalescence results for R-134a–aluminium pair. Each drop has $L_o = 10^{-6}$ m. Plots for (a) time evolution of the droplet, (b) bridge height and merged droplet size variation in time, (c) radius of curvature and (d) second derivative at the steady state.

It is immediately observed upon comparison of the coalescence simulations of water–copper and R-134a–aluminum settings that R-134a droplets merge much slower than the water droplets. This is mainly due to the difference between the contact angles. However, simulations are also heavily dependent on surface tension and viscosity as expected.

In order to emphasize the effect of gravity on droplets and the coalescence processes, the time evolution of relatively larger water droplets on a copper surface is investigated with three different gravity values. Coalescence simulation of 5 mm droplets under normal gravity are selected to be the reference case, and negative gravity and zero-gravity cases are solved accordingly. The initial and the final shapes are compared in the following figures.

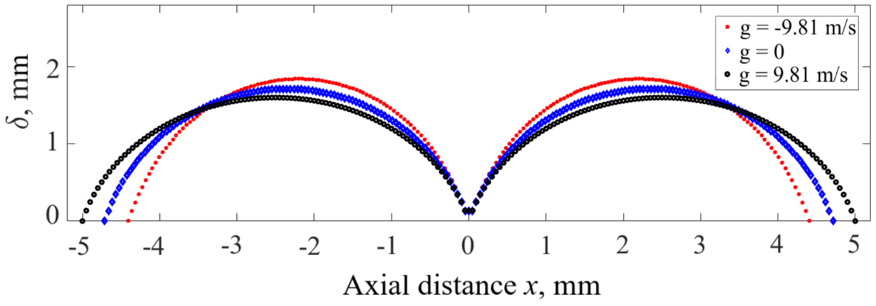

(a)

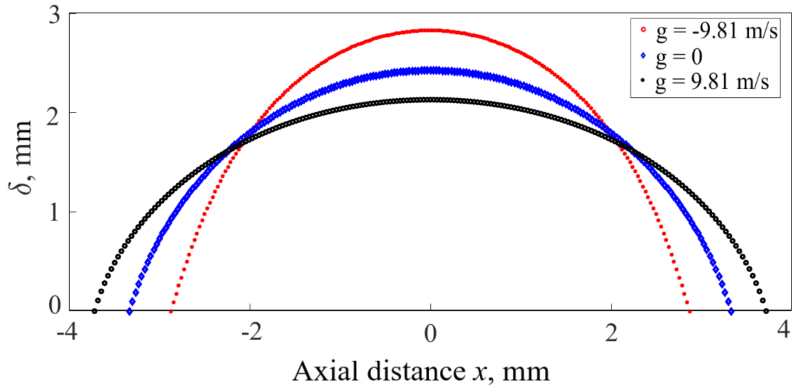

(b)

Figure 4.9: The effect of gravity on two identical water droplets on copper surface where $\alpha = 72°$ a) Initial shapes, (b) shapes after coalescence.

In Fig. 4.9, the cross-sectional areas of the created droplets under the effect of negative, zero and positive gravity are equal. Thus, the influence of the gravity on the maximum film thickness and the axial length can be readily observed. In this first figure, droplets are more compressed as the direction of gravity is altered from a droplet on a flat surface, a positive gravity, to one where the droplet surface faces earth, a negative gravity case. Similar to the differences occurring in the initial droplet shapes, same effects are observed for the film thickness variations when the steady state is reached. Moreover, the apparent retraction of the merged droplet length is greater with the negative gravity case since gravity also contributes the flattening of the droplet dome. Time dependent bridge height and droplet size variation is also given in Fig. 4.10

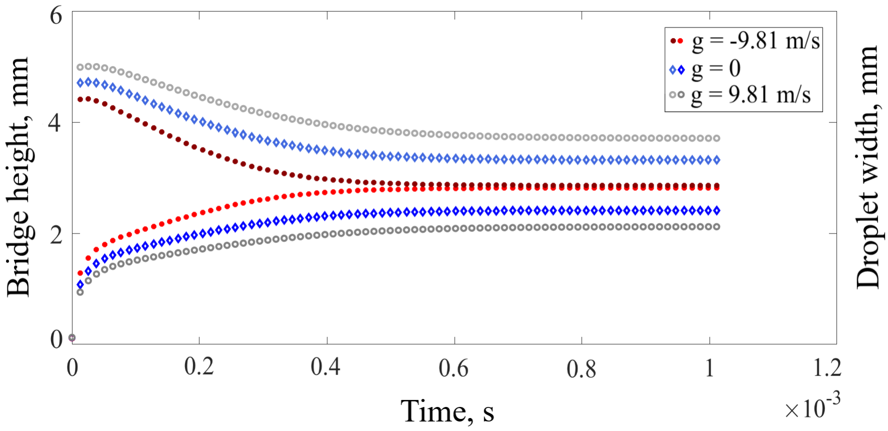

Figure 4.10: Bridge height and merged droplet size variation in time for water-copper pair with $\alpha = 72°$. Decreasing trends represent the droplet size, while increasing lines are for the bridge height.

Notice that the red curves are for the case of negative gravity, blue curves for the zero-gravity case and black/gray curves represent the positive gravity simulations. The results presented in Fig. 4.10 also confirm that the effect of gravity larger droplets is non-negligible, therefore, has to be taken into account in the governing equation.

4.1.1 Validation with the Literature

Even though the evolution of single droplet and two identical droplet results presented in Section 4.1 strongly indicate that the methodology is consistent in itself, these findings must also be compared verified with another study in the literature. The perfect candidate for this purpose is the study of Yarin et al. [21]. They also investigated lubrication equation in their theoretical model, however, they disregarded the denominator in relation 3.26 while this term is included for all the applications in this thesis study. Moreover, although they utilized the same boundary conditions, they applied a different method for the implication of the initial profile. Instead of generating a droplet profile by solving the Young-Laplace equation, they preferred to describe the initial profile via two tangent parabolas, one is convex and the other is concave. This preference drastically change the behavior of the droplet evolution. Thus, exclusive to the verification of this study, the initial profile is created by two tangent parabolas. The liquid properties employed in [21] was as follows:

Table 4.2: Properties of the liquid used in [21].

	R_o (μm)	ρ (kg/m^3)	μ (mPa· s)	σ (mN/m)
Diethylene Glycol	119	1118	38.5	43.16

Yarin et al. [21] preferred to use Diethylene Glycol (DEG) as working fluid, both in their theoretical calculations and in the experimental setup. They denoted R_o as the radius of the droplet, which corresponds to half length of the droplet for our case. Early times of coalescence results are compared in the Fig. 4.11:

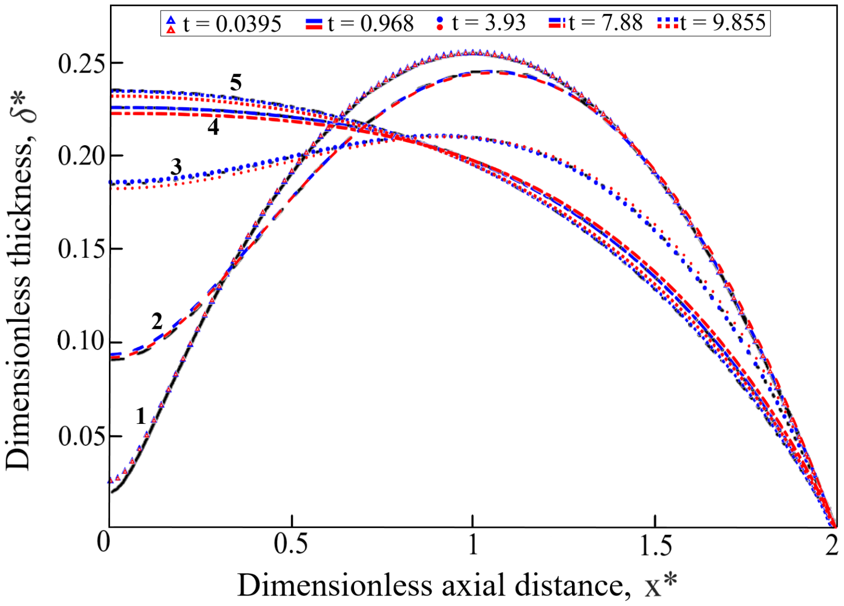

Figure 4.11: Comparison and validation of results, where black lines are presented by [21] at different dimensional times (given with ms).

In Fig. 4.11, results of Eq. (3.25) as well as the results of the version where the denominator term (earlier denoted as ζ in Eq. (3.26)) is neglected are analyzed for the validation. Notice, that droplet profiles shown with blue colored lines do not include the effect of this denominator term, whereas red colored droplet profiles include this effect. Yarin et al. did not share the data set for the figure in question, therefore, a comparison between results can only be made via observing the figure in a digitized manner. For the first two profiles, both our results for the bridge thicknesses deviate slightly from the results of Yarin et al., around 2 percent on the relative basis. Additionally, there is almost no deviation at the bridge thickness observed when comparing the results without the denominator effect against the results of Yarin et al. On the other hand, the results where the denominator effect is included still has a relative error around 1 percent. All in all, both our numerical results for the early time coalescence are in fairly good alignment with the reference results.

4.2 Effect of Bond Number and Contact Angle in the Simulations

As it was deduced with the non-dimensional analysis conducted in Section 3.4.4, our governing equations are only functions of the Bo and the contact angle. Effect of the Bo and contact angle on the formation and the coalescence of droplets will be presented and compared with over of 35 simulations; having 5 different contact angles and 6 to 8 different Bond numbers. As before, paramount attention is required in all these simulations that a tiny bridge is again employed manually between droplets to avoid the singularly fast movement. In the Fig. 4.12 the effect of the Bond number on droplets making different contact angles with the surface is shown.

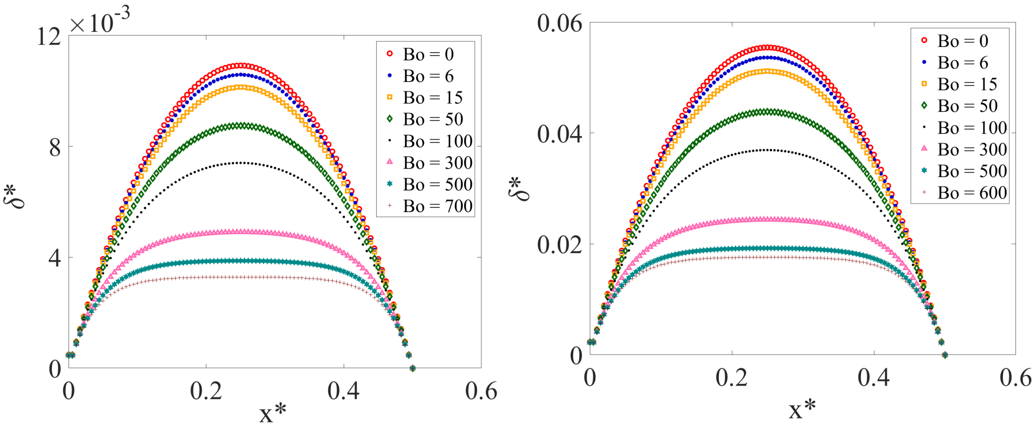

(a)

(b)

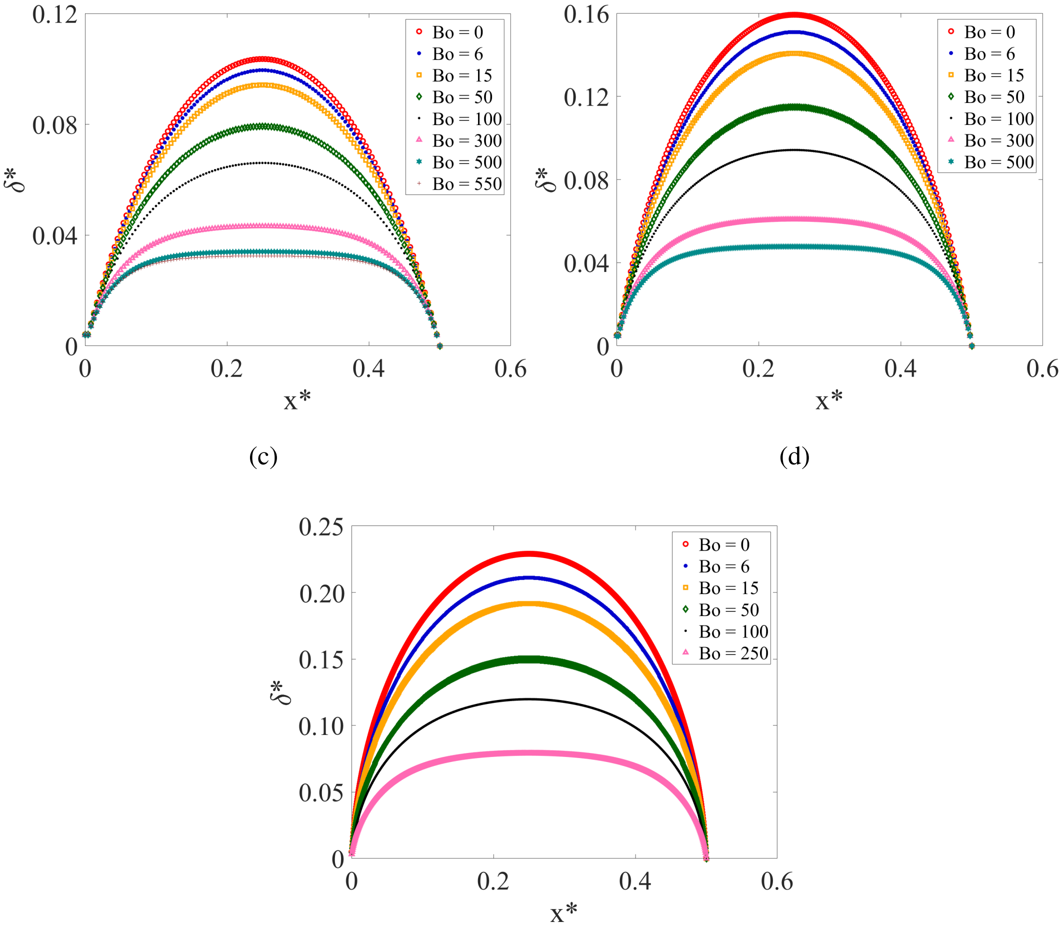

(c)

(d)

(e)

Figure 4.12: Effect of the Bond number on droplets formed with different contact angles. Initial droplet profiles for (a) $\alpha = 5°$, (b) $\alpha = 25°$, (c) $\alpha = 45°$, (d) $\alpha = 65°$, (e) $\alpha = 85°$

Increase in Bond number results with the domination of gravitational forces over the surface tension forces. It is evident from the results shown in Fig. 4.12 that the Bond number has a direct impact on the droplet shape; as it increases, shape of the drops become more flattened from the top. Nevertheless, there is a limitation regarding the maximum Bond number that can be attained by a sample drop. Beyond this point, larger droplets cannot be created; instead droplet starts collapsing towards inside at the bridge section, splitting into smaller droplets. This maximum Bond number is dissimilar for drops with unique contact angles; the higher contact angle of the drop, the less the maximum Bond number that a droplet can withstand. While the lower limit is simply zero, maximum limit of the Bond number for distinct contact angles are given in the Table 4.3.

Table 4.3: Maximum Bond Number Values for Different Contact Angles

Contact Angle	$\alpha = 5°$	$\alpha = 25°$	$\alpha = 45°$	$\alpha = 65°$	$\alpha = 85°$
Max. Bond Number	∼700	∼600	∼550	∼500	∼250

Notice that maximum Bond numbers given in the Table 4.3 are approximate. Since the problem requires a well balance between the space interval dx and the time interval dt as well as it includes several convergence criteria, determining the exact Bond number value for a specific setting is rather toilsome. However, finding a better result is only practiced with a droplet having a contact angle of $65°$. Maximum Bond number for this setting is observed around $Bo = 537$. Further Bond numbers can be achieved by reducing the convergence criterion of RK4 method applied to Eq. (3.18), yet it severely compromises the accuracy of results. Moreover, although it is possible to increase the Bond number by reducing the convergence criterion (and consequently reducing the accuracy), the contact angle of the composed droplet diverges from the value that is defined at the first place. Therefore, it should be pointed out that Bond number limitation is reached as the contact angle of the created droplet deviates from the one that is provided as the boundary condition.

In order to be able to generate a proper droplet and run a smooth simulation, one must increase the total number of nodes in the solution domain, *i.e.* decrease the spatial interval dx. However, doing so not only immensely increases the computational cost, but also it tightens the interval to achieve the delicate balance between the space interval dx and the time interval dt. For the contact angles $\alpha = 5° - 65°$, droplets can be created with a fair number of nodes, *e.g.* $100 - 200$. However, at the close proximity to $85°$ contact angle, the spatial resolution needs to be increased to be able to create the droplet profile at the boundaries. Due to these limitations, $85°$ setting is applied to a larger number of nodes, 1000 to be exact. Yet, even employing this much nodes can have devastating effect on the computational time. While other settings lasts on the order of half an hour, $85°$ contact angle case with 1000 nodes takes up to couple days. After successfully attaining their initial shapes, droplets are ready for coalescence. Merging process for $25°$, $45°$, $65°$ and $85°$ contact angles are presented in Figs. 4.13 to 4.17. It should also be noted that only a number of time steps of coalescence simulations are depicted in Figs. 4.13 to 4.17 to increase the readability of results.

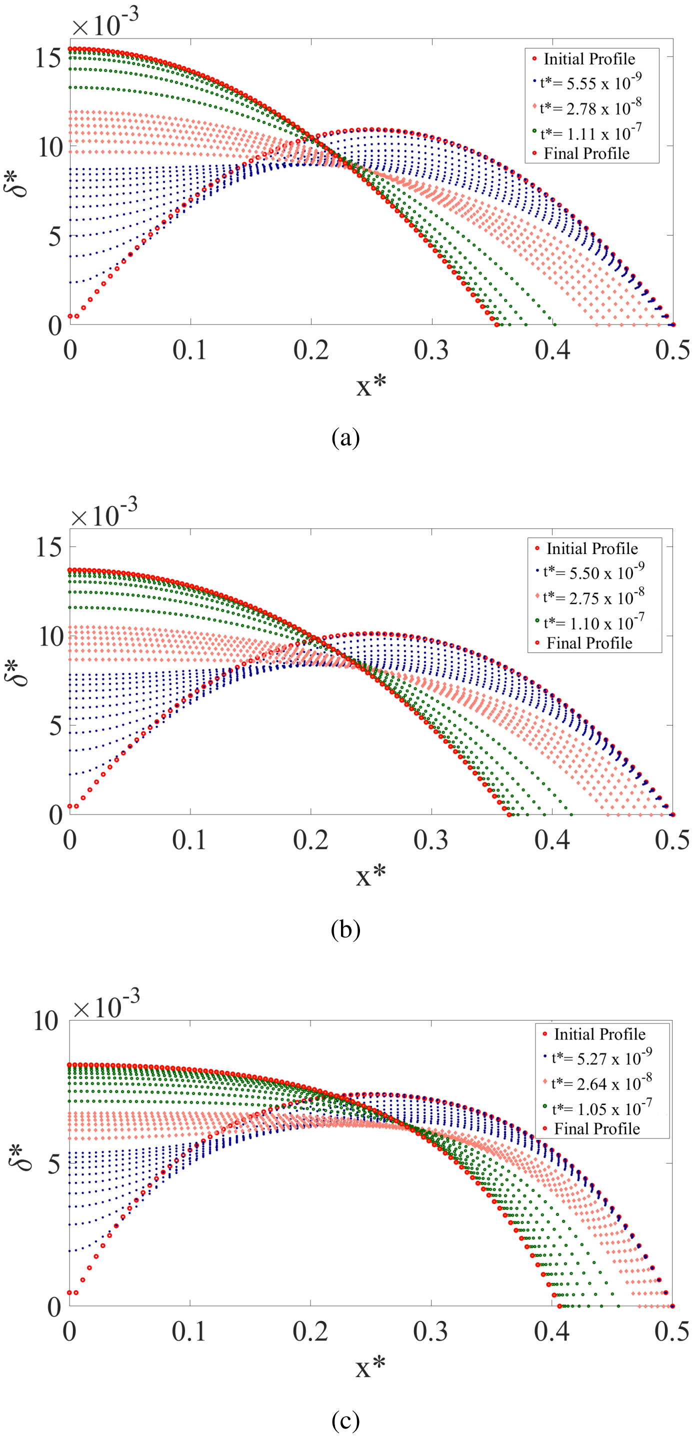

(a)

(b)

(c)

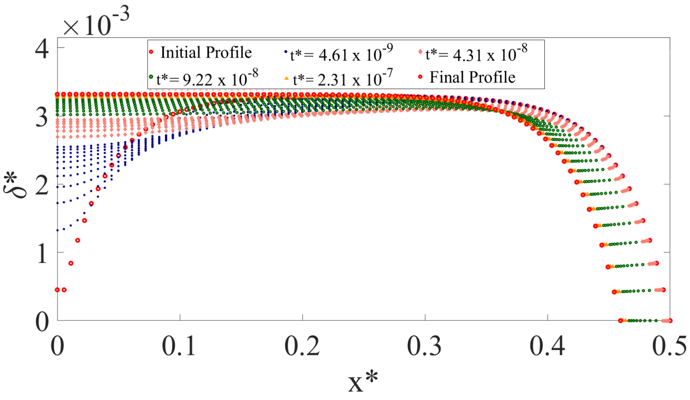

(d)

Figure 4.13: Coalescence results for $5°$ contact angle case. Simulations with (a) Bo $= 0$, (b) Bo $= 15$, (c) Bo $= 100$, (d) Bo $= 700$

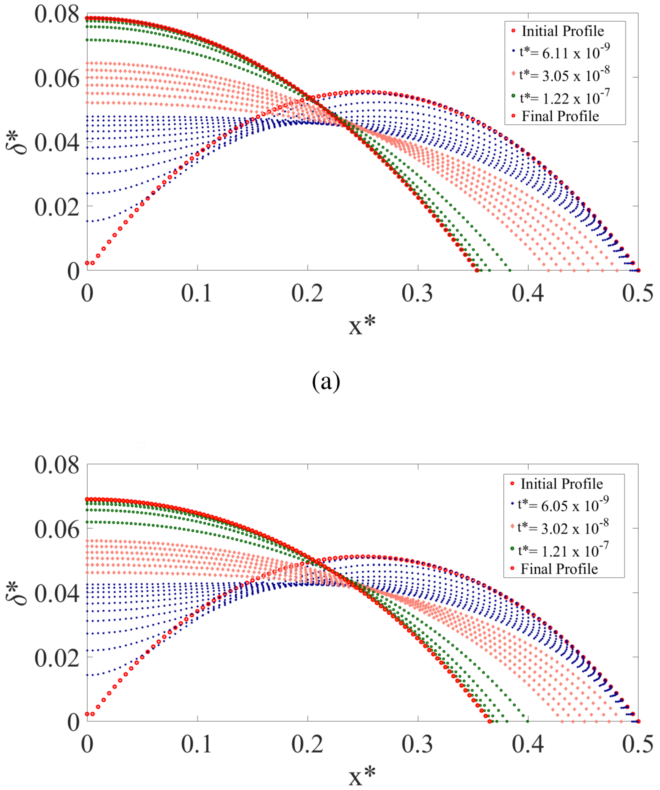

(a)

(b)

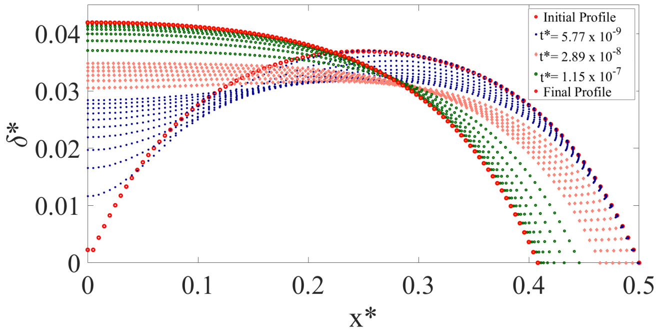

(c)

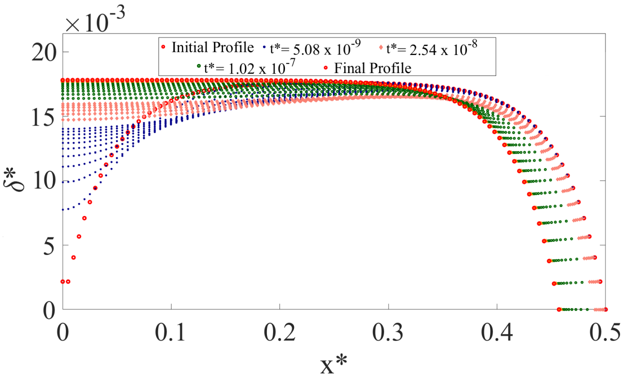

(d)

Figure 4.14: Coalescence results for $25°$ contact angle case. Simulations with (a) Bo $= 0$, (b) Bo $= 15$, (c) Bo $= 100$, (d) Bo $= 600$

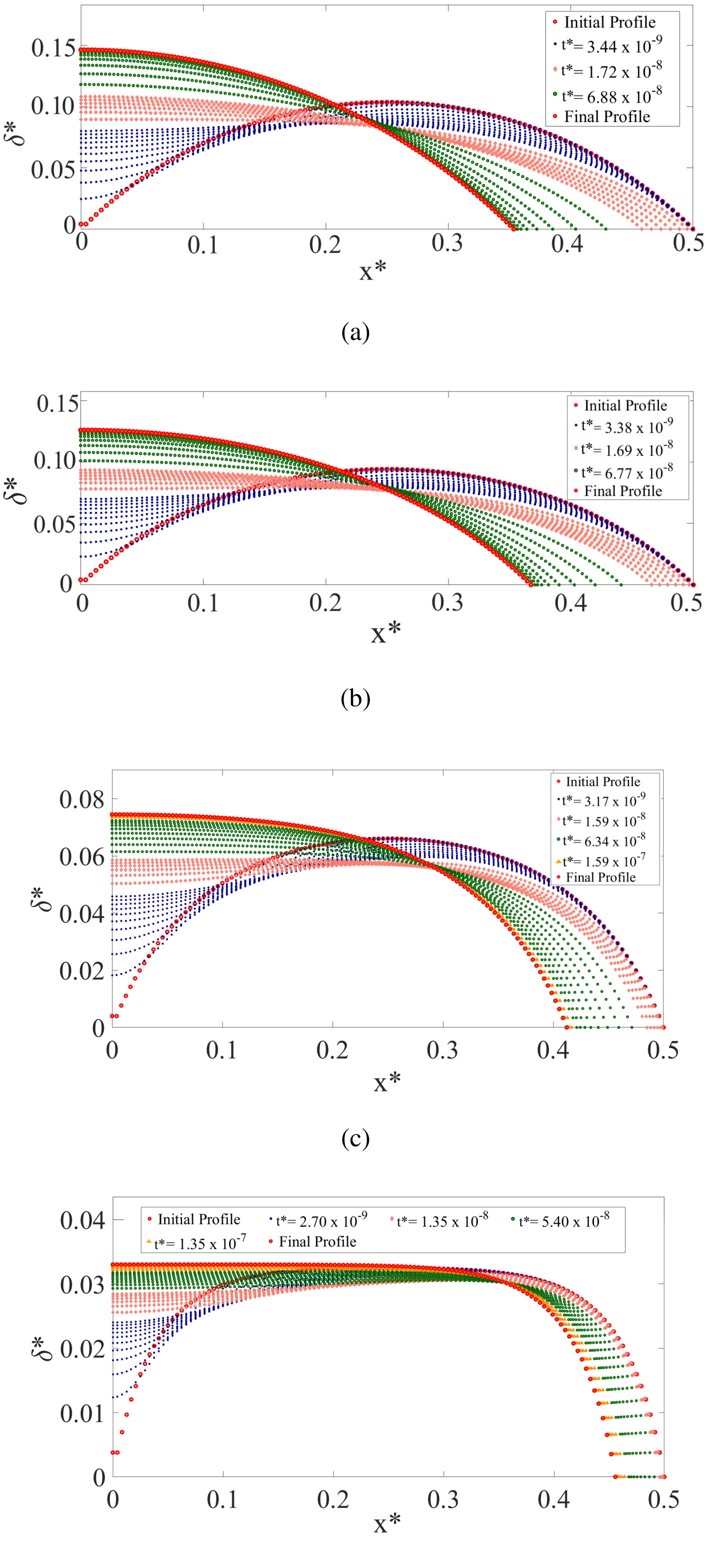

(a)

(b)

(c)

(d)

Figure 4.15: Coalescence results for $45°$ contact angle case. Simulations with (a) Bo $= 0$, (b) Bo $= 15$, (c) Bo $= 100$, (d) Bo $= 550$

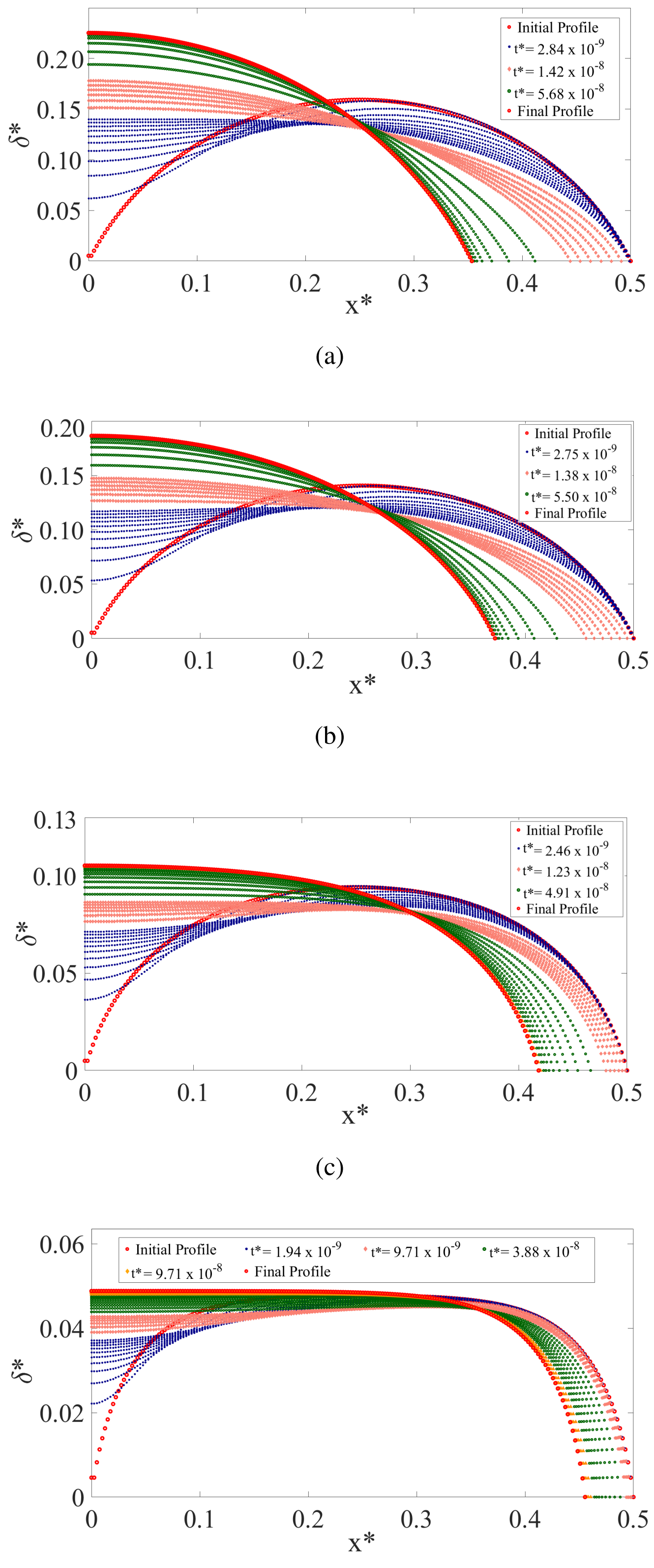

(a)

(b)

(c)

(d)

Figure 4.16: Coalescence results for 65° contact angle case. Simulations with (a) Bo $= 0$, (b) Bo $= 15$, (c) Bo $= 100$, (d) Bo $= 500$

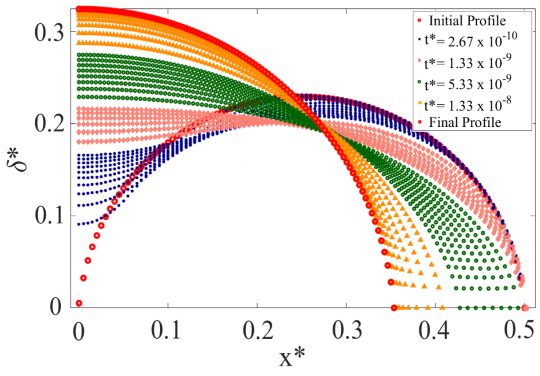

(a)

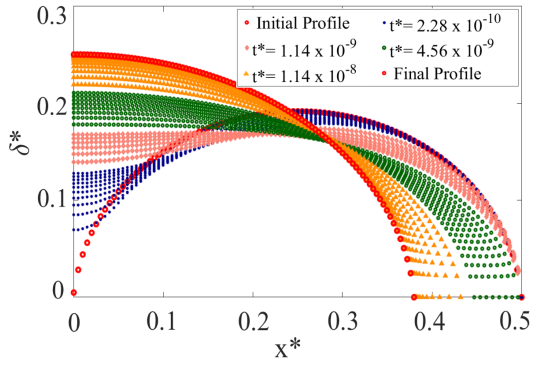

(b)

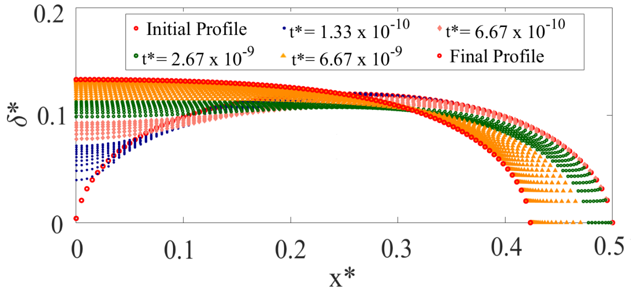

(c)

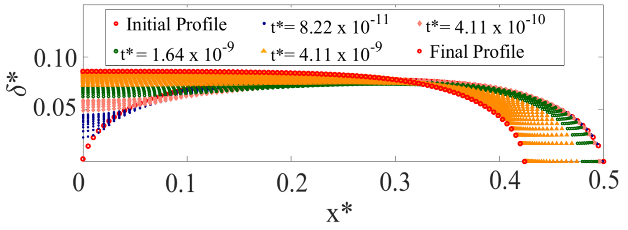

(d)

Figure 4.17: Coalescence results for 85° contact angle case. Simulations with (a) Bo $= 0$, (b) Bo $= 15$, (c) Bo $= 100$, (d) Bo $= 250$

Notice that some of the simulation results could not be presented with the same scale on both axes, as it would make it impossible to read the figures. Instead, its y-axis is given with more resolution. Moreover, as expected, in all the coalescence results increase in the Bond number plays a dominant role on both the evolution of the bridge height and the length of the droplets. When Bond number is increased, final bridge height of the coalesced droplet is reduced. If the Bond number is low, then the final length of the coalesced droplet is smaller.

As result of the coalescence simulations, number of dimensionless parameters are investigated. First of which is the time evolution of the bridge height between droplets. For distinct Bond numbers, non-dimensional bridge height versus non-dimensional time is plotted and they are shown in Fig. 4.18:

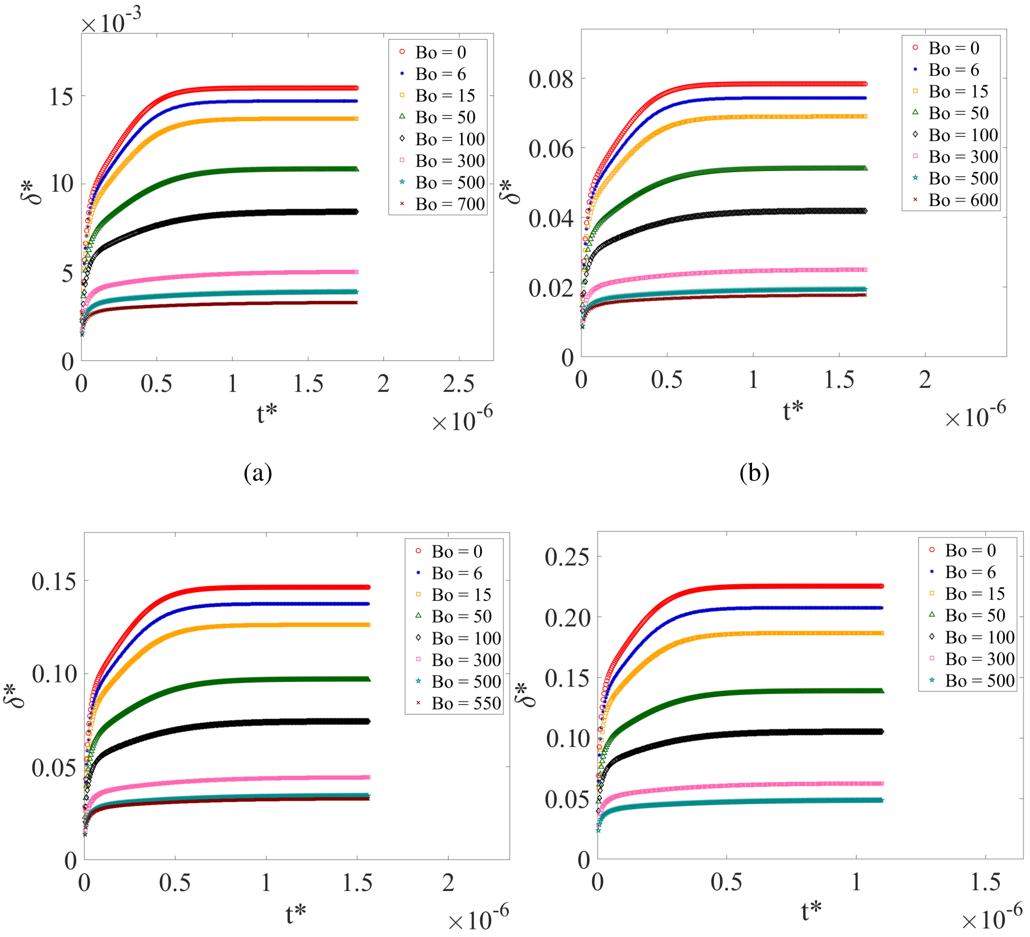

(a)

(b)

(c)

(d)

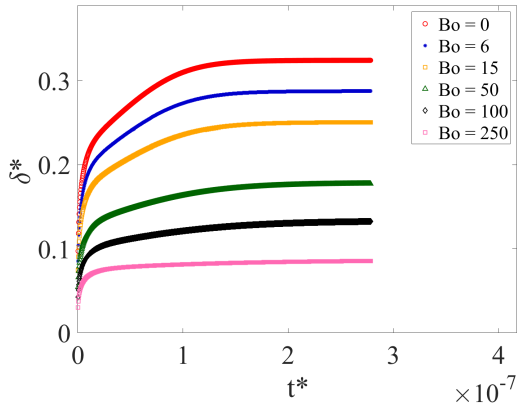

(e)

Figure 4.18: Non-dimensional analysis on the effect of Bond number to the bridge heights of droplets having different contact angles (a) $\alpha = 5°$, (b) $\alpha = 25°$, (c) $\alpha = 45°$, (d) $\alpha = 65°$, (e) $\alpha = 85°$

When the bridge height difference between two consecutive time steps is sufficiently small, steady state conditions within the coalescence process are attained. It is observed from Fig. 4.18 the non-dimensional time for reaching the steady state is indifferent for various settings as it was also indicated with our non-dimensional analysis in Section 3.4.4. Analogous to the bridge height analysis, non-dimensional length with respect to non-dimensional time is investigated, and results are shared in Fig. 4.19:

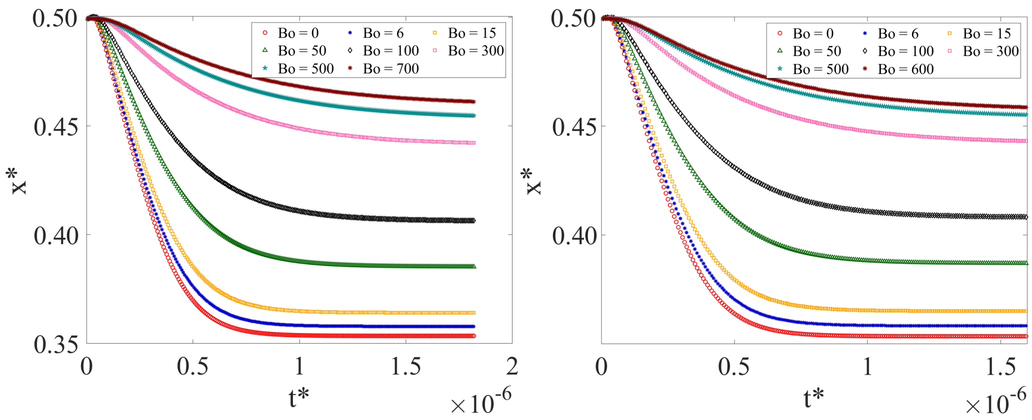

(a) (b)

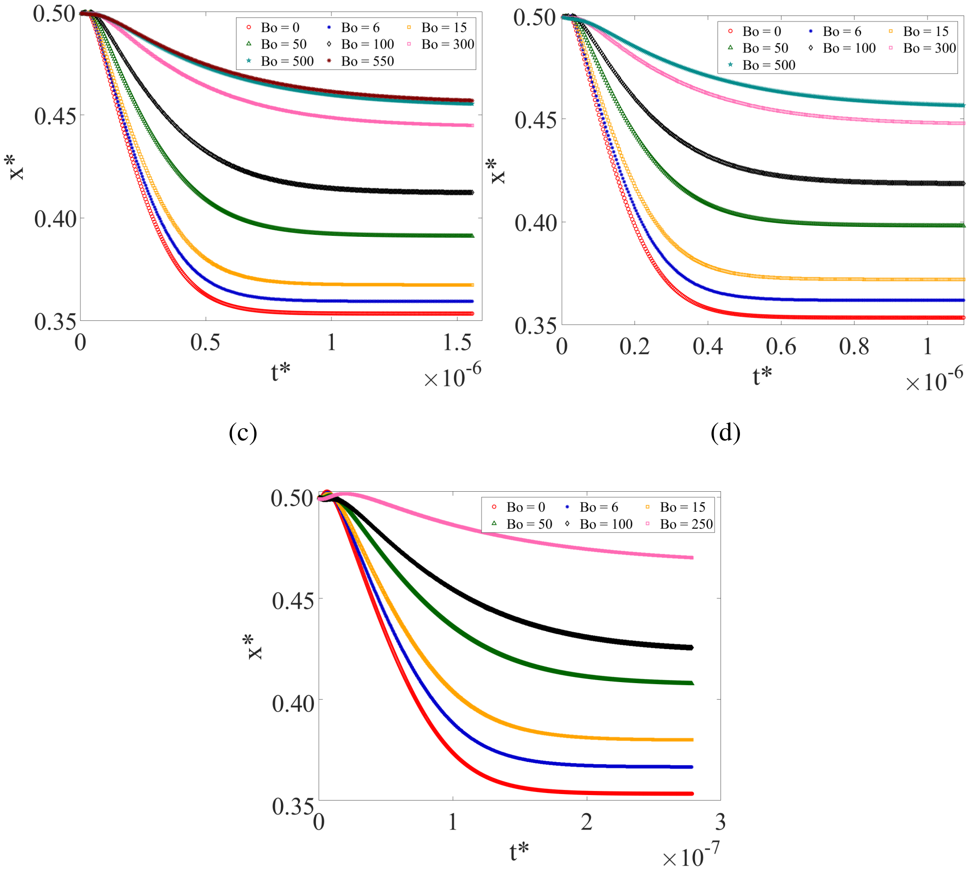

(c)

(d)

(e)

Figure 4.19: Non-dimensional analysis on the effect of Bond number to the lengths of droplets having different contact angles (a) $\alpha = 5°$, (b) $\alpha = 25°$, (c) $\alpha = 45°$, (d) $\alpha = 65°$, (e) $\alpha = 85°$

It is deduced from these results that greater the contact angle is, the higher the bridge height at steady state. However, increasing the Bond number again affects the maximum height achieved since gravitational forces somewhat compress the coalesced droplet. Droplets can still be created and merged with Bond numbers beyond the approximate limits given with Table 4.3, yet the outcome would be most likely misleading and the results may be easily misinterpreted since numerical accuracy is drastically decreased and a substantial error is attained regarding the contact angle. As the merged droplet reaches to its steady state, radius of curvature and the second derivative values are checked at every node of the profile in Figs. 4.20 and 4.21 in order to see the effect of Bond number and contact angle to these parameters:

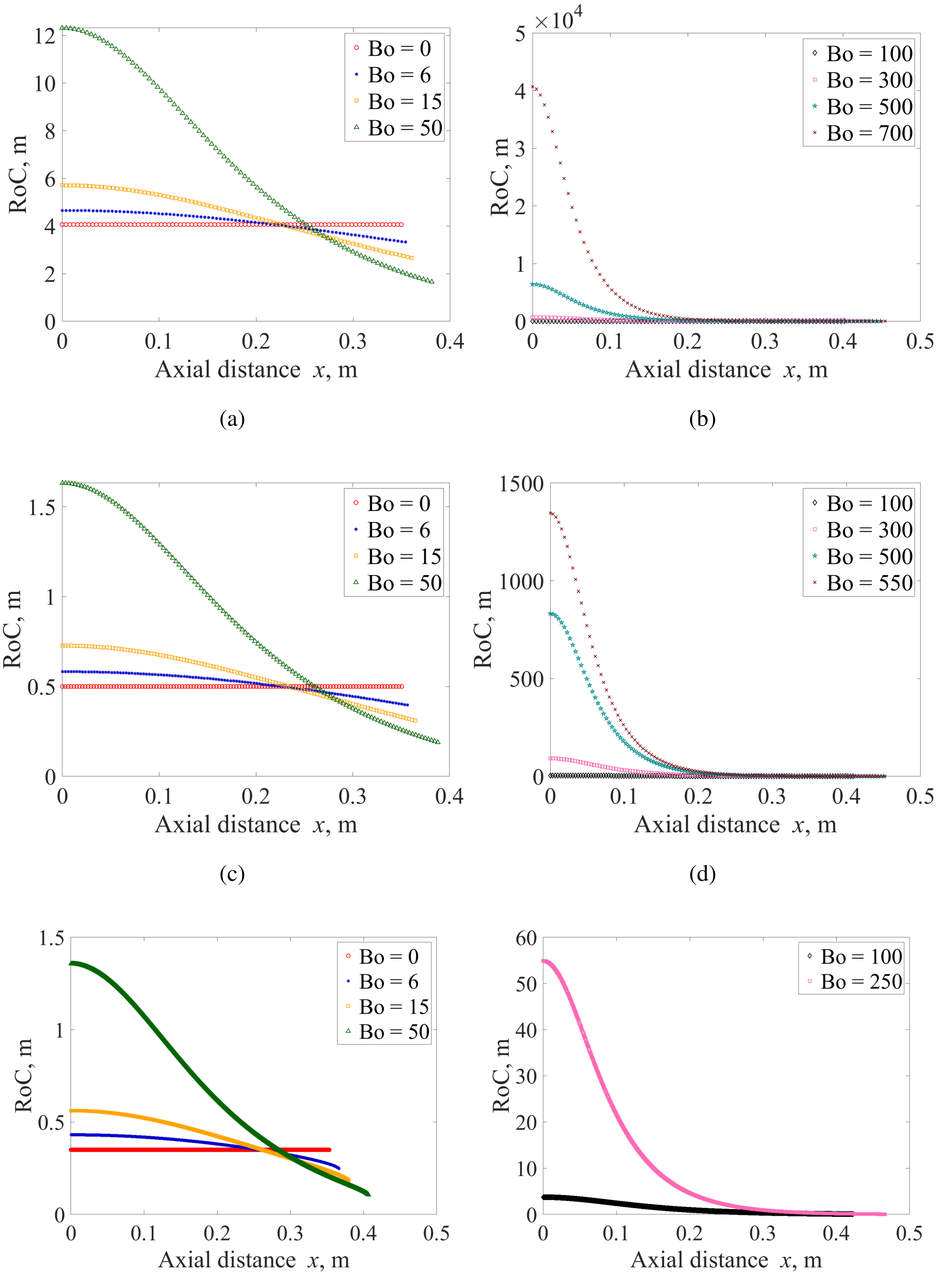

(a) (b)

(c) (d)

(e) (f)

Figure 4.20: Non-dimensional analysis on the effect of Bond number to the radius of curvature values of droplets having different contact angles (a) First set of results for $\alpha = 5°$, (b) Second set of results for $\alpha = 5°$, (c) First set of results for $\alpha = 45°$, (d) Second set of results for $\alpha = 45°$, (e) First set of results for $\alpha = 85°$, (f) Second set of results for $\alpha = 85°$

Radius of the curvature is an important indicator in terms of verifying the integrity of the method employed. Once the coalescence dynamics are settled and merged droplet attained its steady state, the radius of curvature needs to converge to a constant for the zero Bond number cases. As Bond number increases, the obliquity in the radius of curvature also increases. Since the trend in radius of curvature results follow similar trend, results in Fig. 4.20 are only given for 5°, 45° and 85° contact angles.

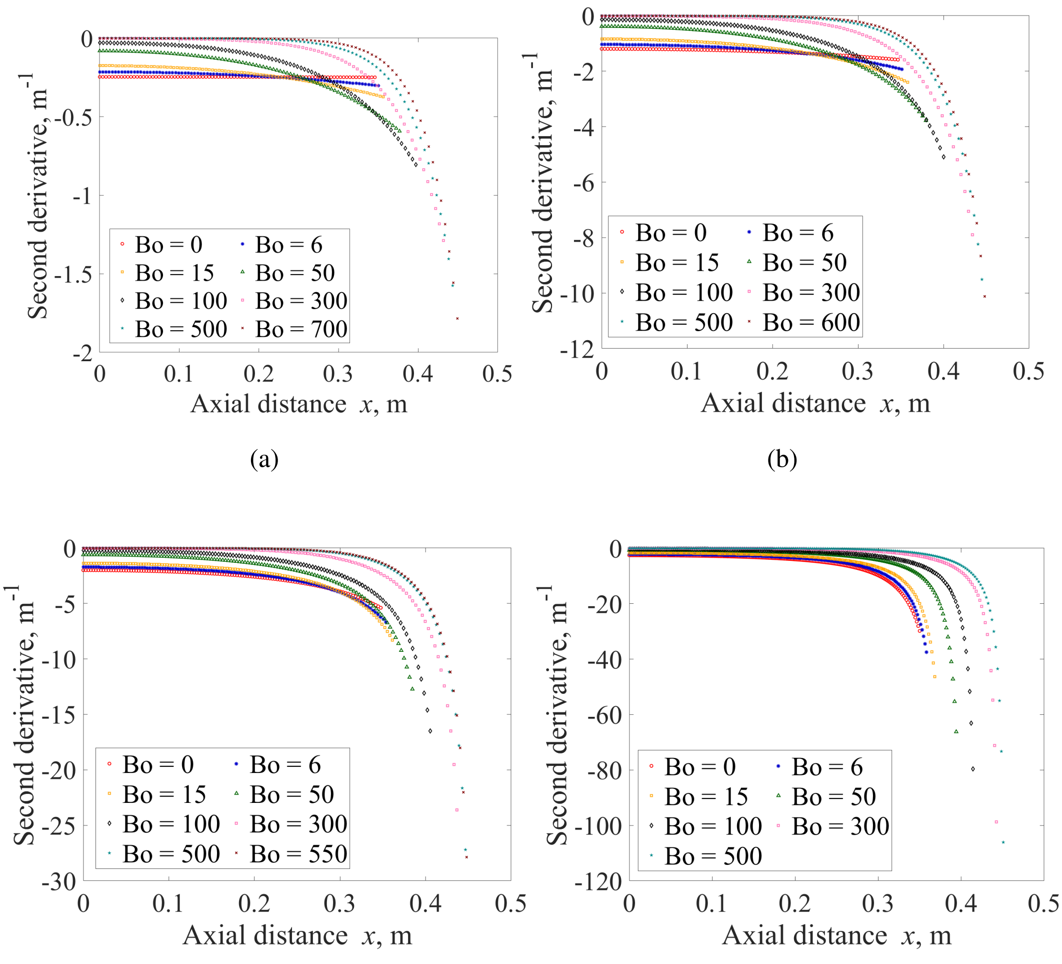

(a)

(b)

(c)

(d)

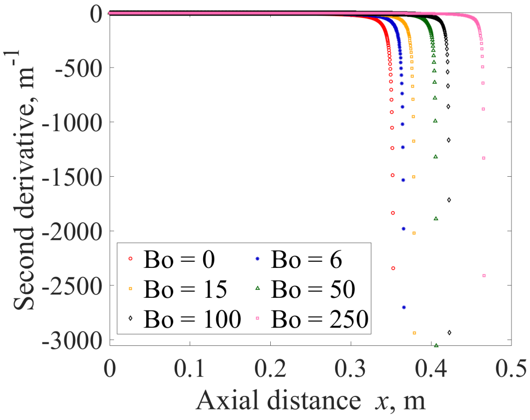

(e)

Figure 4.21: Non-dimensional analysis on the effect of Bond number to the second derivative values of droplets having different contact angles (a) $\alpha = 5°$, (b) $\alpha = 25°$, (c) $\alpha = 45°$, (d) $\alpha = 65°$, (e) $\alpha = 85°$

In Fig. 4.21, the second derivative values of each node at the steady state are plotted. It is easily observed that as the contact angle grows, the second derivative values exponentially increase at the steady state. In a similar manner, the formation of two identical droplets are also achieved for various Bond numbers and unique contact angles. Their respective initial profiles are given in the Fig. 4.22:

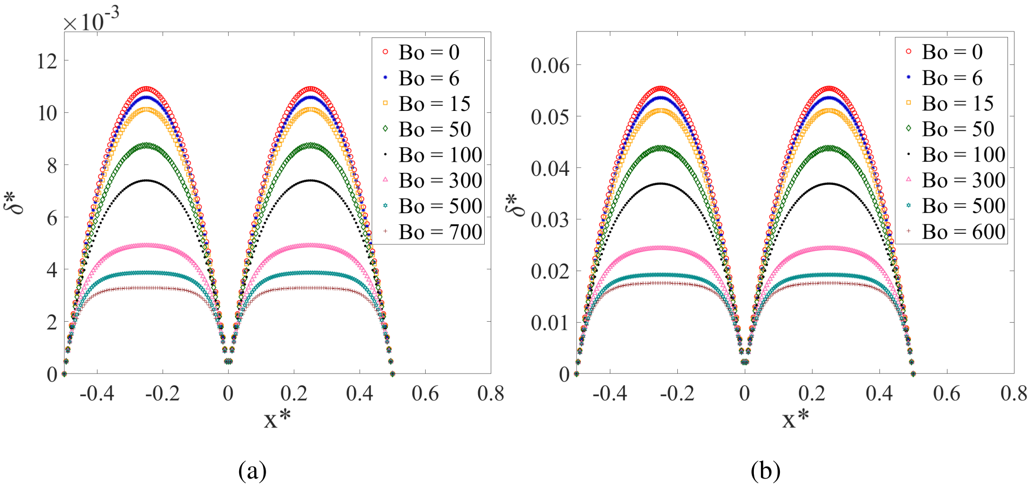

(a) (b)

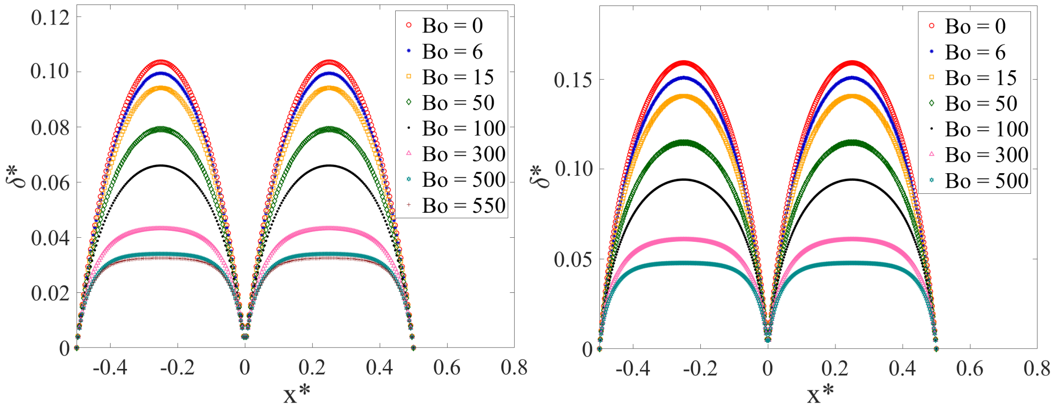

(c) (d)

Figure 4.22: Effect of the Bond number on identical droplets formed with different contact angles. Initial droplet profiles with contact angles (a) $\alpha = 5°$, (b) $\alpha = 25°$, (c) $\alpha = 45°$, (d) $\alpha = 65°$

Once the initial profiles are created, the coalescence simulations are completed for $25°$, $45°$ and $65°$ contact angles. They are presented in Figs. 4.23 to 4.26.

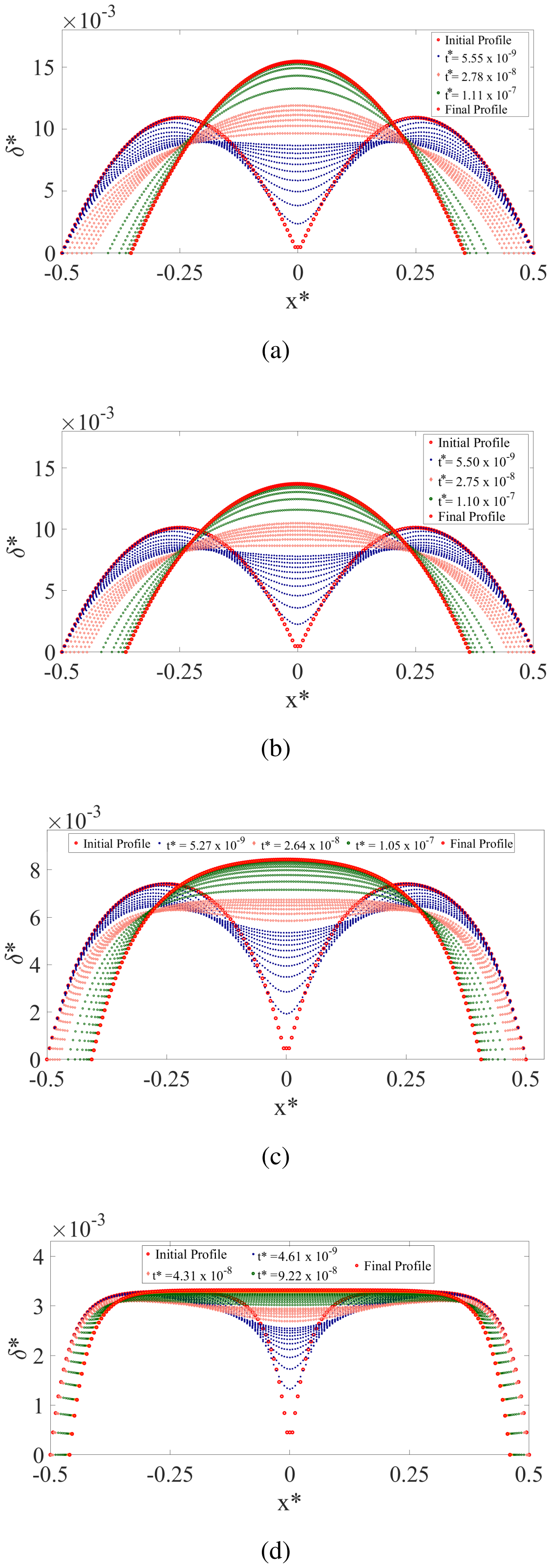

Figure 4.23: Coalescence results for $5°$ contact angle case. Simulations with (a) Bo $= 0$, (b) Bo $= 15$, (c) Bo $= 100$, (d) Bo $= 700$

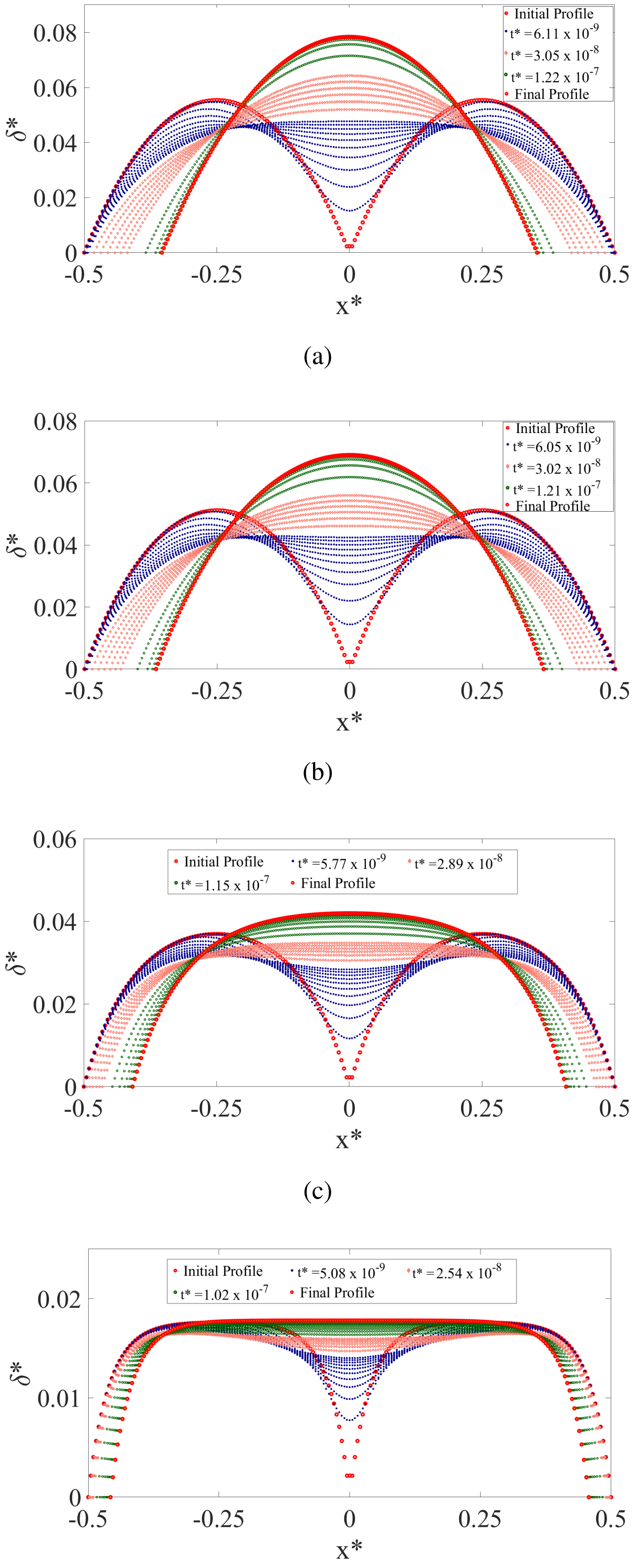

(a)

(b)

(c)

(d)

Figure 4.24: Coalescence results for 25° contact angle case. Simulations with (a) Bo $= 0$, (b) Bo $= 15$, (c) Bo $= 100$, (d) Bo $= 600$

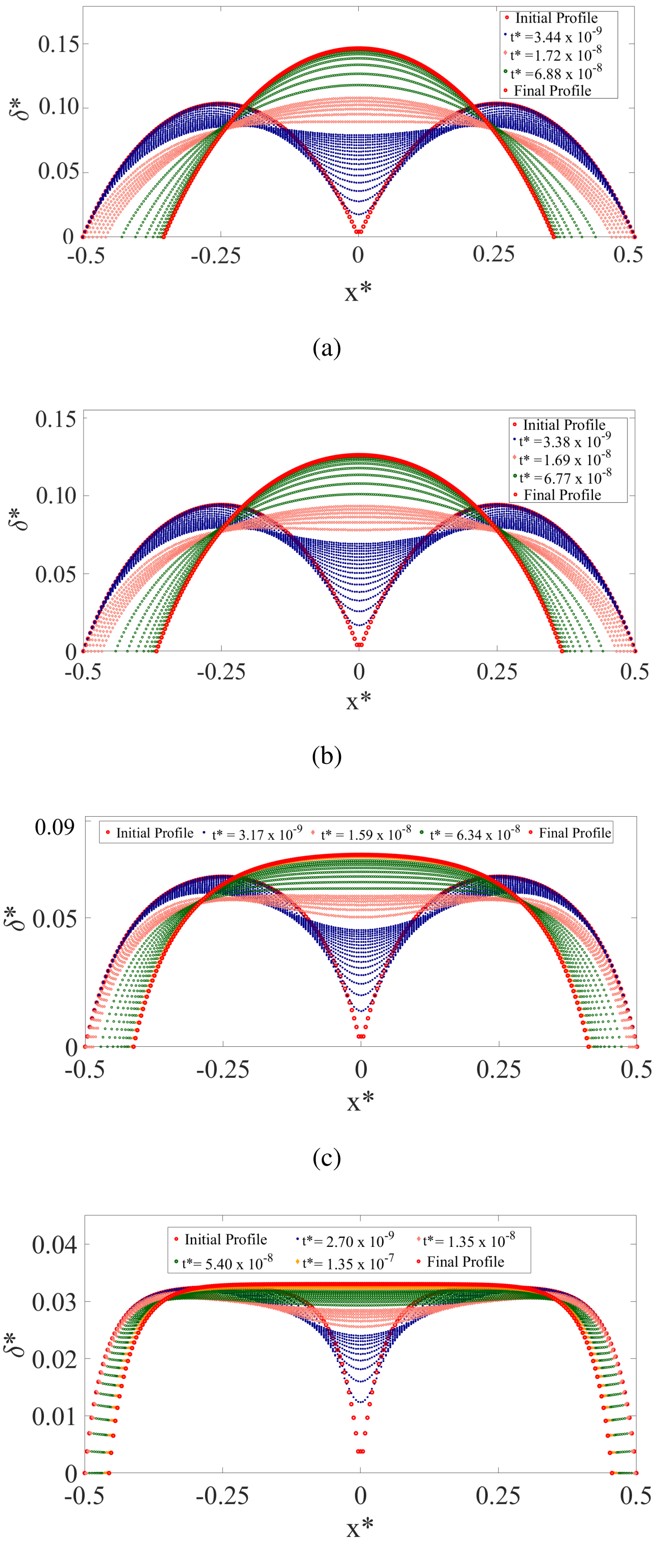

Figure 4.25: Coalescence results for 45° contact angle case. Simulations with (a) Bo $= 0$, (b) Bo $= 15$, (c) Bo $= 100$, (d) Bo $= 550$

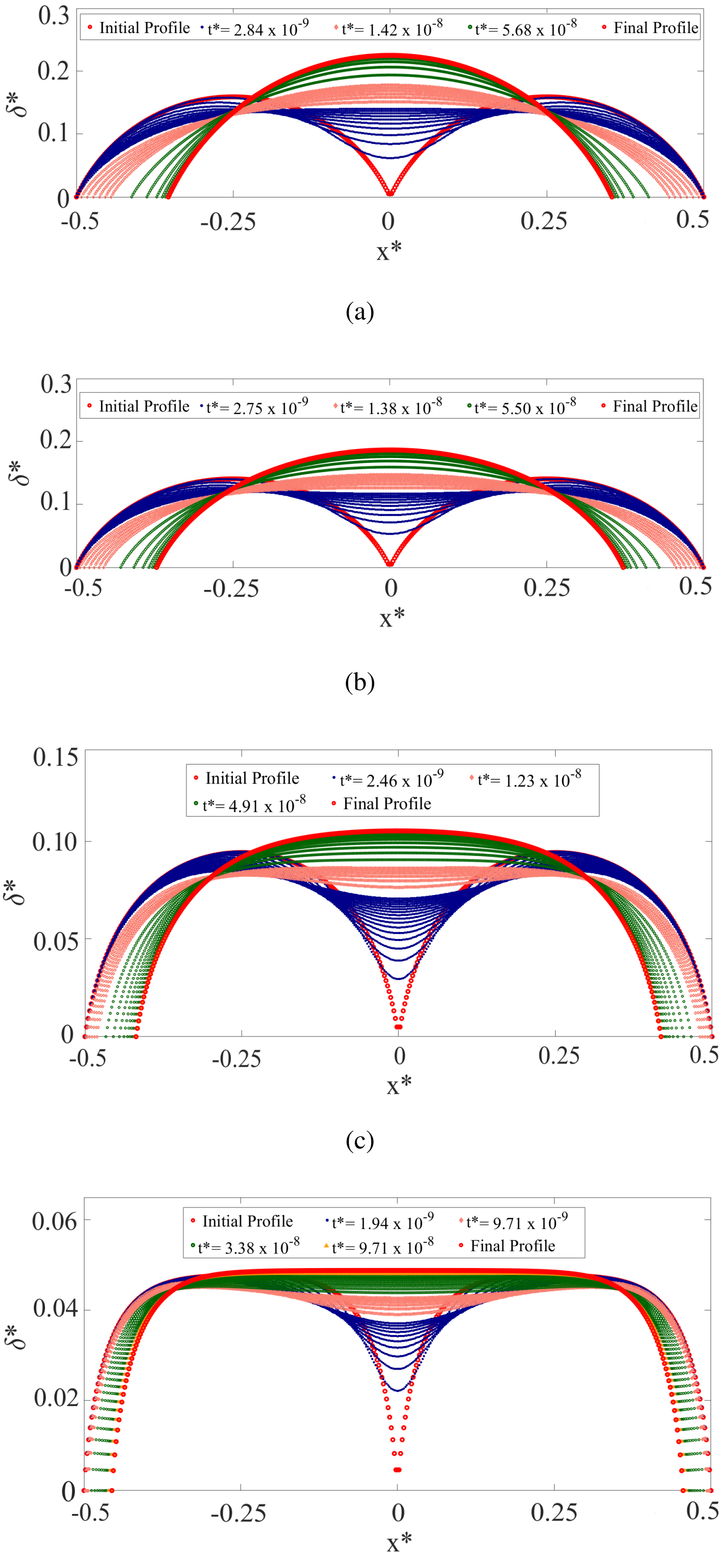

(a)

(b)

(c)

(d)

Figure 4.26: Coalescence results for 65° contact angle case. Simulations with (a) Bo = 0, (b) Bo = 15, (c) Bo = 100, (d) Bo = 500

Notice that the coalescence results for 5° and 25° contact angle simulations as well as merging result of 45° simulation with 550 Bond number and the merging result of 65° simulation with 500 Bond number are not represented with same scales on both axes. It can easily be observed that the coalescence results of single symmetrical droplet given with Figs. 4.13 to 4.16 and two identical droplets presented with Figs. 4.23 to 4.26 are exactly the same. Thus, numerical equations, codes and their implementation are consistent in itself.

Similar to the previous results, two important parameters, bridge height and length of the coalescing droplet through time are investigated and presented in Fig. 4.27:

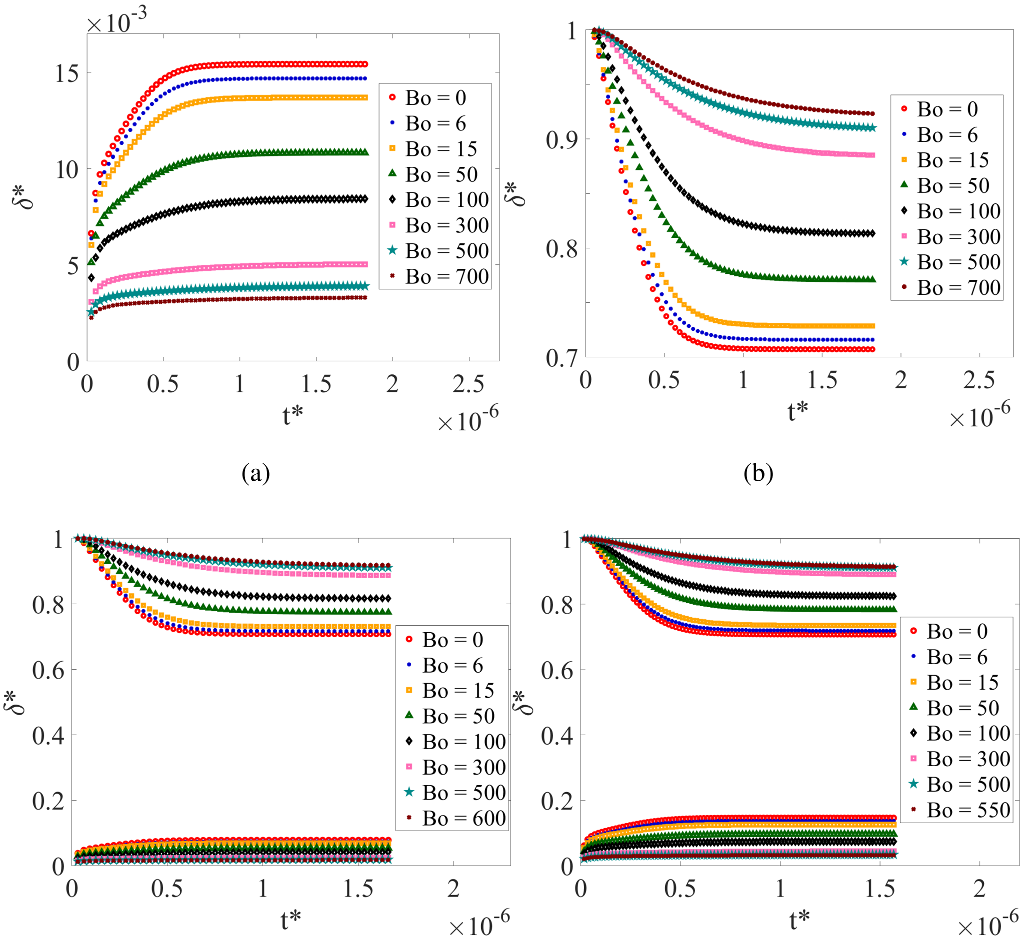

(a) (b)

(c) (d)

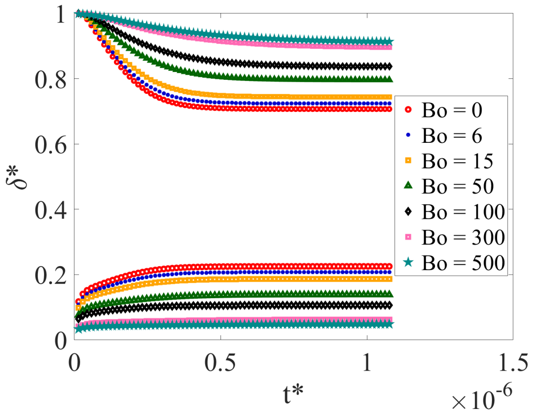

(e)

Figure 4.27: Effect of the Bond number on identical droplets formed with different contact angles. Top five lines are for the lengths that are decreasing, while bottom five lines are for bridge heights which are increasing. The plots are given for, (a) Bridge height with $\alpha = 5°$, (b) length with $\alpha = 5°$, (c) $\alpha = 25°$, (d) $\alpha = 45°$, (e) $\alpha = 65°$

It should be pointed out that for the $\alpha = 5°$ setting, the bridge height and length data could not be presented in the same figure since there was a large scaling difference between these two data, which eventually lead to an incoherent figure. For the other contact angle values, fitting these data into a single figure is readable. It is easily discerned that the time to reach steady state is equal for both length and bridge height parameters. Radius of curvature and and second derivative values at each spatial node is again analyzed, and presented below.

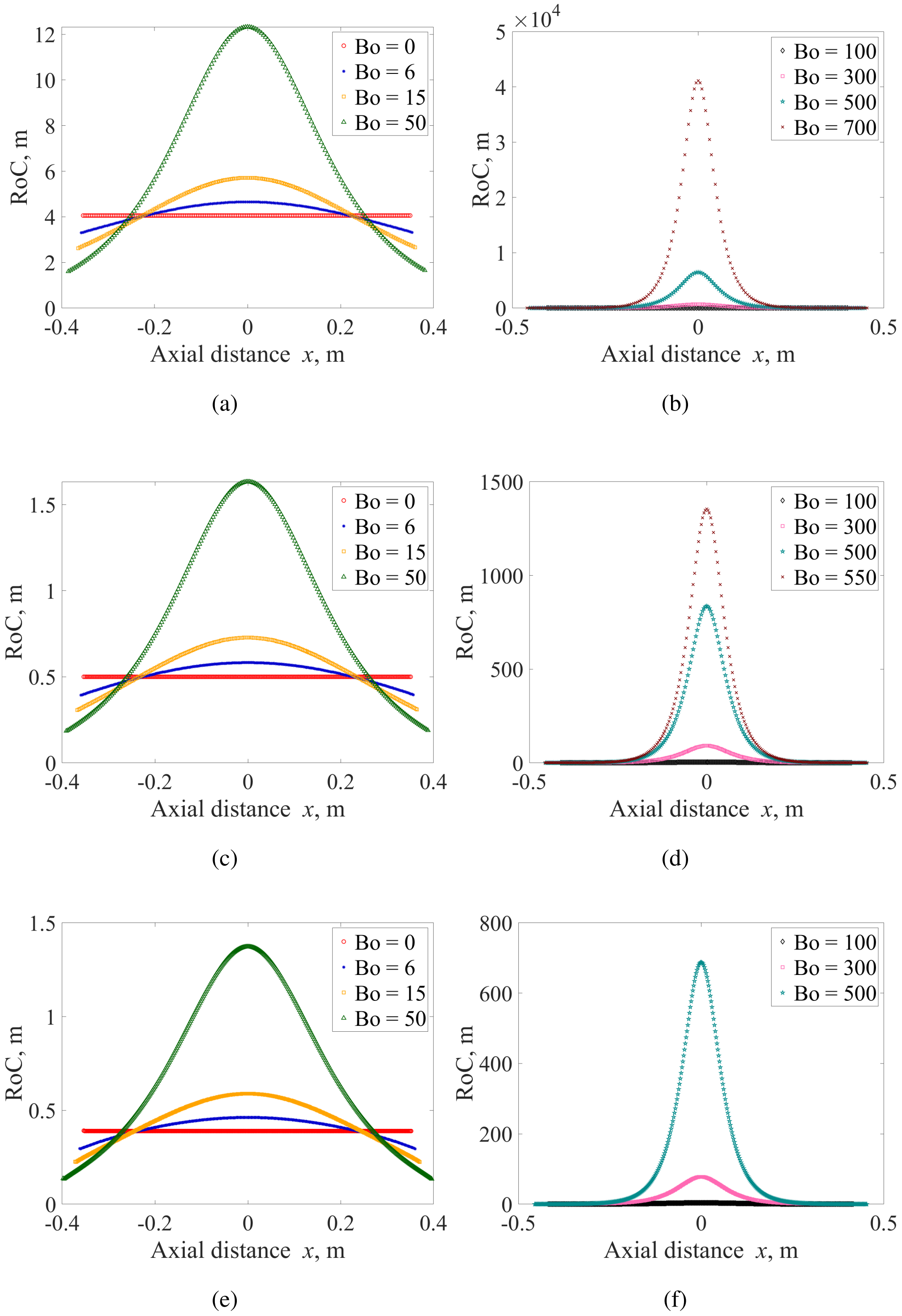

(a) (b)

(c) (d)

(e) (f)

Figure 4.28: Non-dimensional analysis on the effect of Bond number to the radius of curvature values of droplets having different contact angles (a) First set of results for $\alpha = 5°$, (b) Second set of results for $\alpha = 5°$, (c) First set of results for $\alpha = 45°$, (d) Second set of results for $\alpha = 45°$, (e) First set of results for $\alpha = 65°$, (f) Second set of results for $\alpha = 65°$

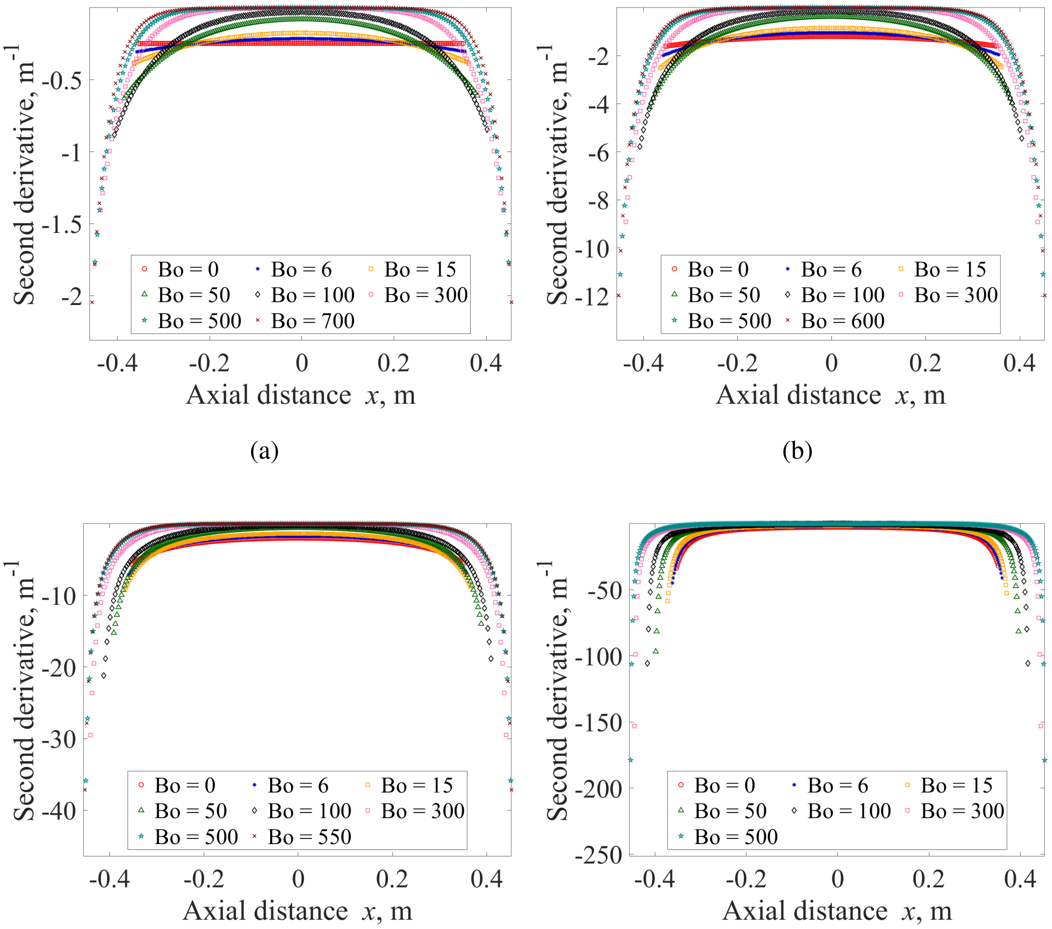

(a) (b)

(c) (d)

Figure 4.29: Non-dimensional analysis on the effect of Bond number to the second derivative values of droplets having different contact angles (a) $\alpha = 5°$, (b) $\alpha = 25°$, (c) $\alpha = 45°$, (d) $\alpha = 65°$

Merging of two identical droplets with 85° contact angle is avoided. The merging simulations for single symmetrical droplet of 85° contact angle takes up to couple days to complete since at least 1000 nodes are required in the solution domain to create a proper profile. For the merging simulations of two identical droplets, total mesh number doubles up to 2000 nodes. With Intel Core i9-9900K CPU, the solution of only one time step of this setting approximately takes 10 seconds, therefore, it is estimated that the whole simulation inevitably takes around 10 days. Thus, it is not feasible to analyse the coalescence of two identical droplets with 85° contact angle.

Table 4.4: Non-dimensional bridge height values at the steady state.

Contact Angle	**Bond Number**	**Single Symmetrical Droplet δ^***	**Two Identical Droplets δ^***
5°	0	0.015436	0.015439
	6	0.014695	0.014697
	15	0.013697	0.013699
	50	0.010824	0.010825
	100	0.008436	0.008436
	300	0.005045	0.005045
	500	0.003919	0.003919
	700	0.003318	0.003319
25°	0	0.078379	0.078379
	6	0.074341	0.074341
	15	0.068992	0.068992
	50	0.054028	0.054028
	100	0.041945	0.041945
	300	0.025060	0.025060
	500	0.019476	0.019476
	600	0.017801	0.017801
45°	0	0.146448	0.146466
	6	0.137547	0.137563
	15	0.126247	0.126252
	50	0.096784	0.096789
	100	0.074510	0.074513
	300	0.044444	0.044444
	500	0.034593	0.034593
	550	0.033016	0.033016
65°	0	0.225258	0.225271
	6	0.207464	0.207468
	15	0.186643	0.186648
	50	0.138378	0.138380
	100	0.105289	0.105290
	300	0.062634	0.062634
	500	0.048808	0.048808

Although the coalescence results for simulations of single symmetric droplet and two identical droplets align perfectly, bridge heights at the steady state are compared in the table given above. Aside from very slight differences due to numerical errors, results are in perfect match again. These findings are plotted in Fig. 4.30 to have a visual understanding towards the Bond number versus the contact angle dependency on the maximum thickness of the droplet at the steady state. It is observed that the effect of Bond number in $5°$ degrees contact angle is somewhat small compared to other contact angle cases. On the other hand, as the contact angle of the droplet increases, the effect of Bond number becomes more evident.

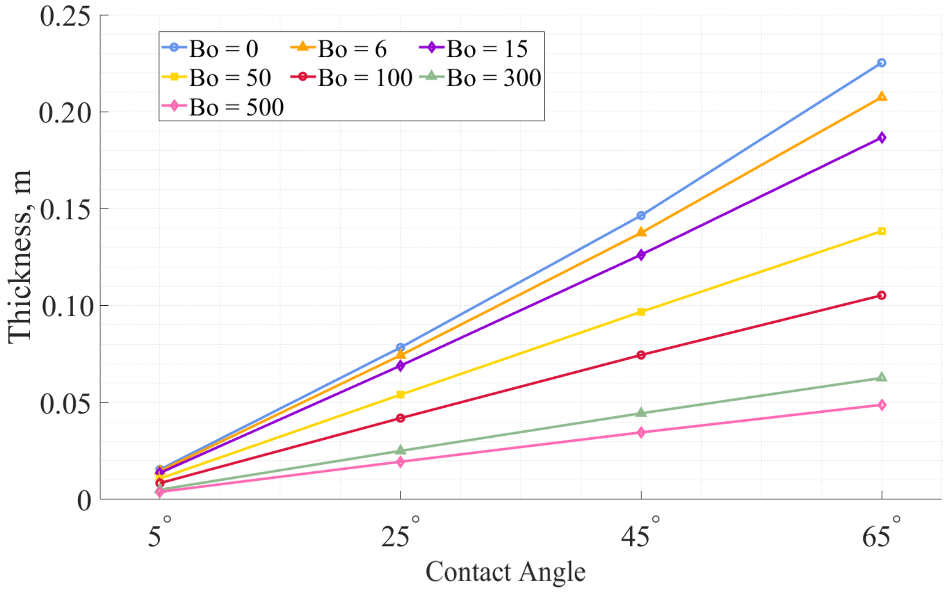

Figure 4.30: Maximum thickness values of droplets reached at the steady state is illustrated. Individual lines represent different Bond numbers, while different contact angles are given in the x-axis.

The last set of results regarding the droplet formation is gathered for different sized droplets. Since previous results provide sufficient insight and different sized droplets are again generated in a correlative way, limited number of modellings are executed for illustrative purposes. Here, different sized droplets are proportioned with their initial horizontal lengths. Since the simulations followed a similar pattern until now, only the modelling results having $25°$ and $65°$ contact angles subjected to different Bond numbers are investigated.

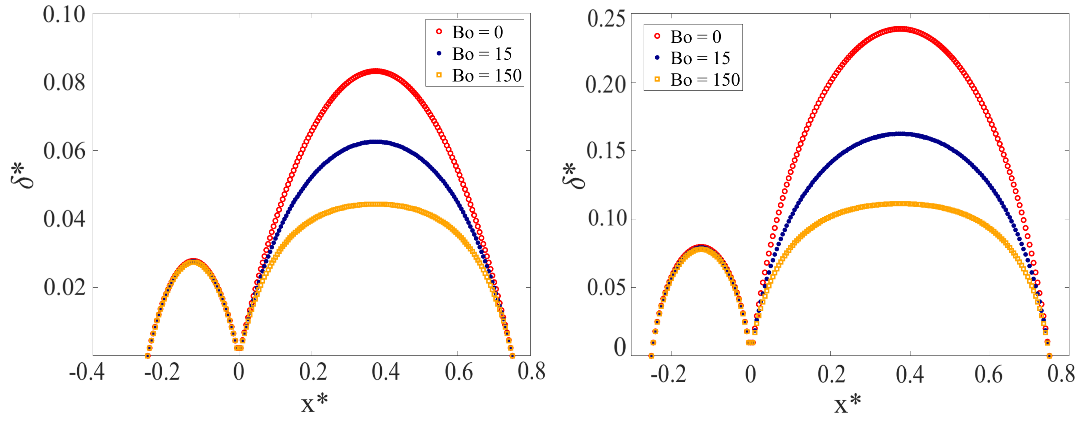

(a) (b)

Figure 4.31: Effect of the Bond number on droplets having $1:3$ initial length ratios. Initial droplet profiles for (a) contact angle $\alpha = 25^\circ$ and (b) contact angle $\alpha = 65^\circ$.

It should be noted that the initial profiles given in Fig. 4.31 as well as figures presented below are again not scaled on both axes, as it would make it difficult to read the figures. Also, the effect of Bond number is immediately recognized with larger droplets, while it does not have a substantial impact on the droplets having relatively smaller size.

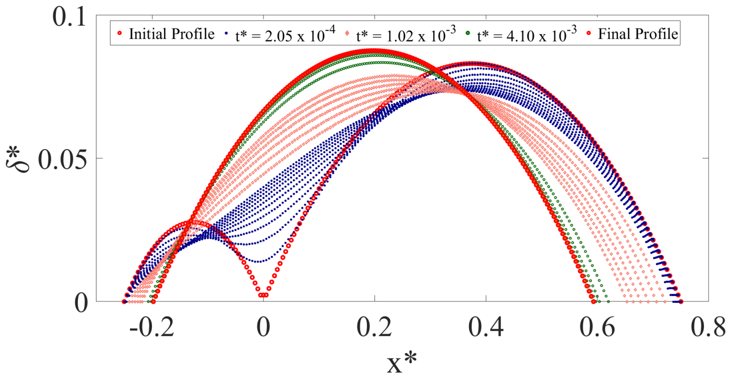

(a)

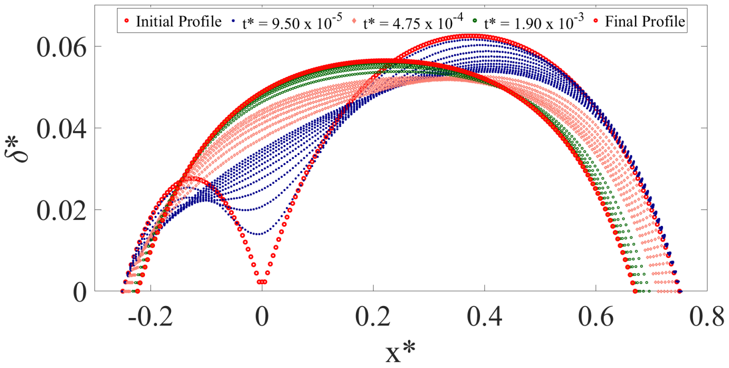

(b)

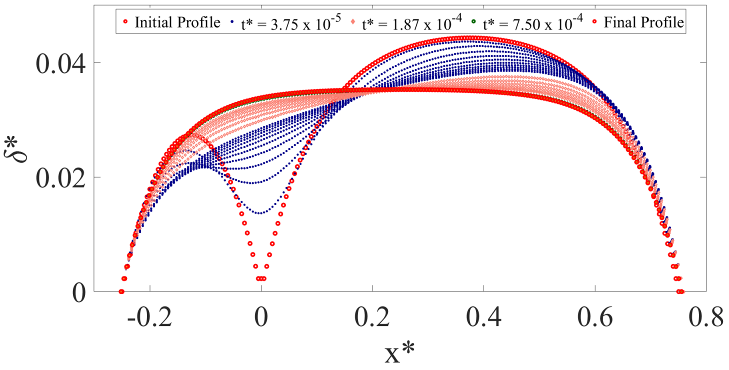

(c)

Figure 4.32: Coalescence results for 25° contact angle case. Simulations with (a) Bo = 0, (b) Bo = 50, (c) Bo = 150

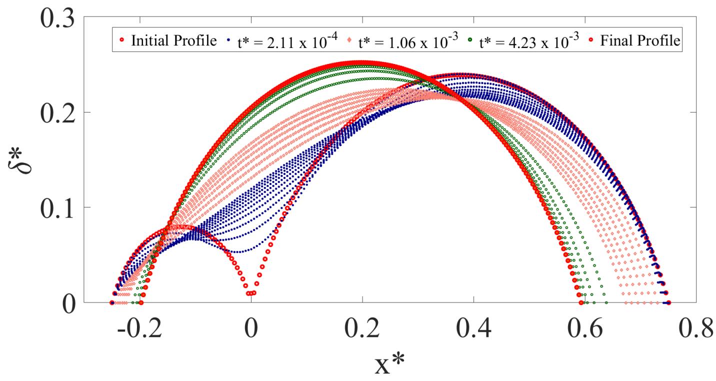

(a)

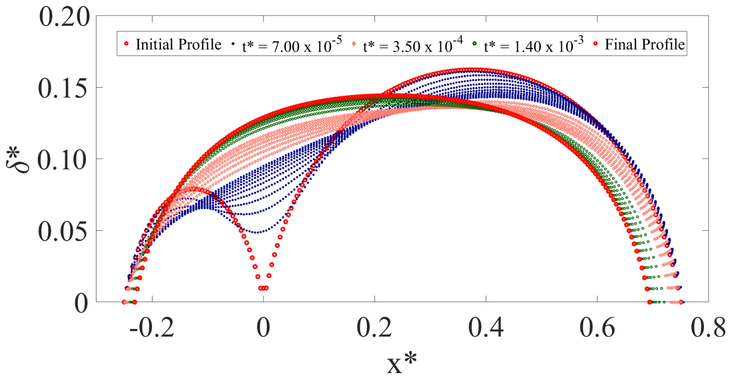

(b)

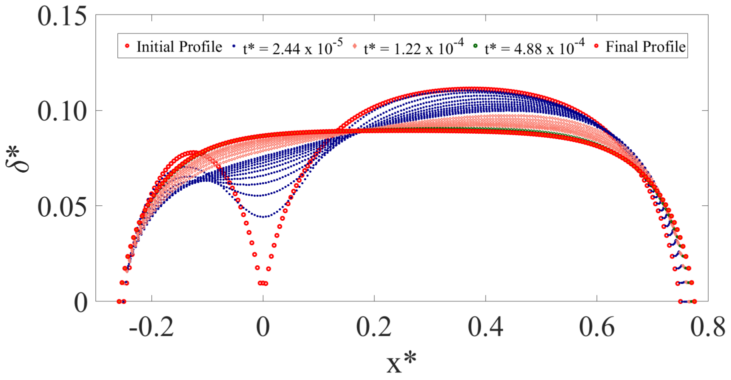

(c)

Figure 4.33: Coalescence results for $65°$ contact angle case. Simulations with (a) Bo $= 0$, (b) Bo $= 50$, (c) Bo $= 150$

The time evolution of the created settings are presented in Fig. 4.32 and Fig. 4.33. As the coalescence commences, a portion of the larger droplet starts leaning towards the smaller droplet immediately. At the steady state, the middle plane of the final droplet resides between the initial shapes; closer to the initial middle point of the larger droplet. Lastly, the compression of the droplet in the x-axis decreases with increasing Bond number.

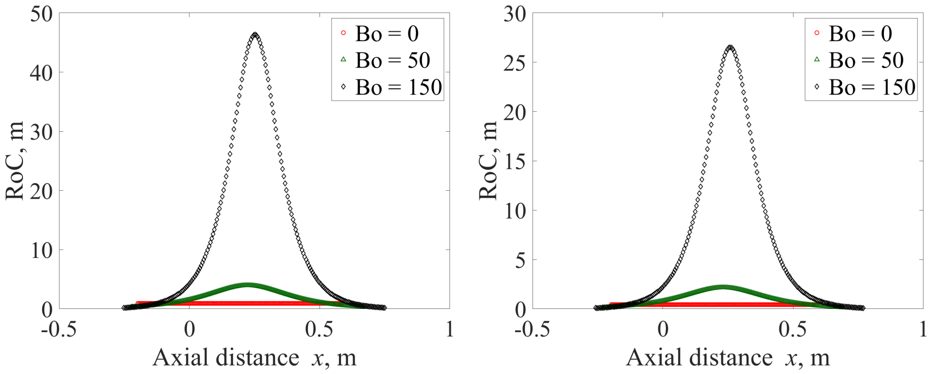

(a)

(b)

Figure 4.34: Non-dimensional analysis on the effect of Bond number to the radius of curvature values at the steady state. Results for (a) contact angle $\alpha = 25°$, (b) contact angle $\alpha = 65°$.

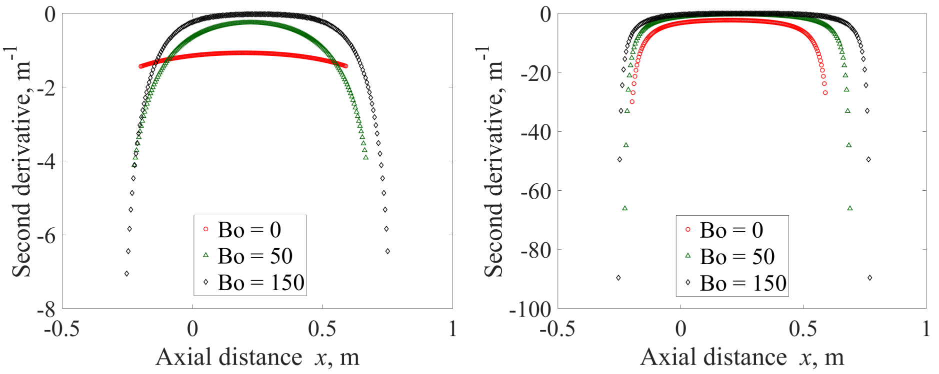

(a)

(b)

Figure 4.35: Non-dimensional analysis on the effect of Bond number to the second derivative values at the steady state. Results for (a) contact angle $\alpha = 25°$, (b) contact angle $\alpha = 65°$.

CHAPTER 5

CONCLUDING REMARKS AND SUGGESTIONS FOR FUTURE WORK

5.1 Conclusion

Droplet or thin film coalescence has been the topic of interest since early 1960's. Various forces such as pressure, viscosity, surface tension and gravity effect the coalescence dynamics of droplets. 2D fully wetting droplets of micron and/or sub-micron scales are first created with Young-Laplace equation and the temporal evolution of coalescing droplets are thoroughly investigated. The governing equation is the unsteady Reynolds equation and it is a 4^{th} order nonlinear PDE. This equation is solved using a time step marching algorithm in conjunction with an implicit formulation of the spatial domain. Nonlinear nature of the equation is overcome by integrating an iterative technique into the formulation of the problem. Coalescence of axially symmetric droplets, two identical droplets and different sized droplets are studied. Aside from the dimensional studies, a non-dimensional analysis is also conducted to find a proper time scale and find the dependencies of the governing equation. It is reached from this analysis that Bond number and the contact angle are the only independent parameters in coalescence dynamics. The approach is validated through the literature and the corresponding verification is completed.

In the dimensional results, coalescence of water droplets on copper and coalescence of R-134a droplets on aluminum is studied. It is observed that R-134a droplets merge much slower compared to the water droplets. Although water has a higher viscosity value than R-134a, it also has higher surface tension value. In return, water touches the substrate with a higher contact angle which enables rapid coalescence. Additionally, the effect of gravity on different sized water droplets are investigated, which is non-negligible for larger droplets. On the other hand, the effect of Bond number and the contact angle on thin film evolution is examined with non-dimensional simulations.

To the best knowledge of the author, there are not any studies in the literature for the coalescence of different sized droplets, which were investigated in detail in the current thesis study. Moreover, coalescence analyses that are conducted in this work included the whole spectrum of contact angles between the close proximity of 0° and 90°, while in the literature, only a certain number of contact angles are often studied. Lastly, previous authors disregarded the denominator term defined in Eq. (3.26) in their studies, however, for larger contact angle values its effect could not be overruled. Therefore, this term was included in our equations as well.

5.2 Suggestions For Future Work

The current study investigates the coalescence of fully wetting 2D droplets. To expand the limits of the study, one can investigate the dynamic movement of fully wetting 3D droplets. Additionally, the merging dynamics of droplets with different wetting characteristics can be studied.

Finally, the dynamic coalescence of a droplet with a meniscus inside the groove of a heat pipe could be studied both in cylindrical and spherical coordinates.

REFERENCES

[1] O. Reynolds, “On the floating of drops on the surface of water depending only on the purity of the surface,” *Proc. Lit. Philos. Soc. Manch.*, 1881.

[2] P. H. Gaskell, P. K. Jimack, M. Sellier, and H. M. Thompson, “Efficient and accurate time adaptive multigrid simulations of droplet spreading,” *International Journal for Numerical Methods in Fluids*, vol. 45, no. 11, pp. 1161–1186, 2004.

[3] S. J. Gokhale, S. DasGupta, J. L. Plawsky, and P. C. Wayner, “Reflectivity-based evaluation of the coalescence of two condensing drops and shape evolution of the coalesced drop,” *Physical Review E - Statistical Physics, Plasmas, Fluids, and Related Interdisciplinary Topics*, vol. 70, no. 5, p. 12, 2004.

[4] J. Lopes and A. Dukler, “Droplet sizes, dynamics and deposition in vertical annular flow,” tech. rep., Historical Energy Database (United States), October 1985.

[5] E. Villermaux and B. Bossa, “Single-drop fragmentation determines size distribution of raindrops,” *Nature Physics*, vol. 5, pp. 697–702, 2009.

[6] K. L. Mittal, *Advances in Contact Angle, Wettability and Adhesion*. Hoboken, NJ, USA: John Wiley & Sons, Inc., September 2015.

[7] A. Marmur, “Wetting on Hydrophobic Rough Surfaces: To Be Heterogeneous or Not To Be?,” *Langmuir*, vol. 19, pp. 8343–8348, September 2003.

[8] S. Khandekar and K. Muralidhar, *Drop Dynamics and Dropwise Condensation on Textured Surfaces*. Springer, 2020.

[9] S. E. Orchard, “On surface levelling in viscous liquids and gels,” *Applied Scientific Research*, vol. 11, no. 4-6, pp. 451–464, 1963.

[10] R. W. Atherton and G. M. Homsy, “On the derivation of evolution equations for interfacial waves,” *Chemical Engineering Communications*, vol. 2, no. 2, pp. 57–77, 1976.

[11] R. W. Hopper, “Plane stokes flow driven by capillarity on a free surface,” *Journal of Fluid Mechanics*, vol. 213, pp. 349–375, 1990.

[12] R. W. Hopper, “Stokes flow of a cylinder and half-space driven by capillarity,” *Journal of Fluid Mechanics*, vol. 243, pp. 171–181, 1992.

[13] R. W. Hopper, “Coalescence of Two Viscous Cylinders by Capillarity: Part I, Theory,” *Journal of the American Ceramic Society*, vol. 76, no. 12, pp. 2947–2952, 1993.

[14] R. W. Hopper, “Coalescence of Two Viscous Cylinders by Capillarity: Part II, Shape Evolution,” *Journal of the American Ceramic Society*, vol. 76, no. 12, pp. 2947–2952, 1993.

[15] J. Frenkel, “Viscous flow of crystalline bodies under the action of surface tension,” *The Journal of Physics, USSR*, 1945.

[16] J. Eggers, J. R. Lister, and H. A. Stone, “Coalescence of liquid drops,” *Journal of Fluid Mechanics*, vol. 401, no. September, pp. 293–310, 1999.

[17] C. Andrieu, D. A. Beysens, V. S. Nikolayev, and Y. Pomeau, “Coalescence of sessile drops,” *Journal of Fluid Mechanics*, vol. 453, pp. 427–438, 2002.

[18] D. G. A. L. Aarts, H. N. Lekkerkerker, H. Guo, G. H. Wegdam, and D. Bonn, “Hydrodynamics of droplet coalescence,” *Physical Review Letters*, vol. 95, no. 16, pp. 1–4, 2005.

[19] W. D. Ristenpart, P. M. McCalla, R. V. Roy, and H. A. Stone, “Coalescence of spreading droplets on a wettable substrate,” *Physical Review Letters*, vol. 97, no. 6, pp. 1–4, 2006.

[20] R. Narhe, D. Beysens, and V. S. Nikolayev, “Contact Line Dynamics in Drop Coalescence and Spreading,” *Langmuir*, vol. 20, pp. 1213–1221, February 2004.

[21] M. W. Lee, D. K. Kang, S. S. Yoon, and A. L. Yarin, “Coalescence of two drops on partially wettable substrates,” *Langmuir*, vol. 28, no. 8, pp. 3791–3798, 2012.

[22] M. Sellier and E. Trelluyer, “Modeling the coalescence of sessile droplets,” *Biomicrofluidics*, vol. 3, no. 2, 2009.

[23] M. Sellier, Y. C. Lee, H. M. Thompson, and P. H. Gaskell, “Thin film flow on surfaces containing arbitrary occlusions,” *Computers and Fluids*, vol. 38, no. 1, pp. 171–182, 2009.

[24] R. FERREIRA and F. BERNIS, “Source-type solutions to thin-film equations in higher dimensions,” *European Journal of Applied Mathematics*, vol. 8, pp. 507–524, October 1997.

[25] J. E. Sprittles and Y. D. Shikhmurzaev, “Coalescence of liquid drops: Different models versus experiment,” *Physics of Fluids*, vol. 24, no. 12, 2012.

[26] Q. Zhang, T. Z. Qian, and X. P. Wang, “Phase field simulation of a droplet impacting a solid surface,” *Physics of Fluids*, vol. 28, no. 2, 2016.

[27] C. Klopp and A. Eremin, “On Droplet Coalescence in Quasi-Two-Dimensional Fluids,” *Langmuir*, vol. 36, no. 35, pp. 10615–10621, 2020.

[28] M. Irshad Khodabocus, M. Sellier, and V. Nock, “Scaling laws of droplet coalescence: Theory and numerical simulation,” *Advances in Mathematical Physics*, vol. 2018, 2018.

[29] J. D. Paulsen, J. C. Burton, S. R. Nagel, S. Appathurai, M. T. Harris, and O. A. Basaran, “The inexorable resistance of inertia determines the initial regime of drop coalescence,” *Proceedings of the National Academy of Sciences of the United States of America*, vol. 109, no. 18, pp. 6857–6861, 2012.

[30] U.S. Geological Survey, “Surface Tension and Water.”

[31] O. Akdag, Y. Akkus, and Z. Dursunkaya, “The effect of disjoining pressure on the shape of condensing films in a fin-groove corner,” *International Journal of Thermal Sciences*, vol. 142, pp. 357–365, May 2019.

[32] K. T. Hong, H. Imadojemu, and R. Webb, “Effects of oxidation and surface roughness on contact angle,” *Experimental Thermal and Fluid Science*, vol. 8, pp. 279–285, May 1994.

[33] B. Vadgama and D. K. Harris, “Measurements of the contact angle between R134a and both aluminum and copper surfaces,” *Experimental Thermal and Fluid Science*, vol. 31, no. 8, pp. 979–984, 2007.

[34] J. D. Bernardin, I. Mudawar, C. B. Walsh, and E. I. Franses, “Contact angle temperature dependence for water droplets on practical aluminum surfaces,” *International Journal of Heat and Mass Transfer*, vol. 40, pp. 1017–1033, March 1997.

[35] M. Fukuta, J. Sumiyama, M. Motozawa, A. Hyodo, and T. Yanagisawa, “Evaluation of Wettability of Solid Surface with Oil / Refrigerant Mixture,” *International Compressor Engineering Conference. Paper 2398*, 2016.

[36] S. M. Smith, B. S. Taft, and J. Moulton, “Contact angle measurements for advanced thermal management technologies,” *Frontiers in Heat and Mass Transfer*, vol. 5, no. 1, 2014.

APPENDIX A

FIRST AND LAST TWO ROWS OF COEFFICIENT MATRIX

A.1 Equations of Single Droplet with Symmetry Axis

For $i = 1$:

$$\begin{aligned}
&\left\{1-\lambda_1\left({}_{l}\delta_1^k\right)^3{}_{l}\zeta_2^k-4\lambda_1\left({}_{l}\delta_1^k\right)^3{}_{l}\zeta_1^k-\lambda_1\left({}_{l}\delta_1^k\right)^3{}_{l}\zeta_0^k+2\lambda_2\left({}_{l}\delta_1^k\right)^3\right\}{}_{l+1}\boldsymbol{\delta}_1^k\\
&+\left\{2\lambda_1\left({}_{l}\delta_1^k\right)^3{}_{l}\zeta_2^k+4\lambda_1\left({}_{l}\delta_1^k\right)^3{}_{l}\zeta_1^k+2\lambda_1\left({}_{l}\delta_1^k\right)^3{}_{l}\zeta_0^k-2\lambda_2\left({}_{l}\delta_1^k\right)^3\right\}{}_{l+1}\boldsymbol{\delta}_2^k\\
&\qquad+\left\{-\lambda_1\left({}_{l}\delta_1^k\right)^3{}_{l}\zeta_2^k-\lambda_1\left({}_{l}\delta_1^k\right)^3{}_{l}\zeta_0^k\right\}{}_{l+1}\boldsymbol{\delta}_3^k=\boldsymbol{\delta}_1^{k-1}
\end{aligned}\tag{A.1}$$

For $i = 2$:

$$\begin{aligned}
&\left\{\frac{3\lambda_1}{4}\left({}_{l}\delta_2^k\right)^2\left[{}_{l}\zeta_3^k\left({}_{l}\delta_4^k-2\,{}_{l}\delta_3^k+{}_{l}\delta_2^k\right)-{}_{l}\zeta_1^k\left(2\,{}_{l}\delta_2^k-2\,{}_{l}\delta_1^k\right)\right]+\right.\\
&\left.2\lambda_1\left({}_{l}\delta_2^k\right)^3{}_{l}\zeta_2^k+2\lambda_1\left({}_{l}\delta_2^k\right)^3{}_{l}\zeta_1^k-\lambda_2\left({}_{l}\delta_2^k\right)^3+\frac{3\lambda_2}{4}\left({}_{l}\delta_2^k\right)^2\left({}_{l}\delta_3^k-{}_{l}\delta_1^k\right)+\lambda_3\right\}{}_{l+1}\boldsymbol{\delta}_1^k\\
&+\left\{1-\lambda_1\left({}_{l}\delta_2^k\right)^3{}_{l}\zeta_3^k-4\lambda_1\left({}_{l}\delta_2^k\right)^3{}_{l}\zeta_2^k-2\lambda_1\left({}_{l}\delta_2^k\right)^3{}_{l}\zeta_1^k+2\lambda_2\left({}_{l}\delta_2^k\right)^3\right\}{}_{l+1}\boldsymbol{\delta}_2^k\\
&+\left\{\frac{-3\lambda_1}{4}\left({}_{l}\delta_2^k\right)^2\left[{}_{l}\zeta_3^k\left({}_{l}\delta_4^k-2\,{}_{l}\delta_3^k+{}_{l}\delta_2^k\right)-{}_{l}\zeta_1^k\left(2\,{}_{l}\delta_2^k-2\,{}_{l}\delta_1^k\right)\right]+\right.\\
&\left.2\lambda_1\left({}_{l}\delta_2^k\right)^3{}_{l}\zeta_3^k+2\lambda_1\left({}_{l}\delta_2^k\right)^3{}_{l}\zeta_2^k-\lambda_2\left({}_{l}\delta_2^k\right)^3-\frac{3\lambda_2}{4}\left({}_{l}\delta_2^k\right)^2\left({}_{l}\delta_3^k-{}_{l}\delta_1^k\right)-\lambda_3\right\}{}_{l+1}\boldsymbol{\delta}_3^k\\
&\qquad+\left\{-\lambda_1\left({}_{l}\delta_2^k\right)^3{}_{l}\zeta_3^k\right\}{}_{l+1}\boldsymbol{\delta}_4^k=\boldsymbol{\delta}_2^{k-1}
\end{aligned}\tag{A.2}$$

For $i = N - 3$:

$$
\begin{aligned}
&\Bigg\{ -\lambda_1 ({}_l\delta^k_{N-3})^3\, {}_l\zeta^k_{N-4} \Bigg\}_{l+1}\boldsymbol{\delta}^k_{N-4} \\
&+ \Bigg\{ \frac{3\lambda_1}{4} ({}_l\delta^k_{N-3})^2 \\
&\Bigg[{}_l\zeta^k_{N-2}\left(-\frac{7}{4}\,{}_l\delta^k_{N-2} + {}_l\delta^k_{N-3} - \frac{\Delta x \tan(\pi-\alpha)}{2}\right) \\
&- {}_l\zeta^k_{N-4}\left({}_l\delta^k_{N-3} - 2\,{}_l\delta^k_{N-4} + {}_l\delta^k_{N-5}\right)\Bigg] + \\
&2\lambda_1 \left({}_l\delta^k_{N-3}\right)^3 {}_l\zeta^k_{N-3} + 2\lambda_1({}_l\delta^k_{N-3})^3\, {}_l\zeta^k_{N-4} - \lambda_2({}_l\delta^k_{N-3})^3 + \\
&\frac{3\lambda_2}{4}({}_l\delta^k_{N-3})^2\left({}_l\delta^k_{N-2} - {}_l\delta^k_{N-4}\right) + \lambda_3 \Bigg\}_{l+1}\boldsymbol{\delta}^k_{N-3} \\
&+ \Bigg\{ 1 - \lambda_1({}_l\delta^k_{N-3})^3\, {}_l\zeta^k_{N-2} - 4\lambda_1({}_l\delta^k_{N-3})^3\, {}_l\zeta^k_{N-3} \\
&-\lambda_1({}_l\delta^k_{N-3})^3\, {}_l\zeta^k_{N-4} + 2\lambda_2({}_l\delta^k_{N-3})^3 \Bigg\}_{l+1}\boldsymbol{\delta}^k_{N-3} \\
&+ \Bigg\{ -\frac{3\lambda_1}{4}({}_l\delta^k_{N-3})^2 \\
&\Bigg[{}_l\zeta^k_{N-2}\left(-\frac{7}{4}\,{}_l\delta^k_{N-2} + {}_l\delta^k_{N-3} - \frac{\Delta x \tan(\pi-\alpha)}{2}\right) \\
&- {}_l\zeta^k_{N-4}\left({}_l\delta^k_{N-3} - 2\,{}_l\delta^k_{N-4} + {}_l\delta^k_{N-5}\right)\Bigg] + \\
&2\lambda_1 \left({}_l\delta^k_{N-3}\right)^3 {}_l\zeta^k_{N-2} + 2\lambda_1({}_l\delta^k_{N-3})^3\, {}_l\zeta^k_{N-3} - \lambda_2({}_l\delta^k_{N-3})^3 + \\
&-\frac{3\lambda_2}{4}({}_l\delta^k_{N-3})^2\left({}_l\delta^k_{N-2} - {}_l\delta^k_{N-4}\right) - \lambda_3 \Bigg\}_{l+1}\boldsymbol{\delta}^k_{N-2} \\
&= \boldsymbol{\delta}^{k-1}_{N-3} + \Bigg\{ -\lambda_1({}_l\delta^k_{N-3})^3\, {}_l\zeta^k_{N-2} \Bigg\}\left[\frac{\Delta x \tan(\pi-\alpha)}{2}\right]
\end{aligned}
\tag{A.3}
$$

For $i = N-2$:

$$
\begin{aligned}
&\Big\{ -\lambda_1 ({}_l\delta^k_{N-2})^3 \, {}_l\zeta^k_{N-3} \Big\} {}_{l+1}\boldsymbol{\delta}^k_{N-4} \\
&+ \Bigg\{ \frac{3\lambda_1}{4} ({}_l\delta^k_{N-2})^2 \Bigg[{}_l\zeta^k_{N-1} \left(\frac{{}_l\delta^k_{N-2}}{2} + \Delta x \tan(\pi-\alpha) \right) \\
&\qquad - {}_l\zeta^k_{N-3} \left({}_l\delta^k_{N-2} - 2\,{}_l\delta^k_{N-3} + {}_l\delta^k_{N-4}\right) \Bigg] + \\
&2\lambda_1 \left({}_l\delta^k_{N-2}\right)^3 {}_l\zeta^k_{N-2} + 2\lambda_1 ({}_l\delta^k_{N-2})^3 \, {}_l\zeta^k_{N-3} - \lambda_2 ({}_l\delta^k_{N-2})^3 + \\
&\frac{3\lambda_2}{4} ({}_l\delta^k_{N-2})^2 \left(\frac{{}_l\delta^k_{N-2}}{4} - \frac{\Delta x \tan(\pi-\alpha)}{2} - {}_l\delta^k_{N-3} \right) + \lambda_3 \Bigg\} {}_{l+1}\boldsymbol{\delta}^k_{N-3} \\
&+ \Bigg\{ 1 - \frac{3\lambda_1}{16} ({}_l\delta^k_{N-2})^2 \Bigg[{}_l\zeta^k_{N-1} \left(\frac{{}_l\delta^k_{N-2}}{2} + \Delta x \tan(\pi-\alpha) \right) \\
&- {}_l\zeta^k_{N-3} \left({}_l\delta^k_{N-2} - 2\,{}_l\delta^k_{N-3} + {}_l\delta^k_{N-4}\right) \Bigg] - \frac{\lambda_1}{2} \left({}_l\delta^k_{N-2}\right)^3 {}_l\zeta^k_{N-1} \\
&-\frac{7\lambda_1}{2} \left({}_l\delta^k_{N-2}\right)^3 {}_l\zeta^k_{N-2} - \lambda_1 \left({}_l\delta^k_{N-2}\right)^3 {}_l\zeta^k_{N-3} + \frac{7\lambda_2}{4} \left({}_l\delta^k_{N-2}\right)^3 - \\
&\frac{3\lambda_2}{16} \left({}_l\delta^k_{N-2}\right)^2 \left(\frac{{}_l\delta^k_{N-2}}{4} - \frac{\Delta x \tan(\pi-\alpha)}{2} - {}_l\delta^k_{N-3} \right) - \frac{\lambda_3}{4} \Bigg\} {}_{l+1}\boldsymbol{\delta}^k_{N-2} \\
&= \boldsymbol{\delta}^{k-1}_{N-3} + \Bigg\{ -\frac{3\lambda_1}{4} ({}_l\delta^k_{N-2})^2 \Bigg[{}_l\zeta^k_{N-1} \left(\frac{{}_l\delta^k_{N-2}}{2} + \Delta x \tan(\pi-\alpha) \right) \\
&\qquad - {}_l\zeta^k_{N-3} \left({}_l\delta^k_{N-2} - 2\,{}_l\delta^k_{N-3} + {}_l\delta^k_{N-4}\right) \Bigg] + \\
&2\lambda_1 \left({}_l\delta^k_{N-2}\right)^3 {}_l\zeta^k_{N-1} + 2\lambda_1 ({}_l\delta^k_{N-2})^3 \, {}_l\zeta^k_{N-2} - \lambda_2 ({}_l\delta^k_{N-2})^3 + \\
&\frac{3\lambda_2}{4} ({}_l\delta^k_{N-2})^2 \left(\frac{{}_l\delta^k_{N-2}}{4} - \frac{\Delta x \tan(\pi-\alpha)}{2} - {}_l\delta^k_{N-3} \right) - \lambda_3 \Bigg\} \\
&\qquad \left[\frac{\Delta x \tan(\pi-\alpha)}{2} \right]
\end{aligned}
\tag{A.4}
$$

A.2 Equations of Two Identical Droplets

For $i = 3$:

$$
\begin{aligned}
&\Bigg\{1 + \frac{3\lambda_1}{16}({}_l\delta_3^k)^2 \\
&\left[{}_l\zeta_4^k \left({}_l\delta_5^k - 2\,{}_l\delta_4^k + 2\,{}_l\delta_3^k\right) - {}_l\zeta_2^k \left(\frac{{}_l\delta_3^k}{2} - \Delta x \tan\alpha\right)\right] \\
&-\lambda_1 \left({}_l\delta_3^k\right)^3 {}_l\zeta_4^k - \frac{7\lambda_1}{2} \left({}_l\delta_3^k\right)^3 {}_l\zeta_3^k - \frac{\lambda_1}{2} \left({}_l\delta_3^k\right)^3 {}_l\zeta_2^k \\
&+\frac{7\lambda_2}{4} \left({}_l\delta_3^k\right)^3 + \frac{3\lambda_2}{16} \left({}_l\delta_3^k\right)^2 \left({}_l\delta_4^k - \frac{{}_l\delta_3^k}{4} - \frac{\Delta x \tan\alpha}{2}\right) + \frac{\lambda_3}{4} \Bigg\}_{l+1}\boldsymbol{\delta}_3^k \\
&+\Bigg\{\frac{-3\lambda_1}{4}({}_l\delta_3^k)^2 \\
&\left[{}_l\zeta_4^k \left({}_l\delta_5^k - 2\,{}_l\delta_4^k + {}_l\delta_3^k\right) - {}_l\zeta_2^k \left(\frac{{}_l\delta_3^k}{2} - \Delta x \tan\alpha\right)\right] \\
&+2\lambda_1 \left({}_l\delta_3^k\right)^3 {}_l\zeta_4^k + 2\lambda_1({}_l\delta_3^k)^3 \, {}_l\zeta_3^k - \lambda_2({}_l\delta_3^k)^3 \\
&-\frac{3\lambda_2}{4}({}_l\delta_3^k)^2 \left({}_l\delta_4^k - \frac{{}_l\delta_3^k}{4} - \frac{\Delta x \tan\alpha}{2}\right) - \lambda_3 \Bigg\}_{l+1}\boldsymbol{\delta}_4^k \\
&+\Bigg\{ - \lambda_1({}_l\delta_3^k)^3 \, {}_l\zeta_4^k \Bigg\}_{l+1}\boldsymbol{\delta}_5^k \\
&= \boldsymbol{\delta}_3^{k-1} - \Bigg\{\frac{-3\lambda_1}{4}({}_l\delta_3^k)^2 \Bigg[{}_l\zeta_4^k \left({}_l\delta_5^k - 2\,{}_l\delta_4^k + {}_l\delta_3^k\right) \\
&- {}_l\zeta_2^k \left(\frac{{}_l\delta_3^k}{2} - \Delta x \tan\alpha\right)\Bigg] \\
&+2\lambda_1 \left({}_l\delta_3^k\right)^3 {}_l\zeta_3^k + 2\lambda_1({}_l\delta_3^k)^3 \, {}_l\zeta_2^k - \lambda_2({}_l\delta_3^k)^3 \\
&+\frac{3\lambda_2}{4}({}_l\delta_3^k)^2 \left({}_l\delta_4^k - \frac{{}_l\delta_3^k}{4} - \frac{\Delta x \tan\alpha}{2}\right) + \lambda_3 \Bigg\} \left[\frac{\Delta x \tan\alpha}{2}\right]
\end{aligned}
\tag{A.5}
$$

For $i = 4$:

$$
\begin{aligned}
&\Bigg\{ \frac{3\lambda_1}{4} ({}_l\delta_4^k)^2 \\
&\left[{}_l\zeta_5^k \left({}_l\delta_6^k - 2\,{}_l\delta_5^k + 2\,{}_l\delta_4^k \right) - {}_l\zeta_3^k \left({}_l\delta_4^k - \frac{7}{4}\,{}_l\delta_3^k + \frac{\Delta x \tan\alpha}{2} \right) \right] \\
&+2\lambda_1 \left({}_l\delta_4^k\right)^3 {}_l\zeta_4^k + \frac{7\lambda_1}{4} \left({}_l\delta_4^k\right)^3 {}_l\zeta_3^k \\
&-\lambda_2 \left({}_l\delta_4^k\right)^3 + \frac{3\lambda_2}{4} \left({}_l\delta_4^k\right)^2 \left({}_l\delta_5^k - {}_l\delta_3^k\right) + \lambda_3 \Bigg\}_{l+1}\boldsymbol{\delta}_3^k \\
&+ \Bigg\{ 1 - \lambda_1 \left({}_l\delta_4^k\right)^3 {}_l\zeta_5^k - 4\lambda_1 \left({}_l\delta_4^k\right)^3 {}_l\zeta_4^k - \lambda_1 \left({}_l\delta_4^k\right)^3 {}_l\zeta_3^k + 2\lambda_2 \left({}_l\delta_4^k\right)^3 \Bigg\}_{l+1}\boldsymbol{\delta}_4^k \\
&\Bigg\{ - \frac{3\lambda_1}{4} ({}_l\delta_4^k)^2 \\
&\left[{}_l\zeta_5^k \left({}_l\delta_6^k - 2\,{}_l\delta_5^k + 2\,{}_l\delta_4^k \right) - {}_l\zeta_3^k \left({}_l\delta_4^k - \frac{7}{4}\,{}_l\delta_3^k + \frac{\Delta x \tan\alpha}{2} \right) \right] \\
&+2\lambda_1 \left({}_l\delta_4^k\right)^3 {}_l\zeta_5^k + 2\lambda_1 \left({}_l\delta_4^k\right)^3 {}_l\zeta_4^k \\
&-\lambda_2 \left({}_l\delta_4^k\right)^3 - \frac{3\lambda_2}{4} \left({}_l\delta_4^k\right)^2 \left({}_l\delta_5^k - {}_l\delta_3^k\right) - \lambda_3 \Bigg\}_{l+1}\boldsymbol{\delta}_5^k \\
&\Bigg\{ - \lambda_1 ({}_l\delta_4^k)^3\, {}_l\zeta_5^k \Bigg\}_{l+1}\boldsymbol{\delta}_6^k \\
&= \boldsymbol{\delta}_4^{k-1} - \Bigg\{ - \lambda_1 ({}_l\delta_4^k)^3\, {}_l\zeta_3^k \Bigg\} \left[\frac{\Delta x \tan\alpha}{2} \right]
\end{aligned}
\tag{A.6}
$$

For $i = N-3$:

$$
\begin{aligned}
&\Big\{ -\lambda_1 ({}_l\delta^k_{N-3})^3\, {}_l\zeta^k_{N-4} \Big\}_{l+1} \boldsymbol{\delta}^k_{N-4} \\
&+ \Big\{ \frac{3\lambda_1}{4} ({}_l\delta^k_{N-3})^2 \\
&\Big[{}_l\zeta^k_{N-2} \Big(-\frac{7}{4}\, {}_l\delta^k_{N-2} + {}_l\delta^k_{N-3} - \frac{\Delta x \tan(\pi-\alpha)}{2} \Big) \\
&- {}_l\zeta^k_{N-4} \big({}_l\delta^k_{N-3} - 2\, {}_l\delta^k_{N-4} + {}_l\delta^k_{N-5} \big) \Big] + \\
&2\lambda_1 \big({}_l\delta^k_{N-3}\big)^3\, {}_l\zeta^k_{N-3} + 2\lambda_1 ({}_l\delta^k_{N-3})^3\, {}_l\zeta^k_{N-4} - \lambda_2 ({}_l\delta^k_{N-3})^3 + \\
&\frac{3\lambda_2}{4} ({}_l\delta^k_{N-3})^2 \big({}_l\delta^k_{N-2} - {}_l\delta^k_{N-4} \big) + \lambda_3 \Big\}_{l+1} \boldsymbol{\delta}^k_{N-3} \\
&+ \Big\{ 1 - \lambda_1 ({}_l\delta^k_{N-3})^3\, {}_l\zeta^k_{N-2} - 4\lambda_1 ({}_l\delta^k_{N-3})^3\, {}_l\zeta^k_{N-3} \\
&-\lambda_1 ({}_l\delta^k_{N-3})^3\, {}_l\zeta^k_{N-4} + 2\lambda_2 ({}_l\delta^k_{N-3})^3 \Big\}_{l+1} \boldsymbol{\delta}^k_{N-3} \\
&+ \Big\{ -\frac{3\lambda_1}{4} ({}_l\delta^k_{N-3})^2 \\
&\Big[{}_l\zeta^k_{N-2} \Big(-\frac{7}{4}\, {}_l\delta^k_{N-2} + {}_l\delta^k_{N-3} - \frac{\Delta x \tan(\pi-\alpha)}{2} \Big) \\
&- {}_l\zeta^k_{N-4} \big({}_l\delta^k_{N-3} - 2\, {}_l\delta^k_{N-4} + {}_l\delta^k_{N-5} \big) \Big] + \\
&2\lambda_1 \big({}_l\delta^k_{N-3}\big)^3\, {}_l\zeta^k_{N-2} + 2\lambda_1 ({}_l\delta^k_{N-3})^3\, {}_l\zeta^k_{N-3} - \lambda_2 ({}_l\delta^k_{N-3})^3 + \\
&-\frac{3\lambda_2}{4} ({}_l\delta^k_{N-3})^2 \big({}_l\delta^k_{N-2} - {}_l\delta^k_{N-4} \big) - \lambda_3 \Big\}_{l+1} \boldsymbol{\delta}^k_{N-2} \\
&= \boldsymbol{\delta}^{k-1}_{N-3} + \Big\{ -\lambda_1 ({}_l\delta^k_{N-3})^3\, {}_l\zeta^k_{N-2} \Big\} \Big[\frac{\Delta x \tan(\pi-\alpha)}{2} \Big]
\end{aligned}
\tag{A.7}
$$

For $i = N-2$:

$$
\begin{aligned}
\Big\{ -\lambda_1({}_l\delta^k_{N-2})^3\,{}_l\zeta^k_{N-3}\Big\}{}_{l+1}\boldsymbol{\delta}^k_{N-4} \\
+\Big\{\frac{3\lambda_1}{4}({}_l\delta^k_{N-2})^2\Big[{}_l\zeta^k_{N-1}\Big(\frac{{}_l\delta^k_{N-2}}{2}+\Delta x\tan(\pi-\alpha)\Big) \\
-{}_l\zeta^k_{N-3}\big({}_l\delta^k_{N-2}-2\,{}_l\delta^k_{N-3}+{}_l\delta^k_{N-4}\big)\Big]+ \\
2\lambda_1\big({}_l\delta^k_{N-2}\big)^3\,{}_l\zeta^k_{N-2}+2\lambda_1({}_l\delta^k_{N-2})^3\,{}_l\zeta^k_{N-3}-\lambda_2({}_l\delta^k_{N-2})^3+ \\
\frac{3\lambda_2}{4}({}_l\delta^k_{N-2})^2\Big(\frac{{}_l\delta^k_{N-2}}{4}-\frac{\Delta x\tan(\pi-\alpha)}{2}-{}_l\delta^k_{N-3}\Big)+\lambda_3\Big\}{}_{l+1}\boldsymbol{\delta}^k_{N-3} \\
+\Big\{1-\frac{3\lambda_1}{16}({}_l\delta^k_{N-2})^2\Big[{}_l\zeta^k_{N-1}\Big(\frac{{}_l\delta^k_{N-2}}{2}+\Delta x\tan(\pi-\alpha)\Big) \\
-{}_l\zeta^k_{N-3}\big({}_l\delta^k_{N-2}-2\,{}_l\delta^k_{N-3}+{}_l\delta^k_{N-4}\big)\Big]-\frac{\lambda_1}{2}\big({}_l\delta^k_{N-2}\big)^3\,{}_l\zeta^k_{N-1} \\
-\frac{7\lambda_1}{2}\big({}_l\delta^k_{N-2}\big)^3\,{}_l\zeta^k_{N-2}-\lambda_1\big({}_l\delta^k_{N-2}\big)^3\,{}_l\zeta^k_{N-3}+\frac{7\lambda_2}{4}\big({}_l\delta^k_{N-2}\big)^3- \\
\frac{3\lambda_2}{16}\big({}_l\delta^k_{N-2}\big)^2\Big(\frac{{}_l\delta^k_{N-2}}{4}-\frac{\Delta x\tan(\pi-\alpha)}{2}-{}_l\delta^k_{N-3}\Big)-\frac{\lambda_3}{4}\Big\}{}_{l+1}\boldsymbol{\delta}^k_{N-2} \\
=\boldsymbol{\delta}^{k-1}_{N-3}+\Big\{-\frac{3\lambda_1}{4}({}_l\delta^k_{N-2})^2\Big[{}_l\zeta^k_{N-1}\Big(\frac{{}_l\delta^k_{N-2}}{2}+\Delta x\tan(\pi-\alpha)\Big) \\
-{}_l\zeta^k_{N-3}\big({}_l\delta^k_{N-2}-2\,{}_l\delta^k_{N-3}+{}_l\delta^k_{N-4}\big)\Big]+ \\
2\lambda_1\big({}_l\delta^k_{N-2}\big)^3\,{}_l\zeta^k_{N-1}+2\lambda_1({}_l\delta^k_{N-2})^3\,{}_l\zeta^k_{N-2}-\lambda_2({}_l\delta^k_{N-2})^3+ \\
\frac{3\lambda_2}{4}({}_l\delta^k_{N-2})^2\Big(\frac{{}_l\delta^k_{N-2}}{4}-\frac{\Delta x\tan(\pi-\alpha)}{2}-{}_l\delta^k_{N-3}\Big)-\lambda_3\Big\} \\
\Big[\frac{\Delta x\tan(\pi-\alpha)}{2}\Big]
\end{aligned}
\tag{A.8}
$$

APPENDIX B

FLOWCHARTS

B.1 Flowchart of Droplet Modelling

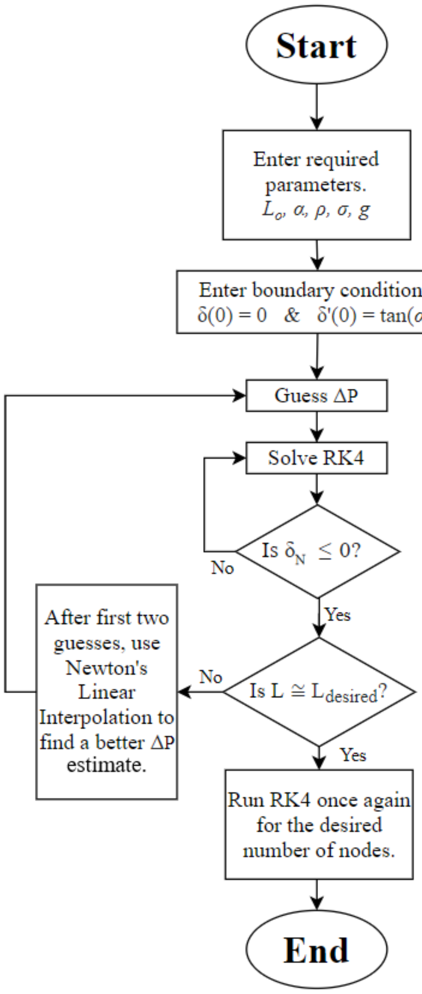

Figure B.1: Flowchart of numerical method of the droplet modelling

B.2 Flowchart of Coalescence of Droplets

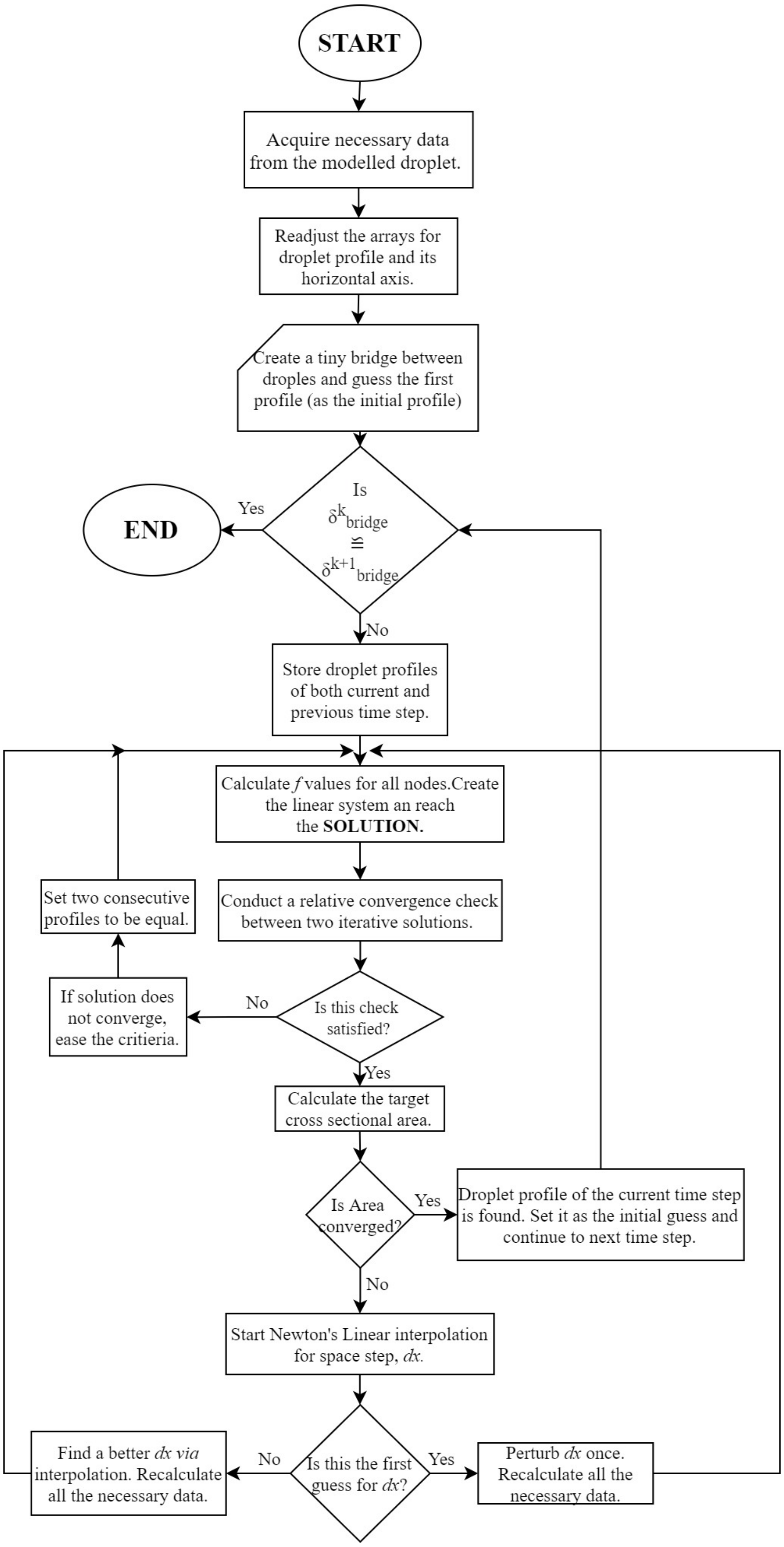

Figure B.2: Flowchart of numerical method of the droplet coalescence